

High-Resolution Observations of Emerging Flux Regions

Dissertation
zur Erlangung des akademischen Grades
doctor rerum naturalium
(Dr. rer. nat.)
in der Wissenschaftsdisziplin Astronomie und Astrophysik

eingereicht an der
Mathematisch-Naturwissenschaftlichen Fakultät
der Universität Potsdam

Sergio Javier González Manrique

January 27, 2017



Leibniz-Institut für Astrophysik Potsdam
An der Sternwarte 16
14482 Potsdam



Universität Potsdam
Institut für Physik und Astronomie
Karl-Liebknecht-Straße 24/25
14476 Potsdam-Golm

Table of Contents

Abstract	1
1 Introduction	5
1.1 Emerging magnetic flux on the solar surface	5
1.1.1 Quiet-Sun magnetic fields	5
1.1.2 Flux emergence	8
1.1.3 Pores and micro-pores	9
1.1.4 Chromospheric response	11
1.1.5 Theoretical models of flux emergence	12
1.2 Solar telescopes	14
1.2.1 Vacuum Tower Telescope	14
1.2.2 GREGOR telescope	15
1.3 Instruments	17
1.3.1 The GREGOR Fabry-Pérot Interferometer	17
1.3.2 The GREGOR Infrared Spectrograph	18
2 High-resolution imaging spectroscopy of two micro-pores and an arch filament system in a small emerging flux region	21
2.1 Observations	23
2.2 Data analysis	24
2.2.1 Local correlation tracking	24
2.2.2 Cloud model inversions	24
2.2.3 Cluster analysis	27
2.3 Results	27
2.3.1 Temporal evolution of micro-pores	28
2.3.2 Horizontal flow field around micro-pores	30
2.3.3 Chromospheric fine structure and Doppler velocity	31
2.3.4 Cloud model inversions	32
2.3.5 Properties of the arch filament system	33
2.4 Discussion	37
2.5 Conclusions	41
3 Fitting peculiar spectral profiles in He I 10830 Å absorption features	43
3.1 Observations	44
3.2 Data reduction	45
3.3 Method	47
3.4 Results	48
3.5 Conclusions and outlook	49
4 Tracking photospheric and chromospheric high-velocity features in an arch filament system	51
4.1 Observations	51
4.2 Data reduction	55
4.3 Data analysis	56
4.3.1 Temporal evolution of emerging magnetic flux	56
4.3.2 Center-to-center distance of pores	57

4.3.3	Line-of-sight velocities of NIR lines	57
4.3.4	Bisectors and spectral inversions of the Si I line	58
4.3.5	Inversion of the photospheric Fe I line	58
4.3.6	Inversion of the chromospheric Ca I line	59
4.3.7	Horizontal proper motions	60
4.4	Results	60
4.4.1	Inflows associated with the central pore	61
4.4.2	Temporal evolution	62
4.4.3	Height dependence	65
4.5	Discussions and conclusions	70
5	Conclusions and outlook	73
	Bibliography	77
	Acknowledgments	95
	Appendix A – Abstracts	97
	Appendix B – List of Acronyms	103

Abstract

High-resolution observations of the Sun are of utmost importance to improve our understanding of the complex and intricate interaction between plasma and magnetic fields. This doctoral thesis focuses on photospheric and chromospheric observations of emerging flux regions and arch filament systems, which were obtained with the Vacuum Tower Telescope and the GREGOR solar telescope at Observatorio del Teide, Tenerife, Spain. The research project is based on these two data sets.

Emerging flux regions mark the first stage in the accumulation of magnetic flux eventually leading to pores, sunspots, and (complex) active regions. These flux regions are highly dynamic, show a variety of fine structure, and live in many cases only for a short time (less than a day) before dissolving quickly into the ubiquitous quiet-Sun magnetic field.

The purpose of this investigation is to characterize the temporal evolution of a minute emerging flux region, the associated photospheric and chromospheric flow fields, and the properties of the accompanying arch filament system. We explore flux emergence and decay processes and investigate if they scale with structure size and magnetic flux contents.

This study is based on imaging spectroscopy with the Göttingen Fabry-Pérot Interferometer at the Vacuum Tower Telescope, Observatorio del Teide, Tenerife, Spain on 2008 August 7. Photospheric horizontal proper motions were measured with Local Correlation Tracking using broad-band images restored with Multi-Object Multi-Frame Blind Deconvolution. Cloud model inversions of line scans in the strong chromospheric absorption $H\alpha$ $\lambda 656.28$ nm line yield cloud model parameters (Doppler velocity, Doppler width, optical thickness, and source function), which describe the cool plasma contained in the arch filament system.

The high-resolution observations cover the decay and convergence of two micro-pores with diameters of less than one second of arc and provide decay rates for intensity and area. The photospheric horizontal flow speed is suppressed near the two micro-pores indicating that the magnetic field is already sufficiently strong to affect the convective energy transport. The micro-pores are accompanied by a small arch filament system as seen in $H\alpha$, where small-scale loops connect two regions with $H\alpha$ line-core brightenings containing an emerging flux region with opposite polarities. The Doppler width, optical thickness, and source function reach the largest values near the $H\alpha$ line-core brightenings. The chromospheric velocity of the cloud material is predominantly directed downwards near the footpoints of the loops with velocities of up to 12 km s^{-1} , whereas loop tops show upward motions of about 3 km s^{-1} . Some of the loops exhibit signs of twisting motions along the loop axis.

Micro-pores are the smallest magnetic field concentrations leaving a photometric signature in the photosphere. In the observed case, they are accompanied by a miniature arch filament system indicative of newly emerging flux in the form of Ω -loops. Flux emergence and decay take place on a time-scale of about two days, whereas the photometric decay of the micro-pores is much more rapid (a few hours), which is consistent with the incipient submergence of Ω -loops. Considering lifetime and evolution time-scales, impact on the surrounding photospheric proper motions, and flow speed of the chromospheric plasma at the loop tops and footpoints, the results are representative for the smallest emerging flux regions still recognizable as such.

The new generation of solar instruments provides better spectral, spatial, and temporal resolution for a better understanding of the physical processes that take place on the Sun. Multiple-component profiles are more commonly observed with these instruments. Particularly, the He I 10830 Å triplet presents such peculiar spectral profiles, which give information on the velocity and magnetic fine structure of the upper chromosphere. The purpose of this investigation is to describe a technique to efficiently fit the two blended components of the He I 10830 Å triplet, which are commonly observed when two atmospheric components are located within the same resolution element. The observations used in this study were taken on 2015 April 17 with the very fast spectroscopic mode of the GREGOR Infrared Spectrograph attached to the 1.5-meter GREGOR solar telescope, located at the Observatorio del Teide, Tenerife, Spain. We apply

a double-Lorentzian fitting technique using Levenberg-Marquardt least-squares minimization. This technique is very simple and much faster than inversion codes. Line-of-sight Doppler velocities can be inferred for a whole map of pixels within just a few minutes. Our results show sub- and supersonic downflow velocities of up to 40 km s^{-1} for the fast component in the vicinity of footpoints of filamentary structures. The slow component presents velocities close to rest.

The initial analysis of the He I 10830 Å triplet focused on just a single spectral scan, i.e., a snapshot. However, the ‘very fast spectroscopic mode’ of the GREGOR Infrared Spectrograph facilitates time-resolved observations, which have a duration of about one hour and a cadence of just one minute. These observations were complemented by observations with the GREGOR Fabry-Pérot Interferometer and the CRisp Imaging Spectropolarimeter at the Swedish Solar Telescope at Observatorio del Roque de los Muchachos, La Palma, Spain. Additional context data was provided by the Solar Dynamics Observatory using the Helioseismic and Magnetic Imager and the Atmospheric Imaging Assembly.

New magnetic flux is still emerging, which leads to an arch filament system connecting both pores and other small-scale magnetic elements with multiple dark filament strands. The observed He I supersonic downflows at the footpoints near the pores and upflows up to 5 km s^{-1} at the loop tops of arch filaments are in very good agreement with previous observations. Tracking these velocities along the arch filaments and following their temporal evolution give us a lifetime of about 25–30 min for rising Ω -loops, which is at the upper end of values given in literature. The lowest values of chromospheric velocities (2.7 km s^{-1}) are inferred with the Ca II 8542 Å line reaching to approaching 0 km s^{-1} at $\log \tau \sim 0$. Photospheric downflows with lower velocities were observed cospatial with the supersonic chromospheric velocities at the footpoints near the pores. These observations are consistent with emerging Ω -loops, where cool material rises to chromospheric heights and beyond at the loop tops and then drains towards the footpoints of the loops. In this study we confirmed the link of these supersonic chromospheric downflows in the footpoints of the arch filament system with downflows observed in the photosphere. This allowed us to calculate an approximate height distance between the footpoints in the chromosphere and the photosphere. This distance can be as large as 1100 km. However, the presence of shocks in the downflowing material potentially affects this value. Regarding the horizontal proper motions in the photosphere, we found inflows around the newly formed pores. Combining these results with the photospheric and chromospheric line-of-sight velocities, we conclude that the plasma likely experiences convective collapse when moving downwards along the arch filaments and reaching the photosphere at the pore.

Time-resolved spectroscopy revealed temporal evolution of He I spectra in proximity to a pore with the strong downflows and the presence of dual-component He I spectral profiles. Using 69 locally averaged spectra in every spectral scan allowed us identify significant changes in the shape of the red component. Initially the slow and fast red component have well-separated minima but with time they vanish and the fast component only contributes to line asymmetry, leaving a single-component profile with a deeper line core in the end. At times, when the fast component becomes dominant, line-core intensities reach $I_{\text{core}}/I_c < 0.8$.

The height dependence of line-of-sight velocities was inferred with two independent methods, which were based on bisectors of spectral lines as a function of line depth and on inversions with the SIR code computing velocities as a function of optical depth. The result was an almost linear dependence of derived velocities so that line depth and optical depth could be matched. Deviation from this linear relationship were only found for the line core, which is formed under non-LTE conditions, and close to the continuum, where broad line wings and noise hamper the computation of bisectors.

Observations with multiple instruments and spectral lines like in this doctoral thesis improve our understanding of plasma dynamics in the presence of magnetic fields. Generally, newly emerging magnetic flux reaches the photosphere, the chromosphere, and the upper atmospheric layers like the transition region and corona, as many observations and simulations suggested. Thus, this doctoral thesis is a part of the puzzle revealing the physics governing emerging flux regions and arch filament systems.

The doctoral thesis is based on two refereed articles (one published, one accepted for publication), a submitted article for a conference proceedings, and material for a forthcoming refereed article. Formatting of these articles (including the figures) were adapted to give this doctoral thesis uniform layout. Some text of the articles was used for the abstract and conclusions of this thesis deviating from the structure of the original articles. In the following I outline my contributions and those of the co-authors.

S.J. González Manrique, N. Bello González, C. Denker: 2017, High-Resolution Imaging Spectroscopy of Two Micro-Pores and an Arch Filament System in a Small Emerging Flux Region. *Astron. Astrophys.*, accepted for publication on 2016 December 22 (Abstract and Chap. 2): Drs. C. Denker and N. Bello González observed the data in 2008 before I started my doctoral thesis. My contribution to this article were data calibration including image restoration, scientific analysis of the data, writing the manuscript, and preparing the figures, among others. Dr. C. Denker provided guidance during this study, critically read the manuscript, and offered comments and suggestions improving the manuscript.

S.J. González Manrique, C. Kuckein, A. Pastor Yabar, M. Collados, C. Denker, C.E. Fischer, P. Gömöry, A. Diercke, N. Bello González, R. Schlichenmaier, H. Balthasar, T. Berkefeld, A. Feller, S. Hoch, A. Hofmann, F. Kneer, A. Lagg, H. Nicklas, D. Orozco Suárez, D. Schmidt, W. Schmidt, M. Sigwarth, M. Sobotka, S.K. Solanki, D. Soltau, J. Staude, K.G. Strassmeier, M. Verma, R. Volkmer, O. von der Lühe, T. Waldmann: 2016, Fitting Peculiar Spectral Profiles in He I 10830 Å Absorption Features. *Astron. Nachr.* 337, 1057 (Abstract and Chap. 3): I was the principle investigator (PI) of this research project, which included a three-months research visit of the Instituto de Astrofísica de Canarias organized by Drs. C. Denker and M. Collados who also provide guidance and critically read the manuscript. During the GREGOR observing campaign I received help from Drs. C. Kuckein, N. Bello González, R. Schlichenmaier, and C.E. Fischer. At the same time Drs. A. Pastor Yabar and M. Cubas Armas observed the same active region with the Swedish Solar Telescope. Dr. A. Pastor Yabar reduced and calibrated these data. Data of both telescope are also used in Chap. 4. Dr. C.E. Fischer helped aligning the field-of-view of the high-resolution instruments with the synoptic data in Fig. 4.5. Dr. C. Kuckein assisted me in the development of the He I line fitting and commented on the manuscript. Dr. P. Gömöry and A. Diercke helped me downloading the synoptic data and calculating the magnetic flux, which was ultimately included in Chap. 4. The data were taken during the ‘early science phase’ of the GREGOR telescope in 2014/15 and thus included other co-authors from the GREGOR consortium who read the manuscript and offered comments and suggestions. In summary, I wrote the paper, developed the line fitting method, reduced and restored all data from the GREGOR telescope, and carried out the data analysis.

Chapter 4 expands the studies from Chap. 3, and it comprises the major part of a forthcoming peer-reviewed article. In this work Dr. C. Kuckein helped me with the SIR code and NICOLE inversions, teaching me how to use the codes and suggesting appropriate atmospheric models. Dr. M. Verma calculated the horizontal proper motions and created Figs. 4.1 and 4.8. Contributions to synoptic data and data of the Swedish Solar Telescope are already mentioned above. Dr. M. Collados provided ideas how to calculate the approximate distance between the chromosphere and the photosphere. Drs. C. Denker and M. Collados guided me during the process of analyzing these data. I wrote the entire chapter, observed, analyzed, reduced, reconstructed, and interpreted the data. Just a small part of Chap. 4.4 results from a conference proceedings (González Manrique *et al.*, 2017). Here, I analyzed the data and created the figures (Figs. 4.9, 4.10, and 4.11). Dr. C. Denker and I collaborated closely to write this more technical proceedings contribution outlining the ‘very fast spectroscopic mode’ of the GREGOR Infrared Spectrograph.

Abstracts of peer-reviewed articles and conference proceedings, which were not included in the doctoral thesis, are presented in Appendix A.

Chapter 1

Introduction

1.1 Emerging magnetic flux on the solar surface

A very important role in solar physics in general, and in solar activity in particular, is played by the emergence of magnetic flux from the solar interior through the solar surface layers, i.e., photosphere, chromosphere, transition region, and eventually the corona. The emergence of flux becomes possible when high gradients of pressure between different layers of the solar surface exist, and the modes change from a large value of the plasma $\beta = P_{\text{gas}}/P_{\text{mag}}$ (where P_{gas} is the gas pressure and P_{mag} the magnetic pressure) to a plasma β smaller than one (e.g., [Schmieder, Archontis, and Pariat, 2014](#)). In the solar interior between the convection zone and the radiative region (tachocline region) the magnetic field is strongly concentrated (see reviews by [Schmieder, Archontis, and Pariat, 2014](#); [Cheung and Isobe, 2014](#)). The differential rotation of the Sun through solar dynamo processes can convert a fraction of the global kinetic energy of the solar rotation into magnetic energy ([Schmieder, Archontis, and Pariat, 2014](#)). The small-scale magnetic fields emerge from the interior region of the Sun within supergranular cells and are guided by a radial flow pattern to the boundaries of the cells ([Martin, 1988](#)). If the magnetic fields are strong enough, the processes eventually can lead to pores, sunspots, and complex active regions ([Zwaan, 1985](#); [Rezaei, Bello González, and Schlichenmaier, 2012](#)).

There are three main observational rules for the emergence of large-scale bipolar structures. These laws are the base of the dynamo models as summarized by [Mackay and Yeates \(2012\)](#), and [van Driel-Gesztelyi and Green \(2015\)](#). The three laws are (1) Spörer's law ([Carrington, 1858](#)), (2) Joy's law ([Hale *et al.*, 1919](#)) and (3) Hale's law ([Hale and Nicholson, 1925](#)). The butterfly diagram shows a dependence of the latitude of flux emergence with respect to the phase of the solar cycle. When the solar cycle starts, the emergence of active regions appears at higher latitudes, and when the cycle advances, they emerge progressively at lower latitudes. Joy's law describes that bipoles are aligned in the east-west direction with the leading pole always closer to the equator in both hemispheres of the Sun. Hale's law says that the leading magnetic polarities have opposite polarities in opposite hemispheres. These polarities change in the next solar cycle. The tilts and the orientation of the small-scale bipoles do not always follow these laws, and they are more random ([Stenflo, 2014](#)).

1.1.1 Quiet-Sun magnetic fields

[Borrero and Ichimoto \(2011\)](#) summarize the important role of the magnetic field particularly in the Sun but more generally in other stars of the universe. Some of the fundamental properties of plasma and magnetic field, which were summarized by these authors are the following:

- *The magnetic field can guide the plasma capturing the charged particles, e.g., the magnetic field can suppress the plasma convection or can even confine the plasma.*
- *The plasma can expand due to the magnetic pressure and become buoyant.*
- *The MHD waves can be guided by the magnetic field, and it can transfer the the energy to other places.*
- *Dynamics transient events can be produced by the magnetic field that accumulates and liberates energy, for example, in flares.*
- *The polarization properties of the light can be altered or generated by the magnetic field.*

Pieter Zeeman discovered at the end of the 19th century the splitting of spectral lines in the presence of a magnetic field. This Zeeman effect is the key to the discovery of magnetic fields in the sunspots (Zeeman, 1897). The Zeeman effect can be described as the splitting of electronic energy levels and formation of various spectral lines in emission or absorption in the presence of magnetic field, when only a single spectral line was present in the absence of magnetic the field. Another consequence is that the magnetic field modifies the polarization properties of photons depending on the angle between the magnetic field vector and the line-of-sight (LOS) of the observer (Borrero and Ichimoto, 2011).

George Ellery Hale discovered the presence of the magnetic fields in sunspots based on the Zeeman splitting of spectral lines (Hale, 1908). He was able to infer the field strength in sunspots comparing the separation between the spectral components of the spectral lines that he observed and the spectral lines obtained in a laboratory. To infer the magnetic field various techniques are used. With time those techniques evolved and became more sophisticated. It is possible to study the evolution of the LOS component of the magnetic flux, the morphology, and the large-scale distribution by plotting maps of the Zeeman effect circular polarization (Stenflo, 1989). These maps are commonly called magnetograms. An example of a solar full-disk magnetogram taken by Helioseismic and Magnetic Imager (HMI, Scherrer *et al.*, 2012; Schou *et al.*, 2012), on-board the Solar Dynamics Observatory (SDO, Pesnell, Thompson, and Chamberlin, 2012), is represented in the Fig. 1.1. The white areas represent the positive magnetic flux directed towards the observer while the black areas represent the negative flux directed away from the observer. These kind of maps are good to show, where the footpoints of the magnetic fields are located, but they do not provide information if the field lines are connected in other heights of the solar atmosphere below or above (see e.g., Stenflo, 1989).

It is possible not only to calculate the magnetic field strength but the magnetic field vector \vec{B} by using the radiative transfer equation (RTE) for polarized light and the observed Stokes profiles I, Q, U, and V. With the help of inversion codes, e.g., ‘the Stokes inversion code based on response functions’ (SIR, Ruiz Cobo and del Toro Iniesta, 1992) code, the HAanle and ZEeman Light (HAZEL, Asensio Ramos, Trujillo Bueno, and Landi Degl’Innocenti, 2008) code, or the Milne-Eddington Line Analysis using Numerical Inversion Engine (MELANIE, Socas-Navarro, 2001) code, among others, it is possible to infer physical parameters such as temperature, density, LOS velocity, and many others. Continuous measurements of the magnetic field vector is required for the a better understanding of the Sun’s magnetic field (Lites, Martinez Pillet, and Skumanich, 1994). There are some limitations in measuring because low signal-to-noise ratios and the 180° ambiguity make things more complicated or require additional information and techniques. Regular high-resolution spectropolarimetric measurements are taken since the advent of space missions such as Hinode (Kosugi *et al.*, 2007; Tsuneta *et al.*, 2008) and SDO. Typical values of the magnetic field strength B for different magnetic features are: around 2900 G for sunspots with penumbra, near 2200 G for pores, between 1500–2000 G the micro-pores, and 1500 G for flux fibers (Zwaan, 1987). These values can show a very high scatter for individual magnetic features and may differ significantly from the aforementioned values (Pevtsov *et al.*, 2014).

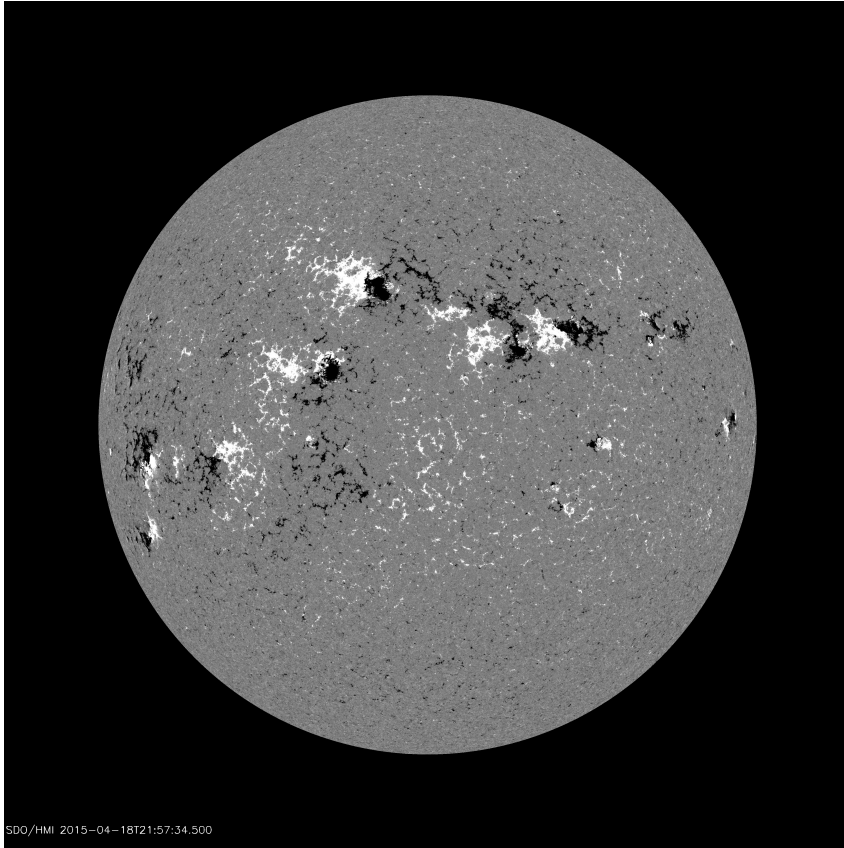


Figure 1.1: Full-disk SDO/HMI LOS magnetogram taken at 21:57 UT on 2015 April 18.

The solar surface is completely covered with different magnetic structures. These magnetic structures on the Sun can occur on a variety of scales, from active regions that can extend for more than 100 Mm (see e.g., [Stein, 2012](#)) to structures that are progressively smaller such as single sunspots, pores, micro-pores, magnetic knots, etc. The observed size of the magnetic structures is limited by the diffraction limit of the largest telescopes (currently around $\sim 60\text{--}70$ km). Depending on the structures the time evolution cover also a wide range. Some active regions can have a live-time of months while smaller magnetic structures live just for a few minutes or even only for seconds ([Stein, 2012](#)). The magnetic field on the solar surface is broadly classified according to active regions and the quiet Sun. Both have a clear origin in the global dynamo ([Stenflo, 2014](#)). The magnetic field observed in the quiet Sun is commonly grouped into network and internetwork. The internetwork quiet-Sun areas cover a very high percentage of the solar surface while the network has a cell diameter around 30 Mm ([Stenflo, 1989](#)). The main observational results show that there are strong vertical magnetic fields but also weaker horizontal magnetic fields associated with the quiet Sun ([de Wijn et al., 2009](#)). The flux extends to the intergranular lanes and is concentrated in the strong vertical field. The field strength is of the order of kilogauss in faculae and bright points (e.g., [de Wijn et al., 2009](#); [Stein, 2012](#); [Stenflo, 2014](#)). The groups of these scattered flux concentrations active regions are called plages ([de Wijn et al., 2009](#)). In the quiet Sun the vertical fields are placed in the magnetic network. This magnetic field network can be seen in various spectral lines and coincides with the emission network ([Stenflo, 1989](#)). The boundaries of the photospheric velocity cells (supergranulation) occupies the same space as the network, and have a lifetime around a day. If the magnetic flux brakes up, it forms smaller cells called mesogranulation with a cell diameter of 1000 km and a lifetime of around 7 min ([Stenflo, 1989](#)). The horizontal magnetic field can be observed all over the Sun but mainly in the quiet Sun ([Trujillo Bueno, Shchukina, and Asensio Ramos, 2004](#); [Harvey et al., 2007](#)). The strongest horizontal fields tend to align with active regions while the weaker fields do not have a clear orientation ([Stein, 2012](#)).

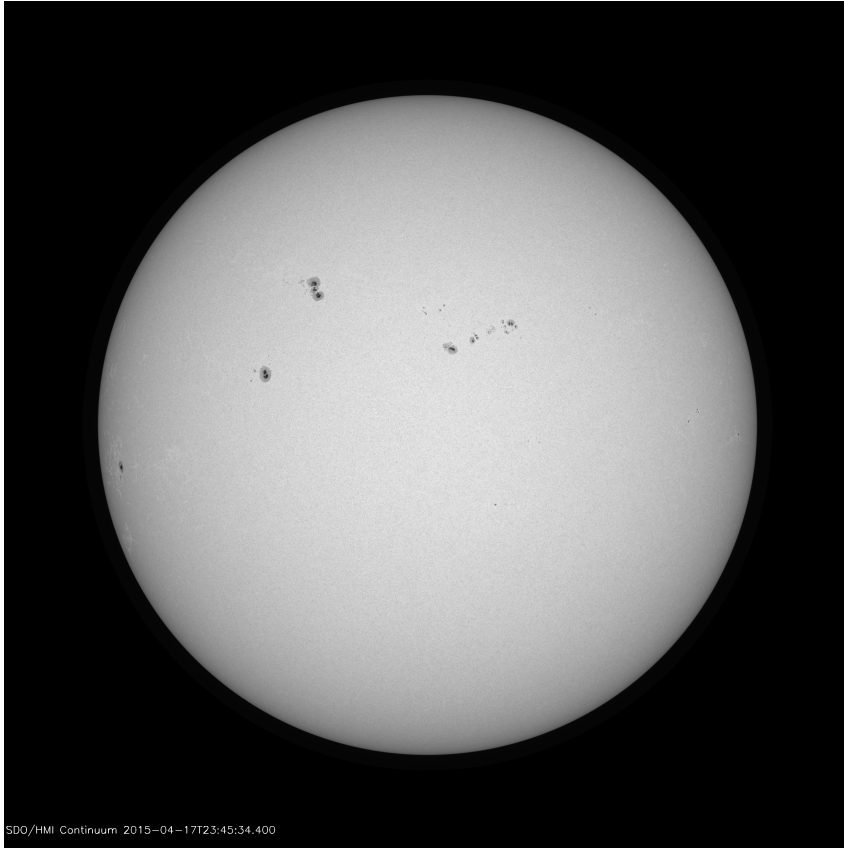


Figure 1.2: Full-disk continuum image from SDO/HMI taken at 23:45 UT on 2015 April 17.

1.1.2 Flux emergence

The generally accepted theory states that emerging flux regions (EFR) are formed by magnetic flux tubes that are transported to the solar surface by buoyancy (Zwaan, 1987). The process forms Ω -loops and can lead to active regions as shown in Fig. 1.2 depicting a full-disk continuum image with different several active regions containing sunspots and pores. After the flux moves through the photosphere, the active regions starts to decay (van Driel-Gesztelyi and Green, 2015). Emerging Ω -loops at granular scale were reported, e.g., by Martínez González *et al.* (2010), and Gömöry *et al.* (2010). The mean velocity of such loops in the photosphere can reach up to 3 km s^{-1} . The upflows' mean velocities are higher in the chromosphere, i.e., around 12 km s^{-1} (Martínez González *et al.*, 2010). The magnetic field at the footpoints is practically vertical when the loops arrive at the upper photosphere. The emerging fields are transported by supergranular flows migrating towards the network (Orozco Suárez, Katsukawa, and Bellot Rubio, 2012). Observations of an EFR in the photosphere show many different temporal and spatial scales. The smallest EFRs can have a lifetime of just a few minutes, while large active regions have a lifetime from days up to weeks (Archontis, 2012). There are EFRs with many sizes, e.g., micro-pores with a radius $R \approx 0.5 \text{ Mm}$, pores with a range between $R \approx 0.7 - 1.8 \text{ Mm}$, or sunspots between $R \approx 2 - 12 \text{ Mm}$. A very wide flux range of all the EFRs are between 10^{18} Mx and $3 \times 10^{22} \text{ Mx}$ (Zwaan, 1987). The EFRs could also lead to eruptive events such as micro-flares, surges, jets, coronal mass ejections, etc.

Many different magnetic field elements with diverse polarities emerge or disappear on the solar surface when the EFRs are forming. In some cases, larger elements evolve into bipolar structures. Smaller magnetic elements can appear and merge with the main bipole or are canceled with opposite polarity elements (Archontis, 2012). Even smaller EFRs follow the Hale-Nicholson law (Tlatov, Vasil'eva, and Pevtsov, 2010) and have the typical magnetic configuration of the solar cycle. These small-scale bipolar magnetic flux concentrations (ephemeral regions) arise all over the solar surface and refill continuously every 14 hours the quiet-Sun magnetic field (Hagenaar, 2001; Guglielmino *et al.*, 2012). The name of 'ephemeral' refers to the short lifetime (~ 12 hours) as compared to the active regions (a few days to several weeks). This lifetime

is defined as the time, when the region still can be recognized as a bipolar structure (Harvey and Martin, 1973; Hagenaar, 2001). In many EFRs the magnetic field between two opposite main polarities can form the well known ‘sea-serpent’ topology (see e.g., Harvey and Martin, 1973; Pariat *et al.*, 2004; Archontis, 2012; Cheung and Isobe, 2014; Schmieder, Archontis, and Pariat, 2014). Approximately ever 10 min, emerging field lines can form a photospheric pattern of aligned dark intergranular lanes (Strous *et al.*, 1996). Magnetic loops are visible in H α when the emerging fields reach chromospheric layers where they form dark fibrils. The plasma progressively drains from the loops. Strong downflows can be caused by this and potentially lead to convective collapse (Cheung *et al.*, 2008). A group of these cool loops are commonly called an arch filament system (AFS) connecting the two opposite-polarity-footpoints. The loops can reach to the photosphere, chromosphere, and corona, where the physical conditions can differ by orders of magnitude in temperature and gas density. In summary, many physical processes play a very important role in the solar atmosphere, e.g., radiation, convection, magnetic field generation/decay, and heat conduction among others. Wedemeyer-Böhm, Lagg, and Nordlund (2009) reviewed the connection between the photosphere, the chromosphere, and the corona. To fully comprehend and follow the dynamics of the solar fine structures, it is very important to observe simultaneously different layers of the Sun with multi-wavelengths observations. The new generation of solar telescopes and their instruments (see Chap. 1.2) allow us the kind of very high resolution observations necessary to observe the dynamics, magnetic field, size, and with inversion codes many other physical parameters are determined. The observations will help us to answer many open solar physics questions related to flux emergence (see the questions raised in the review by Cheung and Isobe, 2014) (1) What are the observational consequences of the emerging flux (Bruzek, 1967; Zwaan, 1978), and what are the physical mechanism responsible (Cheung and Isobe, 2014)? (2) How EFRs evolve with time in the different layers of the solar surface? How are they linked? (3) Is it possible to measure how big the footpoints of the AFSs connected in the different layers of the solar surface are?

1.1.3 Pores and micro-pores

The magnetic solar activity in the photosphere is characterized by various magnetic structures with a wide range of spatial sizes and diameters. When the magnetic field is strong and the value of the filling factor is high enough, micro-pores are visible in the photosphere. They appear as a signature of flux emergence (Scharmer *et al.*, 2002; Rouppe van der Voort *et al.*, 2005). It is the same case for pores, if the convection and thus the plasma motions are inhibited by a strong magnetic field, pores and eventually sunspots can be formed (Sobotka, 2003). The effective temperature of pores is still relatively hot, which means that the convective energy transfer is not fully suppressed. The pores are considered intermediate-sized emerging magnetic features (Sobotka *et al.*, 2012). They can be isolated features or emerge near sunspots, and not all pores evolve into sunspots (Keil *et al.*, 1999), as seen in two examples in Fig. 1.3. Micro-pores are at the very limit part of the statistical size distribution of pores (Verma and Denker, 2014). Once pores are present, sunspots are eventually formed by coalescence of newly emerged flux (Schlichenmaier *et al.*, 2010; Rezaei, Bello González, and Schlichenmaier, 2012). Pores normally are defined based on their continuum intensity. The continuum intensity varies from 20 – 80 % of the quiet-Sun continuum intensity (Hirzberger, 2003; Sobotka, 2003; Verma and Denker, 2014). The diameter of pores varies from study to study, but all authors agree that the maximum diameter is a few megameters, typically less than 4 Mm (e.g., Rucklidge, Schmidt, and Weiss, 1995; Keppens and Martinez Pillet, 1996; Sütterlin, 1998; Hirzberger, 2003; Sobotka *et al.*, 2012; Quintero Noda *et al.*, 2016) but always a few thousand of kilometers smaller than the sunspots (Morinaga *et al.*, 2008). The magnetic field radius is always larger than the continuum radius and implies that a magnetic canopy exists (Keil *et al.*, 1999). The lower limit of pores and some micro-pores can have the same size as the granules, i.e., a diameter typically smaller than 1'' (Rouppe van der Voort *et al.*, 2006). As a consequence, observations with a very high-resolution are needed (Keil *et al.*, 1999). Micro-pores change their appearance between circular magnetic structures (flowers) and elongated features that are dark in the center and brighter at the borders

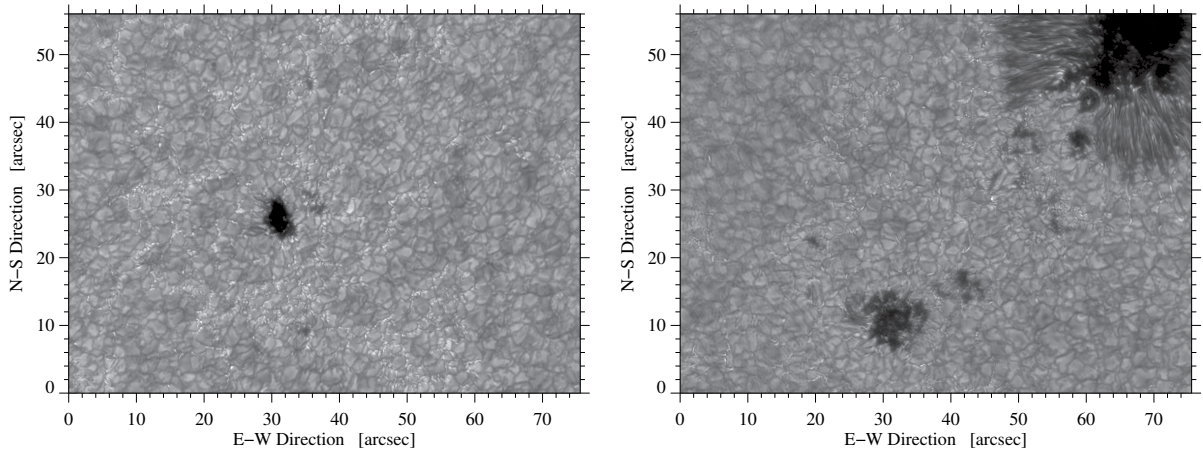


Figure 1.3: Left: Example of an isolated pore observed with a broad filter 5434 Å Fe I on 2014 August 4 at 08:31 UT with the Blue Imaging Channel (BIC) (see Chap. 1.3.1). Right: Example of a pore close to a sunspot observed with a G-Band 4307Å filter on 2014 August 26 at 08:24 UT with BIC.

(ribbons). The nomenclature is based on G-band data presented by [Roupe van der Voort *et al.* \(2005\)](#).

One of the main characteristics that differentiates between pores and sunspots is the absence of a filamentary penumbra in pores. Nevertheless, high-spatial resolution revealed diverse bright features like light-bridges or umbral dots ([Sobotka *et al.*, 2012](#)) and may indicate a mechanism of convective energy transportation (e.g., [Sobotka *et al.*, 1999](#); [Keil *et al.*, 1999](#); [Hirzberger, 2003](#); [Rucklidge, Schmidt, and Weiss, 1995](#)). The absence of filamentary structure in pores may suggest a simple magnetic structure of flux tubes with a vertical magnetic field (e.g., [Simon and Weiss, 1970](#)). However, the magnetic field lines near the borders of the pores are inclined between $40^\circ - 80^\circ$ ([Keil *et al.*, 1999](#)). The magnetic field measured across the pores indicates that it varies between 600 – 1700 G (e.g., [Sütterlin, Schröter, and Muglach, 1996](#); [Keppens and Martinez Pillet, 1996](#); [Sütterlin, 1998](#)). [Quintero Noda *et al.* \(2016\)](#) found in the center of the pore strong LOS field strengths larger than 2000 G in the lower parts of the photosphere and around 1000 – 1500 G in upper layers using a new technique of a spatially deconvolution of a solar pore. In the case of bigger pores the magnetic field range can reach up to 2000 G ([Zwaan, 1987](#)).

The LOS velocities and horizontal motions inside the concentrated magnetic field of pores are zero for all height layers, and the observed downflows in the surroundings are close to zero or exhibit small upward velocities at middle layers ([Sobotka *et al.*, 2012](#); [Quintero Noda *et al.*, 2016](#)). Similar results were found for the micro-pores with small fluctuations of around 0.1 km s^{-1} ([Roupe van der Voort *et al.*, 2006](#)). In contrast, the downward LOS velocities near the pores have a range around $0.5 - 2 \text{ km s}^{-1}$ (e.g., [Brants and Steenbeek, 1985](#); [Leka and Skumanich, 1998](#); [Hirzberger, 2003](#)). [Verma and Denker \(2014\)](#) calculated the horizontal velocities of more than 2000 pores. They discussed two examples in detail, one isolated pore and a pore resulting from a decaying sunspot that they called “residual pore”. Both pores have inflows in the center and outflows in the surroundings. The mean horizontal velocities for the isolated pore is $v_{\text{mean}} = 0.18 \text{ km s}^{-1}$ and for the residual pore $v_{\text{mean}} = 0.29 \text{ km s}^{-1}$. The horizontal motion around isolated pores can reach up to 0.7 km s^{-1} .

Simulations by [Cameron *et al.* \(2007\)](#) of a pore and its surroundings showed downflows up to 1 km s^{-1} . This agrees with observations of not only the LOS velocities but also of the average magnetic field around $2000 \pm 300 \text{ G}$, and of a field inclination larger than 50° . There are two main groups of theoretical models that agreed with the observations ([Sobotka *et al.*, 2012](#)). The first model considers a bundle of spaghetti-like flux tubes. They are separated by field-free plasma that can penetrate the layers close to the visible surface (e.g., [Severnyi, 1965](#); [Parker, 1979](#); [Choudhuri, 1986](#)). The second theory consists of a inhomogeneous and monolithic flux

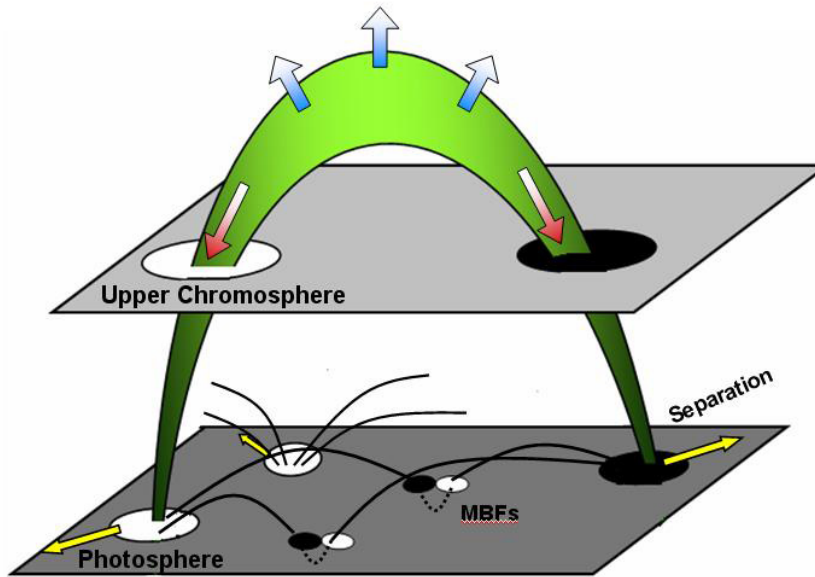


Figure 1.4: The schematic sketch depicts the magnetic field observed within an emerging flux region. The lower layer represents the photosphere and the upper layer the average chromosphere. The dark and the white circular refer to negative and positive polarities, respectively. The green arch filament depicts an emerging magnetic loop connecting two opposite polarities going from the photosphere into the upper chromosphere. The photospheric footprints move in opposite directions as indicated by the yellow arrows. The red and blue arrows illustrate the downflows and upflows commonly observed in the arch filaments in the upper chromosphere. (Fig. 13 in [Xu, Lagg, and Solanki, 2010](#)).

tube with interior magnetoconvection. This model allows a plasma that can be modified by the magnetic field and vice versa (e.g., [Hurlburt and Rucklidge, 2000](#); [Thomas and Weiss, 2004](#)).

1.1.4 Chromospheric response

Compared to the photosphere, the chromosphere is very inhomogeneous (e.g., [Contarino *et al.*, 2009](#)). There are several features that can be observed. Some of the main features are: spicules, dynamic fibrils, mottles connected by AFSs and quiet-Sun or active-region filaments, among others. Filaments are also called prominences when observed in emission above the limb (see [Mackay *et al.*, 2010](#), for a review). Spicules are jet-like structures observed at the solar limb and also sometimes on the disk as filamentary structures. They appear in regions with high magnetic flux ([Beckers, 1972](#)). These structures can have vertical extensions between 5 – 10 Mm and have lifetime of around 5 – 15 min ([Contarino *et al.*, 2009](#)). In active regions it is possible to see dynamic fibrils with a very small size of the order of about 1250 km. These fibrils have diameters is between 100 – 700 km and a lifetime of 3 – 6 min. ([Contarino *et al.*, 2009](#)). Elongated dark structures placed in the quiet Sun are called mottles. Their heights can reach up to 10 Mm and their widths between 500 – 2000 km. They have very short lifetimes of 5 – 10 min. Another chromospheric feature are groups of mottles called chains or rosettes ([Contarino *et al.*, 2009](#)). With regard to the topic of this thesis we distinguish between AFSs and filaments. Their structure depends on the magnetic field configuration, specifically at their photospheric footprints. Filaments are formed of cool dense plasma and are located between opposite polarities (e.g., [Tandberg-Hanssen, 1995](#); [Mackay *et al.*, 2010](#); [Kuckein, Martínez Pillet, and Centeno, 2012a](#)) along the polarity inversion line (PIL, [Babcock and Babcock, 1955](#)). In contrast to filaments, AFS cross the PIL connecting two opposite polarities of newly emerging flux regions ([Bruzek, 1969](#)).

Quiet-Sun filaments have typically a length of 60–600 Mm although longer ones exist (cf., [Kuckein, Verma, and Denker, 2016](#)), reach heights around 100 Mm, and possess lifetimes up to a few weeks ([Tandberg-Hanssen, 1995](#)). Active-region filaments are shorter with a size of around

10 Mm and lifetimes from a few hours up to several days (Mackay *et al.*, 2010). Several studies were carried out to investigate the magnetic field in filaments. In particular, Bommier, Rayrole, and Eff-Darwich (2005) inferred the magnetic field of an active-region filament in the photosphere with values around 100 G. Higher values of the magnetic field (600 – 800 G), and with the field lines oriented mainly horizontal, were reported by Kuckein *et al.* (2009) and Kuckein, Martínez Pillet, and Centeno (2012a). The latter observed very strong sheared magnetic fields in the chromosphere and two days after a sheared magnetic field in the photosphere. Xu *et al.* (2012) reported a range of magnetic field between 200 – 800 G depending on the region within the active-region filament. The magnetic fields of the quiet-Sun filaments are mainly horizontal with range between 3 to 15 G. Supersonic downflows up to 100 km s⁻¹ in the filaments at the upper chromosphere were found by Sasso, Lagg, and Solanki (2011, 2014), while Kuckein, Martínez Pillet, and Centeno (2012b) reported supersonic photospheric downflows near the PIL and very weak upflows below the filament. Horizontal motions and LOS velocities in quiescent filaments are of the order of 10 – 70 km s⁻¹ (see Mackay *et al.*, 2010, and references therein).

Howard and Harvey (1964) for the first time distinguished between fibrils or arch filaments and filaments. While filaments lie above the PIL, fibrils cross perpendicularly to it. Martres, Michard, and Soru-Iscovici (1966) observed fibrils connecting two opposite polarities. Bruzek (1967) reported these system of fibrils for the first time and called it AFS. The AFSs are prominently visible in line-core filtergrams of the strong chromospheric absorption line H α and also, but less pronounced, in the line core of the Ca II H & K lines (Bruzek, 1969). More recently they were observed in the He I 10830 Å triplet (e.g., Solanki *et al.*, 2003; Spadaro *et al.*, 2004; Lagg *et al.*, 2007; Xu, Lagg, and Solanki, 2010; Vargas Domínguez, van Driel-Gesztelyi, and Bellot Rubio, 2012; Ma *et al.*, 2015). Figure 1.4 illustrates the loop of a theoretical arch filament connecting the two opposite polarities in the photosphere and the chromosphere. The arch filaments are normally confined below 10 Mm. Bruzek (1969) determined the length of the arch filaments up to the size of supergranular network cells (20–30 Mm). Typically, the width of single AFS loops is only a few megameters, and the height of the arches varies between 5–15 Mm with a lifetime of about 30 min (Bruzek, 1967). However, some individual loops of the AFS can reach heights close to 25 Mm and lengths near 20–40 Mm (Tsiropoula *et al.*, 1992). Generally, the appearance of an AFS does not change for many hours. However, significant changes can occur along with the growth of the sunspot group. The AFS vanishes around three days after its formation. Spadaro *et al.* (2004) studied the evolution and dynamics of an AFS. They reported upflows in the center of the arches and downflows at the footpoints. Downflows reach velocities in the range of 30–50 km s⁻¹. They were observed near both footpoints of the AFS, whereas loop tops rise with about 1.5–20 km s⁻¹ (Bruzek, 1969; Zwaan, 1985; Chou and Zirin, 1988; Lites, Skumanich, and Martinez Pillet, 1998). Some other studies of AFS based on the He I triplet reported downflows from 40–90 km s⁻¹ (e.g., Teriaca *et al.*, 2003; Aznar Cuadrado, Solanki, and Lagg, 2005, 2007; Sasso *et al.*, 2007; Lagg *et al.*, 2007).

In the past it was not easy to infer the magnetic field with the spectral lines typically used to observe an AFS (Socas-Navarro and Uitenbroek, 2004). Studies containing the magnetic field vectors based on the full Stokes profiles of the He I 10830 Å triplet were reported, for example, by Solanki (2003) and Lagg *et al.* (2004, 2007). The He I triplet is a very important tool to study the magnetic features in the chromosphere, and particularly the AFS (Lagg *et al.*, 2007; Xu, Lagg, and Solanki, 2010). Solanki (2003) reported magnetic field strengths in the footpoints between 390–500 G while it decreases in both legs down to 50 G. Magnetic field strength values up to 1200 G were reported by Lagg *et al.* (2007) in the regions with very high velocities, typically located at the footpoints. Xu, Lagg, and Solanki (2010) reconstructed the three-dimensional (3D) magnetic field in an AFS. They assumed that the He I 10830 Å triplet is formed along the magnetic field loops.

1.1.5 Theoretical models of flux emergence

Magnetohydrodynamics (MHD) simulations are an important to deepen our physical understanding of processes on the Sun. We briefly introduce the latest theoretical works, for example

related to emerging magnetic flux. Commonly, the MHD equations are used to describe the evolution of the buoyant rise of the magnetic field lines and their interaction with the surrounding medium (e.g., [Cheung and Isobe, 2014](#)). These equations are nonlinear, and they require simulations to study the evolution of the entire system. [Cheung and Isobe \(2014\)](#) reviewed the physical principles of the MHD equations as follows (see also references therein):

- *the principle of mass conservation*
- *the principle of momentum conservation*
- *the principle of energy conservation*
- *Faraday's law of electromagnetic induction*

They summarized the MHD equations in the context of continuum mechanics and in a Lagrangian notation. The Eulerian notation is also used for the implementation of numerical simulation codes. With the Lagrangian MHD equations it is possible to simulate the evolution of individual flux tubes going through the solar convection zone, and it describes the magnetic flux emergence (e.g., [Moreno-Insertis, 1997](#); [Fan, 2009](#)).

[Stein \(2012\)](#) mentioned the three different initializations of the simulations of emerging magnetic flux from the layers of the convection zone. The first initialization assumes a coherent twisted flux tube. It is forced through the bottom boundary into the computational domain or by lowering their density to make it buoyant (e.g., [Cheung, Schüssler, and Moreno-Insertis, 2007](#); [Cheung et al., 2008](#); [Martínez-Sykora, Hansteen, and Carlsson, 2008, 2009](#); [Cheung et al., 2010](#)). The second one assumes that the flux tube emergence produced locally by a dynamo action ([Abbett, 2007](#); [Abbett and Fisher, 2010](#)). The third one assumes that a minimally structured, untwisted, uniform, and horizontal magnetic field is advected into the domain by inflows at the bottom ([Stein et al., 2011, 2012](#)).

[Rempel and Cheung \(2014\)](#) reported on recent 3D simulations of different features of the solar surface related to active regions. Sunspots including umbra were simulated by e.g., [Rempel et al. \(2009\)](#), [Rempel \(2011\)](#), with penumbra e.g., [Kitiashvili et al. \(2010a\)](#), [Rempel \(2012\)](#), and sunspots including light bridges by [Cheung et al. \(2010\)](#). Simulations including pores were simulated by e.g., [Kitiashvili et al. \(2010b\)](#), [Stein and Nordlund \(2012b\)](#), including plages [Vögler et al. \(2005\)](#) and simulating some anomalous features within the solar granulation related to the emerging flux e.g., [Tortosa-Andreu and Moreno-Insertis \(2009\)](#), [Fang et al. \(2012\)](#).

The aforementioned simulations reveal the following: [Cheung et al. \(2010\)](#) was able to reproduce some of the observational properties of magnetic flux emergence like mixed polarities in EFRs, pore formation, or elongated granules. From a depth in the convection zone of 7.5 Mm they kinematically advected a magnetic semi-torus upward to the photosphere. [Rempel and Cheung \(2014\)](#) extended this study. They introduced the evolution and emergence of buoyant flux under the assumption of coherent twisted flux tubes. [Stein et al. \(2011\)](#) simulated flux emergence that rises through the upper convection zone and penetrates the solar surface. The initial rise and evolution is based on a uniform, untwisted, and horizontal magnetic flux tube with the same entropy as the nonmagnetized plasma. The simulation was carried out by upflows into a domain of 48 Mm wide and a depth of 20 Mm. Concerning the simulations of the pores [Stein and Nordlund \(2012b\)](#) also used a horizontal magnetic field that rises from a depth of 20 Mm below the photosphere within a 48-Mm-wide box. The bottom and top boundaries were open and the horizontal boundaries periodic. After two days a pore was formed spontaneously in some of the vertical flux concentrations of the emerging loops. These simulations included a magnetic field that slowly increased from 200 G to 1 kG with a time-range of around 5 hours. The maximum magnetic flux was 2×10^{20} Mx with vertical magnetic field lines in the pore and field lines inclined by more than 45° near the edges. The lifetime of the pores was around



Figure 1.5: The VTT at Observatorio del Teide, Tenerife. Image courtesy of Christoph Kuckein.

10 hours. As mentioned in Chap. 1.1.3, [Cameron *et al.* \(2007\)](#) computed radiative MHD simulations that reproduce many observed properties of solar pores such as density, mean height profiles of temperature, morphology, continuum intensity, pressure, surrounding flow pattern, and magnetic field geometry. They used the MURaM code (MPS/University of Chicago RAdiative MHD, [Vögler and Schüssler, 2003](#); [Vögler, 2005](#)) to simulate many pores of different sizes and with diverse boundary conditions. [Kitiashvili *et al.* \(2010b\)](#) employed realistic radiative 3D MHD simulations to study the interaction between the turbulent convection and the magnetic field. They imposed weak a vertical uniform magnetic field in a region with granular convection. In addition, at the bottom and top boundaries they applied a constant magnetic flux. They obtained spontaneous formation of stable magnetic structures, and they claim that this spontaneous formation is one of the keys to understand the magnetic organization of the Sun and the formation of pores and eventually sunspots. The maximum magnetic field strength of the pores obtained at the solar surface reaches up to 1.5 kG while at the solar interior it is around 6 kG. The simulated magnetic features remained stable for several hours without any sign of decay.

1.2 Solar telescopes

1.2.1 Vacuum Tower Telescope

The 70 cm Vacuum Tower Telescope (VTT) in Fig. 1.5 was designed in 1973 by Dr. J.P. Mehlretter at the Kiepenheuer-Institut für Sonnenphysik (KIS). The project was funded as the “Hilfseinrichtung Sonnenphysik” by the Deutsche Forschungsgemeinschaft. It included the former Gregory-Coudé Telescope (GCT) 2002, the GTC was replaced by the 1.5 meters GREGOR telescope. The construction of the VTT started in 1983 and finished 1987 and it had the first light in 1987. It is located at the Observatorio del Teide (OT), Tenerife, Spain. It is located at coordinates $28^{\circ}18'$ North and $16^{\circ}30'$ West at an altitude of 2390 m. The building has a height of 38 m with the dome closed ([Schmidt and Soltau, 1987](#)).

The VTT has a coelostat consisting of two mirrors with a diameter of 80 cm, a 75 cm window for the evacuated telescope tank with a length of 25 m and a diameter of 2 m. At the end of the tank is one parabolic primary mirror of 70 cm that it is mounted in an off-axis configuration. Its focal length is 45.64 m with the possibility to observe a field-of-view (FOV) of around 10 arcmin at the primary focus (plate-scale of $4.52'' \text{ mm}^{-1}$). The VTT has two optical laboratories with space for large instruments and optical benches for experimental setups ([von der Lühne, 1998](#)). Real-time image correction is provided by the Kiepenheuer Adaptive Optics System (KAOS, [von der Lühne *et al.*, 2003](#); [Berkefeld *et al.*, 2010](#)), developed at KIS, and it became operational in 2001. With the Adaptive Optics (AO) system, it is possible to observe small-scale solar features with a much improved spatial resolution. KAOS is situated near the telescope focus on an optical bench, containing a camera mirror and a collimator producing a 50 mm diameter pupil on the deformable mirror.



Figure 1.6: GREGOR telescope at the Observatorio del Teide, Tenerife. Image courtesy of Christoph Kuckein.

The VTT hosted and still hosts several post-focus instruments. One of them was the Göttingen Fabry-Pérot Interferometer (FPI) (Bendlin, Volkmer, and Kneer, 1992; Puschmann *et al.*, 2006; Bello González and Kneer, 2008). The Göttingen FPI was designed for very high resolution. In the context of this doctoral thesis it was used to study two small micro-pores in a small EFR in Chaps. 4 and 5. High resolution spectroscopy is one of the key applications of the VTT. Other post-focus instruments of the VTT are the Telecentric Etalon Solar Spectrometer (TESOS, Kentischer *et al.*, 1998), the polarimetric Littrow Spectrograph (POLIS, Schmidt *et al.*, 2003), the high-resolution Echelle spectrograph including a slit-jaw imaging system (Schröter, Soltau, and Wiehr, 1985), or the HELioseismological Large Regions Interferometric DEvice (HELLRIDE, Staiger, 2012a,b).

1.2.2 GREGOR telescope

The 1.5-meter GREGOR solar telescope (e.g., Schmidt *et al.* (2012); Denker *et al.* (2012); Kneer (2012) replaced the GCT at Observatorio del Teide, Tenerife, Spain. It is the largest solar telescope constructed in Europe and one of the largest in the world. Three imaging mirrors, which are called a double Gregory System, are part of the optical design (Soltau *et al.*, 2012). The overall design is based on concepts for an open telescope, i.e., the Large Earth-based Solar Telescope (LEST, Andersen, Engvold, and Owner-Pedersen, 2002). The scheme of the optical train of GREGOR is shown in Fig. 1.7. The dome of the telescope consists of a foldable tent (Hammerschlag *et al.*, 2012). Information of the mechanical design can be found in Volkmer *et al.* (2012).

Much effort went into the design and construction of the primary mirror. It was made from Zerodur ceramics (Volkmer *et al.*, 2010b,a) and has a diameter of $D_1 = 1500$ mm (clear aperture 1440 mm) and a focal length of $f_1 = 2500$ mm (von der Lühse *et al.*, 2001). An image with a diameter of 25 mm is formed in the primary focus, where a total power of nearly 2000 W is concentrated and the flux density amounts to 6 MW m^{-2} (Schmidt *et al.*, 2012). Initially, in the optical design of the primary, secondary, and tertiary mirrors the mirror substrate was Cesium ceramics (Volkmer *et al.*, 2003a, 2006; Krödel, Luichtel, and Volkmer, 2006). This advanced material can be more effectively cooled. In addition, the mirror seeing is reduced and the weight of the mirror is smaller (Volkmer *et al.*, 2003b). However, the technology was not evolved enough to create such a large mirror as the primary mirror. Only the secondary ($D_2 = 400$ mm, $f_2 = 520$ mm) and the tertiary ($D_3 = 300$ mm, $f_2 = 1400$ mm) mirrors were made out

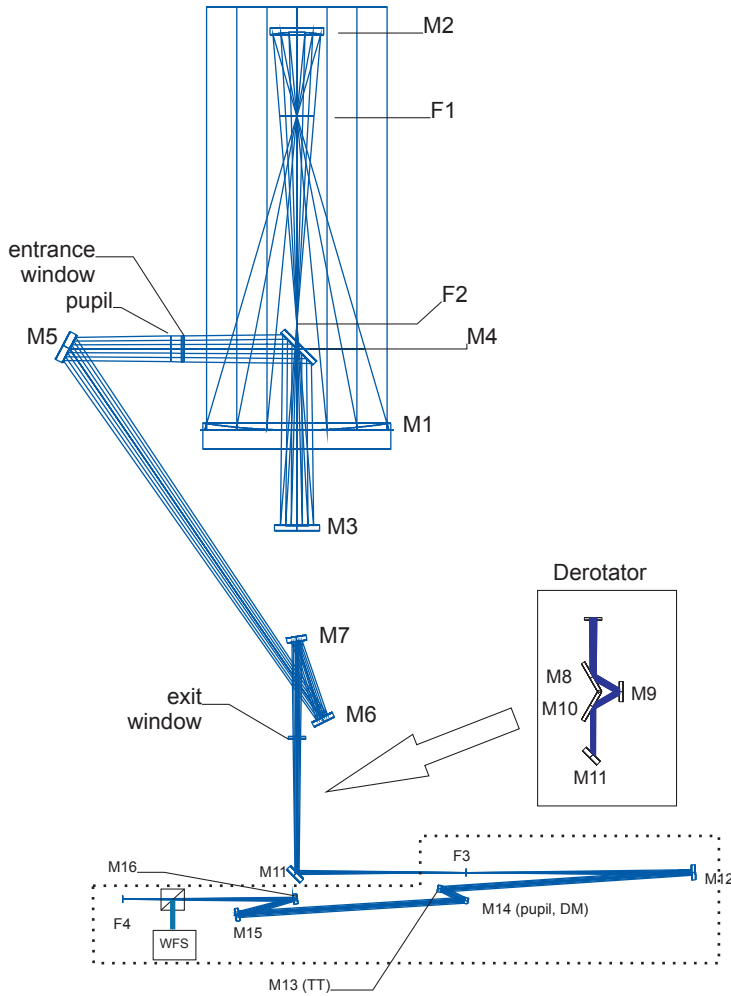


Figure 1.7: Scheme of the optical train of the GREGOR telescope (Fig. 3 in [Soltau et al., 2012](#)).

of this material. Even these smaller mirrors were replaced or are in the process to be replaced because their surface quality and roughness was not optimal.

The GREGOR telescope benefits from advanced real-time image correction provided by the GREGOR Adaptive Optics System (GAOS, [Berkefeld et al., 2012](#)). The typical day time seeing conditions at Observatorio del Teide have a Full-Width-at-Half-Maximum (FWHM) of $1.2''$ for the seeing disk with a blurring value of $\sigma = 0.5''$ ([Brandt and Wöhl, 1982](#)). Therefore, large-aperture telescopes are almost always seeing limited, especially for observations in the visible light. As a consequence, powerful AO systems have been developed over past two decades providing real-time correction. GAOS allows to observe high-spatial resolution images approaching the diffraction limit of the telescope. The theoretical diffraction limit of GREGOR is $0.07''$ at a wavelength of 5000 \AA ([Berkefeld et al., 2012](#); [Schmidt et al., 2012](#)).

The GREGOR telescope is equipped with the GREGOR Polarimetric Unit (GPU) located in the light beam between M_2 and M_3 near F_2 ([Hofmann et al., 2012](#)). The GPU can be used to calibrate the data taken with all post-focus instruments for the visible and near infrared (NIR). There are three operational post-focus instruments at GREGOR. The GREGOR Fabry-Pérot Interferometer (GFPI, [Denker et al., 2010](#); [Puschmann et al., 2012](#)), the Broad-Band Imager (BBI, [von der Lühe et al., 2012](#)), and the GREGOR Infrared Spectrograph (GRIS, [Collados et al., 2012](#)). The GFPI and BBI are completely placed at the fifth floor of the GREGOR building, whereas GRIS is mainly located on the fourth floor ([Volkmer et al., 2006](#)). From the observing room it is possible to control all the instruments thanks to the GREGOR telescope control system ([Halbgewachs et al., 2012](#)). Dichroic pentaprisms are used to split the light between the NIR and the visible wavelengths. In the near future, the GREGOR telescope will be capable to perform night observations ([Strassmeier et al., 2012](#); [Granzer et al., 2012](#)).

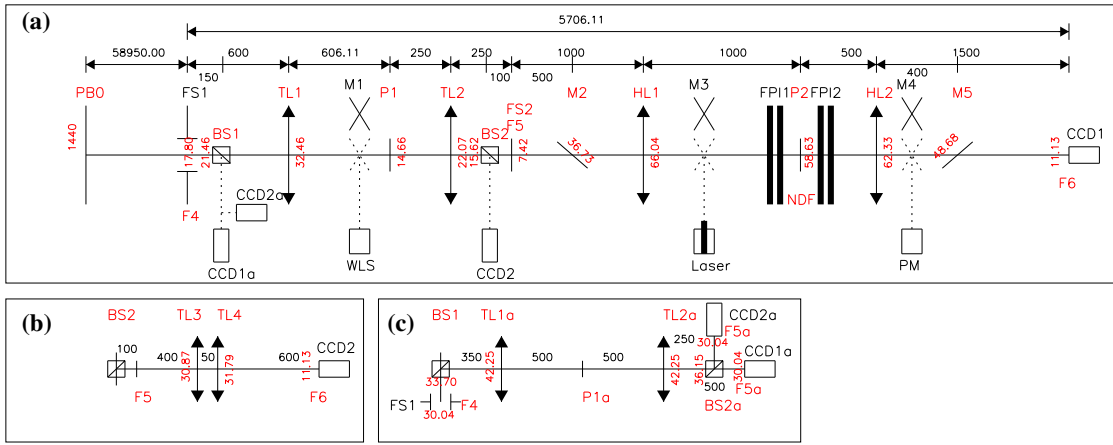


Figure 1.8: Scheme of the main channels of the GFPI (Fig. 1 in [Puschmann et al., 2012](#)): (a) the narrow-band channel, (b) the broad-band channel, and (c) the blue imaging channel. All the distances between optical elements are shown in millimeters.

The science verification phase started in spring 2012 and the first early science observations started in spring 2014. The science goals of the GREGOR telescope are summarized in the GREGOR proposal by [Schmidt et al. \(2012\)](#) and listed by [Denker et al. \(2012\)](#) as:

- The interaction between convection and the magnetic field in the photosphere*
- Solar magnetism and its role in driving solar variability*
- The enigmatic heating mechanism of the chromosphere*
- The search for solar twins during nighttime*

1.3 Instruments

1.3.1 The GREGOR Fabry-Pérot Interferometer

One of the significant post-focus instruments of solar telescopes are imaging spectropolarimeters. Such instruments support image restoration techniques and have a better photon-efficiency than long-slit spectrographs. For more than 20 years these kind of instruments are used at various solar telescopes, e.g., the Göttingen FPI ([Bendlin, Volkmer, and Kneer, 1992](#); [Puschmann et al., 2006](#); [Bello González and Kneer, 2008](#)), also TESOS ([Kentischer et al., 1998](#)), both at the VTT, the CRisp Imaging SpectroPolarimeter (CRISP) described by [Scharmer \(2006\)](#) and [Scharmer et al. \(2008\)](#) at the Swedish Solar Telescope (SST, [Scharmer et al., 2003](#)), the Interferometric Bidimensional Spectrometer (IBIS, [Cavallini, 2006](#)) at the Dunn Solar Telescope (DST), the Visible-light and NIR Imaging Magnetographs (VIM and IRIM, [Denker et al., 2003](#)) at the Big Bear Solar Observatory (BBSO), the Imaging Magnetograph eXperiment (IMaX, [Martínez Pillet et al., 2011](#)) for the Sunrise balloon-borne solar observatory ([Barthol et al., 2010](#)), and finally the GFPI, one of the first-light instruments of the 1.5-meter GREGOR solar telescope.

The GREGOR FPI as the successor of the Göttingen FPI was described in [Puschmann et al. \(2007\)](#). The Göttingen FPI was originally developed by the Institute for Astrophysics Göttingen. In 2009 the Leibniz-Institut für Astrophysik Potsdam(AIP) became in charge of the instrument, and it was installed at the GREGOR telescope and had its first light in 2012.

Just before the light enters the main optical path of the GREGOR FPI as shown in Fig. 1.8, two pentaprisms placed before the science focus F4 split the light. The infrared light is transmitted to GRIS and the visible light is reflected towards GFPI. The main optical path includes

the narrow- and broad-band channels. The incoming light is transmitted by a beamsplitter (BS2 in Fig. 1.8), so that 95% of the light is transmitted to the narrow-band channel and the remaining 5% of the light is directed to the broad-band channel (Denker *et al.*, 2010). The etalons manufactured by IC Optical Systems LtdIn are placed the collimated beam near the pupil. The free aperture of both etalons is $\varnothing = 70$ mm, and the plates spacing are $d_1 = 1.101$ mm and $d_2 = 1.408$ mm, respectively. The GFPI covers the wavelength range of 5300 – 8600 Å with a very high reflectivity $R \sim 0.95$ and a FWHM = 28 – 75 mÅ resulting in a spectral resolutions of the instrument of $\mathcal{R} \approx 250.000$. The effective finesse is $\mathcal{F}_{\text{eff}} \geq 40$. The two etalons functions as tunable filters to scan along a previously selected spectral line. For a proper performance and stability of the GFPI, the environmental conditions should be as stable as possible, i.e., humidity, air pressure, and temperature should remain constant. To protect the instrument from dust contamination the optical tables are enclosed in a black aluminum box. Additionally, the etalons are covered with a thermally insulated box.

The detectors for the narrow- and broad-band channels are two Imager QE CCDs from La Vision GmbH with a Sony ICX258A chip, which has 1376×1040 pixels. The pixel size is $6.45 \mu\text{m} \times 6.45 \mu\text{m}$. The instrument has an image scale of $0.0361'' \text{ pixel}^{-1}$ and a FOV of $52.2'' \times 39.5''$. Using the full resolution the frame rate can reach up to 10 Hz, which can be doubled using 2×2 binning.

It is possible to insert a full Stokes polarimeter in the narrow-band channel of the GFPI. It uses ferroelectric liquid crystal retarders (FLCRs) for modulation. The nominal retardance of the first FLCR is $\lambda/2$ (half-wave) plate and the second one acts as a $\lambda/4$ (quarter-wave) plate. After the modulator a modified Savart plate is placed, which functions as a polarizing beamsplitter. The Savart plate contains two calcites and a half-wave plate is placed between them. The polarimeter can measure four modulation states in every wavelength point, thus representing a linear combination of the four components of the Stokes vector (Denker *et al.*, 2010; Balthasar *et al.*, 2011; Puschmann *et al.*, 2012). After demodulation it is possible to derive the full Stokes vector for every spectral scan. The FLCRs were tested and optimized for the wavelength range 580–660 nm. The FOV is reduced in the polarimetric mode to $24'' \times 38''$.

Another dichroic beamsplitter (BS1 in Fig. 1.8) deflect the light to the Blue imaging channel (BIC). The wavelengths available in this channels are below 530 nm. An additional beamsplitter transmits 50% of the light to each of the PCO.4000 cameras. The chip has 4008×2672 pixels but because of the vignetting of the beamsplitters only 2000×2672 pixels can be used (Puschmann *et al.*, 2013). The pixel size is $9 \mu\text{m} \times 9 \mu\text{m}$, and the image scale is $0.0315'' \text{ pixel}^{-1}$. The FOV of both cameras is $63'' \times 84''$ and can record more than 30 images in less than 15 s (Puschmann *et al.*, 2012). Various interference filters are available for use in BIC, e.g., blue continuum (450.6 nm), Ca II (396.8 nm), and Fraunhofer G-band (430.7 nm) (Puschmann *et al.*, 2013). The software package DaVis from LaVision in Göttingen facilitates the communication between the devices of the telescope and the devices of the GFPI, e.g, cameras, etalons, filters, etc. (Puschmann *et al.*, 2012). Soon the software will be upgraded to DaVis 8. Recently, AIP acquired two new imager sCMOS cameras (repackaged PCO.edge 5.5 detectors) from LaVision for BIC. The new sCMOS cameras are a major improvement over the old PCO cameras. The camera chip is 2560×2160 pixels large, with the pixel size of $6.5 \mu\text{m} \times 6.5 \mu\text{m}$. The spectral range is between 370–1100 nm. The frame rate with the maximum resolution of the camera is 50 frames s^{-1} and thus much faster than the old PCO cameras. The fast frame rate will allow to acquire more images and select the best ones to achieve better reconstructions and to improve the spatial resolution and contrast of the images. The image reconstruction techniques include post-processing with Multi-Object Multi-Frame Blind Deconvolution (MOMFBD, Löfdahl, 2002; van Noort, Rouppe van der Voort, and Löfdahl, 2005) and speckle techniques (e.g., KISIP, Wöger and von der Lühe, 2008; Wöger, von der Lühe, and Reardon, 2008).

1.3.2 The GREGOR Infrared Spectrograph

The GRIS (Collados *et al.*, 2008, 2012) was developed by the Instituto de Astrofísica de Canarias (IAC). Attached to the spectrograph is an infrared camera, which was formerly operated at the

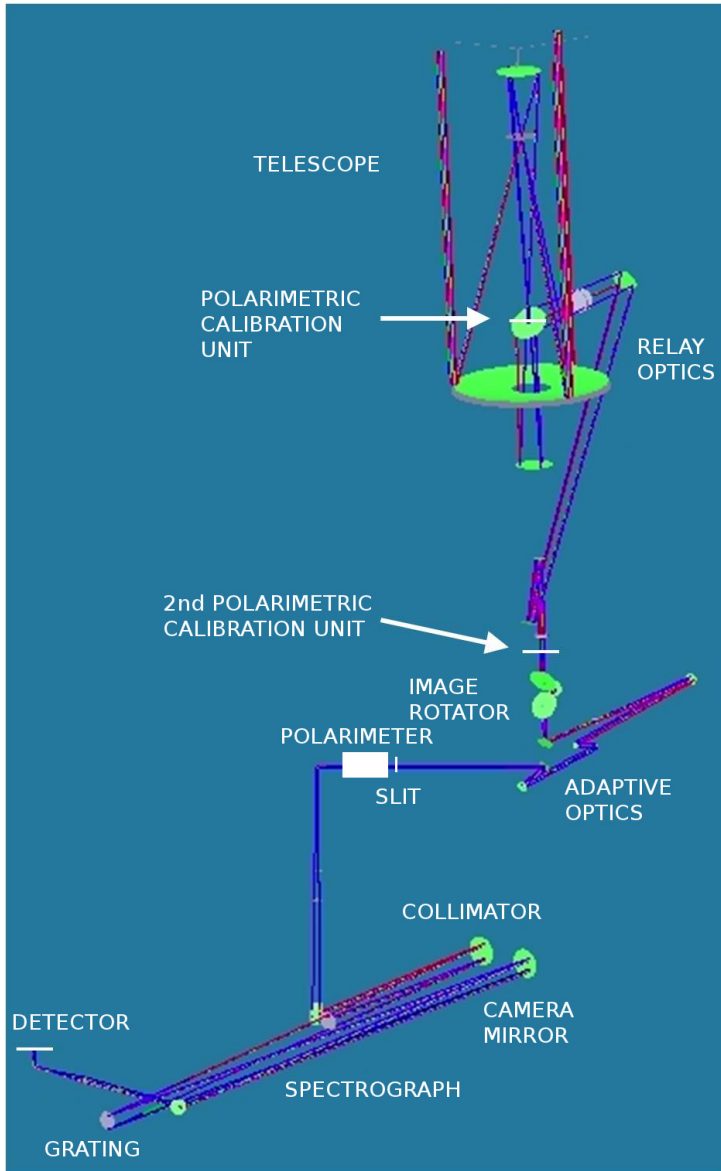


Figure 1.9: Scheme of the full optical path of the GREGOR telescope and GRIS (Fig. 1 in Collados *et al.*, 2012).

VTT under the name Tenerife Infrared Polarimeter II (TIP-II, Collados *et al.*, 2007). The detector is a Rockwell TCM-8600 and has 1024×1020 pixels. It was purchased by the 6. Max-Planck-Institut für Sonnensystemforschung (MPS). The detector has a pixel size of $18 \mu\text{m} \times 18 \mu\text{m}$, and its highest frame rate to acquire images is 30 Hz (Collados *et al.*, 2007).

The spectrograph together with TIP-II is sensitive to the spectral range $1.0\text{--}2.3 \mu\text{m}$ in spectroscopic mode and in the range between $1.0\text{--}1.8 \mu\text{m}$ using the spectropolarimetric mode. Within the wavelength range covered by GRIS there are two spectral region commonly used by observers. The first one is the $1.083 \mu\text{m}$ spectral region. It comprises the photospheric Si I $1.0827 \mu\text{m}$ line, the chromospheric He I $1.0830 \mu\text{m}$ triplet, the photospheric Ca I 1.0834 and $1.0839 \mu\text{m}$ lines, and several telluric lines. The second one lies around $1.565 \mu\text{m}$ and comprises the Fe I $1.5648 \mu\text{m}$ line ($g = 3$), the Fe I $1.5652 \mu\text{m}$ line, the Fe I $1.5662 \mu\text{m}$ triplet and the Fe I $1.5665 \mu\text{m}$. There are more spectral windows which are less often observed. For instance, the Ti I spectral region at $2.230 \mu\text{m}$. The angular resolution of GRIS is $0.18''$ and $0.26''$ for the $1.083 \mu\text{m}$ and $1.565 \mu\text{m}$ spectral ranges, respectively (Collados *et al.*, 2012).

Figure 1.8 shows the full optical path of GREGOR from the primary mirror, through all optical elements, until the infrared detector attached to the spectrograph. The entrance slit is the first optical element of GRIS that the light encounters. It is located on the fifth floor of the building. As described in the Chap. 1.3.1, there are two pentaprisms in front of the GFPI box and the GRIS entrance slit. The first pentaprism reflects the light to the wavefront sensor with a wavelength centered at around of 500 nm and the second pentaprism sends the light to the

GFPI with a wavelength below 660 nm (Puschmann *et al.*, 2012; Collados *et al.*, 2012).

The slit has a length of 50 mm, which correspond to $180''$ on the Sun. However, the FOV of the camera limits this length to $130''$. The width of the slit is $70\ \mu\text{m}$, which correspond to $0.25''$ on the Sun. The light that does not pass through the slit is reflected to a slit-jaw imaging system with three channels, but only two are currently used: continuum (wavelength above 660 nm) and a chromospheric channel (where the $\text{H}\alpha$ filter is not yet installed).

The polarimeter is placed just after the slit. It consists of a polarizing beamsplitter and two ferroelectric liquid crystals. Afterwards, the light is sent to the fourth floor with a 45-degree folding mirror. Once the light arrives there, two flat mirrors send the light to the collimator. The camera mirror and another folding mirror send the light to the focal plane of the spectrograph. Lastly, the light enters a collimating doublet lens and camera doublet lens. These adjust the final focal plane and provide the correct image scale for the detector ($0.13''\ \text{pixel}^{-1}$). As described in Chap. 1.2.2 the GREGOR telescope is equipped with a GPU. A second polarimetric calibration unit is placed at the exit of the relay optics of the GREGOR telescope (see Fig. 1.9). Thus, instrumental polarization introduced by the moving telescope can be calibrated separately from the stationary AO system and instruments. The GFPI and GRIS were used simultaneously to study the evolution of an EFR containing two pores, which is described in the Chap. 4.

Chapter 2

High-resolution imaging spectroscopy of two micro-pores and an arch filament system in a small emerging flux region

Solar activity is intimately linked to the presence of magnetic fields on the solar surface. Small-scale magnetic fields emerge within the interior of supergranular cells, and they are transported by a radial flow pattern to the boundaries of the cells (Martin, 1988). The stronger magnetic fields appear in a multi-stage process eventually leading to pores, sunspots, and (complex) active regions (Zwaan, 1985; Rezaei, Bello González, and Schlichenmaier, 2012). The first indications of newly emerging flux are ephemeral regions with dimensions of about 30 Mm and a total magnetic flux of up to 10^{20} Mx. These small-scale, bipolar magnetic flux concentrations spring up everywhere on the solar surface to continuously replenish the quiet-Sun magnetic field about every 14 hours (Hagenaar, 2001; Guglielmino *et al.*, 2012). Emerging Ω -loops at granular scale were reported by Martínez González *et al.* (2010). When such loops rise through the photosphere their mean velocity can reach up to 3 km s^{-1} . Once the loops reach the upper photosphere, their magnetic field is almost vertical at the footpoints. In the chromosphere, the mean upflow velocity climbs to 12 km s^{-1} , and the energy contained in the loops system is at least $1.4 \times 10^6 - 2.2 \times 10^7 \text{ erg cm}^{-2} \text{ s}^{-1}$ in the lower chromosphere (Martínez González *et al.*, 2010). The emerging fields are transported by supergranular flows migrating towards the network (Orozco Suárez, Katsukawa, and Bellot Rubio, 2012).

The initial expansion rate of the bipoles is about 2 km s^{-1} (Harvey and Martin, 1973). Once the magnetic field becomes sufficiently strong, i.e., the filling factor becomes sufficiently high, ‘micro-pores’ appear as photospheric signatures of flux emergence (Scharmer *et al.*, 2002; Rouppe van der Voort *et al.*, 2005). They change their appearance between elongated features, which are darker in the center and have their maximum brightness at the edges (ribbons), and more circular magnetic structures (flowers), adapting the nomenclature of Rouppe van der Voort *et al.* (2005). The definitions were made based on G-band data. Micro-pores are at the very low end of the statistical size distribution of pores (Verma and Denker, 2014). Once pores are present, sunspots are eventually formed by coalescence of newly emerged flux (Schlichenmaier *et al.*, 2010; Rezaei, Bello González, and Schlichenmaier, 2012).

The dynamics of EFRs are characterized by a transient state (Zwaan, 1985) of magnetic field lines rising within granular convection. On time scales of about 10 minutes (photospheric crossing time), emerging field lines form a pattern of aligned dark intergranular lanes (Strous *et al.*, 1996). When reaching chromospheric heights, the magnetic loops become visible in $H\alpha$, and material gradually drains from the loops. This and convective collapse (Cheung *et al.*, 2008) at the footpoints of the loops lead to strong downflows.

AFS connecting the two opposite magnetic polarities of newly emerging flux are prominently visible in line-core filtergrams of the strong chromospheric absorption line $H\alpha$ and also, but less pronounced, in the Ca II H & K lines (Bruzek, 1969). Downflows in the range of $30 - 50 \text{ km s}^{-1}$ occur near both footpoints of dark filaments, whereas loop tops rise with about $1.5 - 20 \text{ km s}^{-1}$

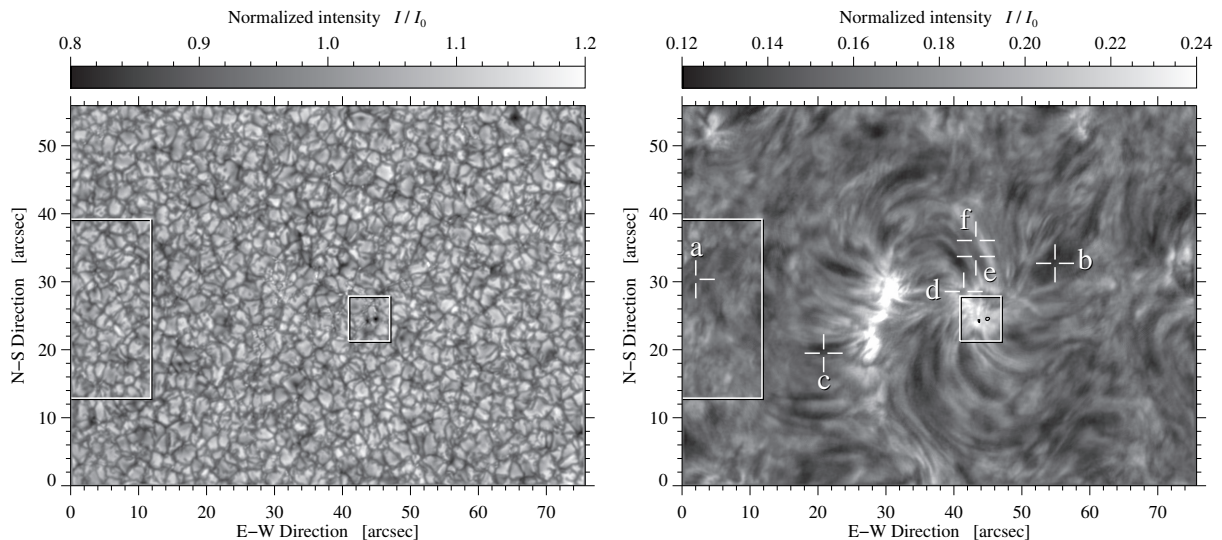


Figure 2.1: MOMFBD-restored broad-band image (*left*) at about $\lambda 600$ nm of micro-pores (white square in the center in both images) in an EFR observed with the Göttingen FPI at 08:07 UT on 2008 August 7. $H\alpha$ line-core intensity image (*right*) corresponding to the broad-band image. The white rectangle on the left outlines the region used for computing the average $H\alpha$ quiet-Sun spectral profile. Crosses ‘+’ and alphabetic labels mark the locations of six contrast profiles plotted in Fig. 2.5. The black contours indicate the position of the micro-pores.

(Bruzek, 1969; Zwaan, 1985; Chou and Zirin, 1988; Lites, Skumanich, and Martinez Pillet, 1998). The arched filaments are typically confined below 10 Mm. Bruzek (1969) relates the length of the filaments (20–30 Mm) to the size of supergranular network cells. The height of the arches is typically 5–15 Mm, and the width of individual filaments is just a few megameters with a lifetime of about 30 minutes (Bruzek, 1967). However, individual loops of the AFS can reach heights of up to 25 Mm and a mean length of about 20–40 Mm (Tsiropoula *et al.*, 1992). In general, the appearance of an AFS remains the same for several hours, whereas significant changes occur only along with the growth of the sunspot group, i.e., after about three days the AFS vanishes.

AFS are mainly observed in $H\alpha$, and one method to analyze $H\alpha$ spectra is cloud modeling. The cloud model (CM) assumes that absorbing chromospheric plasma is suspended by the magnetic field above the photosphere (Beckers, 1964). A broad spectrum of solar fine structure was investigated using CM inversions, e.g., $H\alpha$ upflow events (Lee, Chae, and Wang, 2000), dark mottles in the chromospheric network (Lee, Chae, and Wang, 2000; Al *et al.*, 2004; Contarino *et al.*, 2009; Bostanci, 2011), superpenumbral fibrils (Alissandrakis, Tsiropoula, and Mein, 1990), AFSs (Alissandrakis, Tsiropoula, and Mein, 1990; Contarino *et al.*, 2009), and filaments (Schmieder, Raadu, and Wiik, 1991). Such inversions are attractive mainly because of the inherent simplicity of the model and the scarcity of other well established inversion schemes for strong chromospheric absorption lines such as $H\alpha$ (cf., Molowny-Horas *et al.*, 1999; Tziotziou *et al.*, 2001). However, refinements of CM inversions have been implemented including the differential cloud model (Mein and Mein, 1988), the addition of a variable source function and velocity gradients (Mein *et al.*, 1996; Heinzel, Mein, and Mein, 1999), the embedded cloud model (Chae, 2014), and the two-cloud model (Hong *et al.*, 2014). Bostanci and Erdogan (2010) examined the impact of observed and theoretical quiet-Sun background profiles on CM inversions and concluded that synthetic $H\alpha$ profiles based on non-local thermodynamic equilibrium (NLTE) calculations perform better than profiles derived directly from the data.

Physical processes including radiation, convection, conduction, and magnetic field generation/decay play an important and prominent role in the solar atmosphere. To fully appreciate the dynamics of solar fine structure, simultaneous multi-wavelengths observations at different layers of the Sun are crucial. Wedemeyer-Böhm, Lagg, and Nordlund (2009) critically reviewed the links between the photosphere, chromosphere, and corona of the Sun. They affirm that these atmospheric layers are coupled by the magnetic field at many different spatial scales. Thus loops,

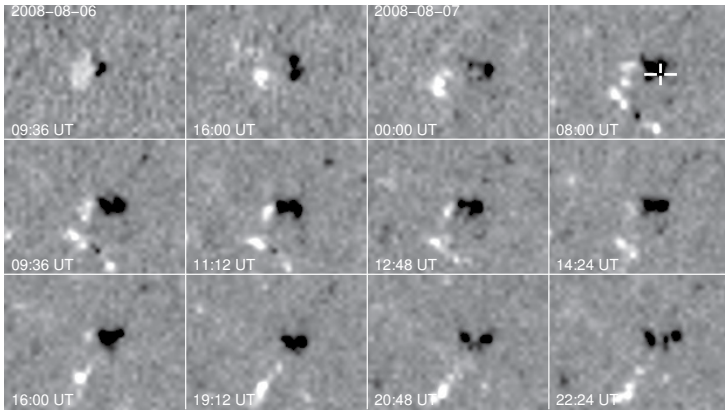


Figure 2.2: SoHO/MDI time-series of a small EFR on 2008 August 6 and 7. Each panel has the same size as the high-resolution image in Fig. 2.1. The magnetograms were scaled between ± 100 G and resampled to a four times finer grid for better display. The cross ‘+’ indicate the position of the micro-pores in Fig. 2.1 using the magnetogram closest in time.

as the ones found in AFS, reach from the photosphere to the chromosphere and corona, where they encounter physical conditions differing by orders of magnitude in temperature and gas density. The present study strives to contribute to the quantitative description of EFRs and AFSs. Some of the key questions related to this study are the following: Do morphological evolution and statistical properties of micro-pores imply a specific flux emergence scenario or flux dispersion mechanism (Chap. 2.3.1)? Which physical quantities are most suitable to restrain theoretical models? Can the results of CM inversions help to identify distinct chromospheric features (cluster analysis in Chap. 2.2)?

In Chap. 2.1, we briefly introduce the observations, image processing, and image restoration techniques. The data analysis is described in Chap. 2.2. Chapter 2.3 puts forward the results, where we first examine the two micro-pores, then determine the photospheric horizontal proper motions associated with the EFR, and finally scrutinize the chromospheric response of emerging flux, which includes Doppler velocities, CM inversions, and parameters characterizing the AFS. We conclude our study by comparing our results with the most recent findings and synoptic literature concerning EFRs and AFSs (Chap. 2.4). Initial results were presented in Denker and Tritschler (2009).

2.1 Observations

A small EFR at heliographic coordinates $E28.5^\circ$ and $S7.91^\circ$ ($\mu = \cos\theta = 0.86$) was observed on 2008 August 7 with the VTT (von der Lühe, 1998) at Observatorio del Teide, Tenerife, Spain. Imaging spectroscopy in the strong chromospheric absorption line $H\alpha$ $\lambda 656.28$ nm was carried out with the Göttingen Fabry-Pérot Interferometer (Göttingen FPI, Puschmann *et al.*, 2006; Bello González and Kneer, 2008). The FOV of the instrument is $77.1'' \times 58.2''$ (688×520 pixels after 2×2 -pixel binning) with an image scale of $0.112'' \text{ pixel}^{-1}$. All data were taken under good seeing conditions (Fried-parameter $r_0 > 15$ cm for most of the time) with real-time image correction provided by KAOS (von der Lühe *et al.*, 2003; Berkefeld *et al.*, 2010).

Four short time-series of simultaneous broad- and narrow-band images were acquired with the Göttingen FPI during the time period from 07:54–08:37 UT (see Fig. 2.1). The observations were paused twice for about six minutes to take flat-field images at solar disk center and continuum images with an artificial light source. The AO system experienced a few interruptions while tracking on solar granulation. From the 54 time-series, 17 data sets (08:07–08:16 UT) have been selected for a more detailed analysis because of very good seeing conditions and continuous AO correction. Post-processing with MOMFBD (Löfdahl, 2002; van Noort, Rouppe van der Voort, and Löfdahl, 2005) as described in Sect. 4.4 of de la Cruz Rodríguez *et al.* (2015) further improves the spatial resolution and contrast of the imaging spectroscopic data.

Each spectral scan of narrow-band images covers 61 equidistant ($\delta\lambda = 3.13$ pm) positions in the strong chromospheric absorption line $H\alpha$ $\lambda 656.28$ nm, i.e., a spectral window of $\Delta\lambda = 0.189$ nm centered on the line core. Eight images were taken at each position to increase the signal-to-noise ratio in preparation for MOMFBD. With an exposure time of 15 ms, the cadence of a spectral scan with $61 \times 8 = 488$ single exposures is $\Delta t = 34$ s. Thus, the total duration of

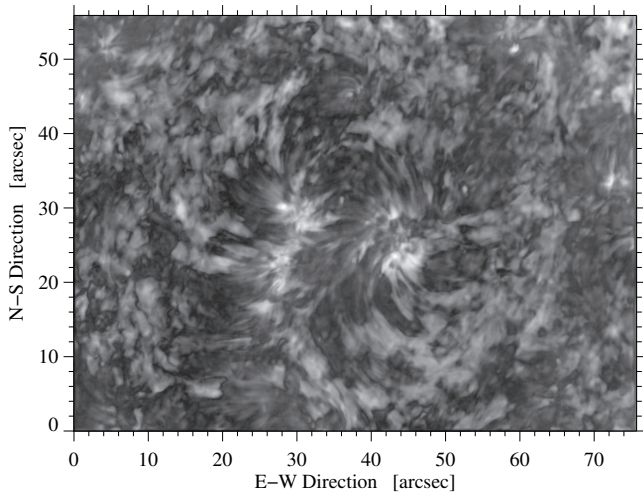


Figure 2.3: Map of the χ^2 goodness-of-fit statistics, where bright regions indicate significant differences between the observed and fitted profiles, in particular near the footpoints of the AFS.

the selected time-series is $\Delta T \approx 10$ min. In some instances, scans of the other time-series are used, e.g., when determining the lifetimes of micro-pores.

Finally, we matched our high-resolution observations to 96-minute cadence, full-disk magnetograms of the Solar and Heliospheric Observatory/Michelson Doppler Imager (SoHO/MDI Scherrer *et al.*, 1995). The magnetograms have 1024×1024 pixels and an image scale of about $2'' \text{ pixel}^{-1}$. Thus, the image scales of the Göttingen FPI and MDI data roughly differ by a factor of twenty, i.e., a magnetogram section of just 39×29 pixels corresponds to the Göttingen FPI FOV. The magnetograms selected for the time-series depicted in Fig. 2.2 were chosen taking into account some data gaps and the noise being present in the magnetograms. The cadence of the first row is about four hours and about 96 minutes in the other two rows.

2.2 Data analysis

2.2.1 Local correlation tracking

Horizontal proper motions are derived from the time-series of 17 broad-band images using local correlation tracking (LCT, November and Simon, 1988) as described in Verma and Denker (2011). However, the data have not been corrected for geometrical foreshortening because of the small FOV and its proximity to disk center. The input parameters selected for LCT are a cadence of $\Delta t = 34$ s, an averaging time of $\Delta T \approx 10$ min, and a Gaussian sampling window with a FWHM = 600 km (the Gaussian used as a high-pass filter has a FWHM = 1200 km). The image scale of the Göttingen FPI broad-band and Hinode/BFI G-band (Kosugi *et al.*, 2007; Tsuneta *et al.*, 2008) images are almost the same, thus facilitating a straightforward comparison of flow fields derived from these two instruments.

2.2.2 Cloud model inversions

Some characteristics of strong chromospheric absorption lines are easier to discover in intensity contrast profiles, which are given as

$$C(\lambda) = \frac{I(\lambda) - I_0(\lambda)}{I_0(\lambda)}, \quad (2.1)$$

where $I(\lambda)$ and $I_0(\lambda)$ denote the observed and the average quiet-Sun spectral profiles, respectively. Beckers (1964) assumes in his model a cloud of absorbing material suspended by the magnetic field above the photosphere, and he provides a relationship between the intensity contrast profile $C(\lambda)$ and four free fit parameters describing the cloud material, i.e., the central

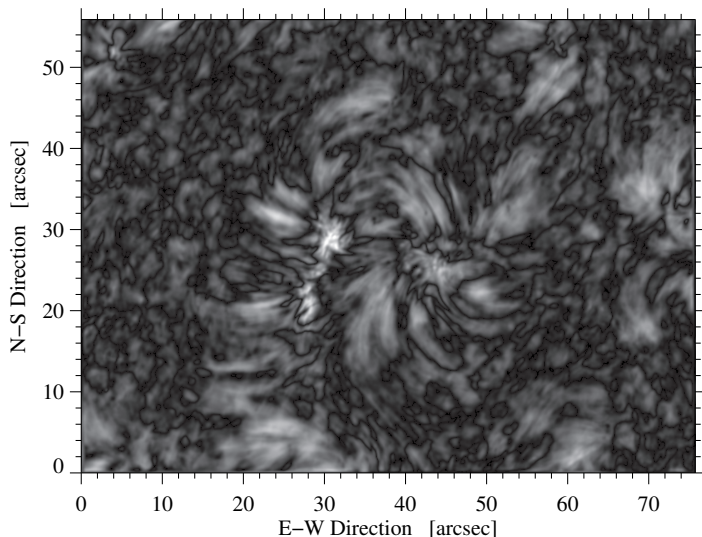


Figure 2.4: Map of the absolute contrast for each spectral profile. The highest (positive) contrasts correspond to the bright regions in the $H\alpha$ line-core intensity image shown in Fig. 2.1.

wavelength of the absorption profile λ_c , the Doppler width of the absorption profile $\Delta\lambda_D$, the optical thickness τ_0 of the cloud at the central wavelength, and the source function S :

$$C(\lambda) = \left[\frac{S}{I_0(\lambda)} - 1 \right] \left(1 - \exp[-\tau(\lambda)] \right) \quad \text{with} \quad (2.2)$$

$$\tau(\lambda) = \tau_0 \exp \left[- \left(\frac{\lambda - \lambda_c}{\Delta\lambda_D} \right)^2 \right] \quad (2.3)$$

The LOS velocity v_{LOS} of the cloud can be derived, once λ_c is known, according to

$$v_{\text{LOS}} = c \frac{\lambda_c - \lambda_0}{\lambda_0}, \quad (2.4)$$

where λ_0 is the central wavelength of the strong chromospheric absorption line averaged over a quiet-Sun area and c is the speed of light.

The quiet-Sun profile $I_0(\lambda)$ is computed within an about $10''$ -wide region to the East of the EFR (see white rectangle in Fig. 2.1). The selection of $I_0(\lambda)$ has a strong impact on the results of the CM analysis (Tziotziou, Tsiropoula, and Mein, 2003), e.g., lateral radiative exchange affects the conditions of the cloud material. The selected quiet-Sun region is at the periphery of AFS, it does not show any features with strong absorption in $H\alpha$, and chromospheric velocities are low. Therefore, this quiet-Sun region is the best choice within the available FOV. We carried out some tests using different samples within this region to create different quiet-Sun profiles. The results from CM inversions were basically identical, which is not the case for other ‘quiet’ settings within the FOV, which contained either absorption features or exhibited high chromospheric velocities. Line shifts are corrected by linear interpolation before averaging the profiles. Assuming that up- and downflows in the quiet Sun are balanced and that the convective blueshift of spectral lines is negligible in the chromosphere, the mean velocity is set to zero and used as a reference for the entire FOV. In this study, the quiet-Sun profile $I_0(\lambda)$ is computed from the data itself. However, Bostanci (2011) demonstrated that theoretical profiles from NLTE calculations may compare favorably to profiles derived directly from observations.

Two steps are required in the CM inversions to efficiently analyze the millions of spectral profiles obtained with imaging spectroscopy: (1) Contrast profiles are computed for 50 000 random CM input parameters, which are restricted to the intervals $\tau_0 \in [0, 3]$, $v_{\text{LOS}} \in [-90, +90] \text{ km s}^{-1}$, $\Delta\lambda_D \in [0, 70] \text{ pm}$, and $S \in [0, 0.4]$, where the source function S is given in quiet-Sun intensity units. In addition, the histograms of the parameters have to closely match those of the observations. This requires some a priori knowledge acquired by dropping the last assumption for a representative sample of contrast profiles. Each observed profile is then compared against the 50 000 templates, and the CM parameters of the closest match (smallest χ^2 -values) are saved.

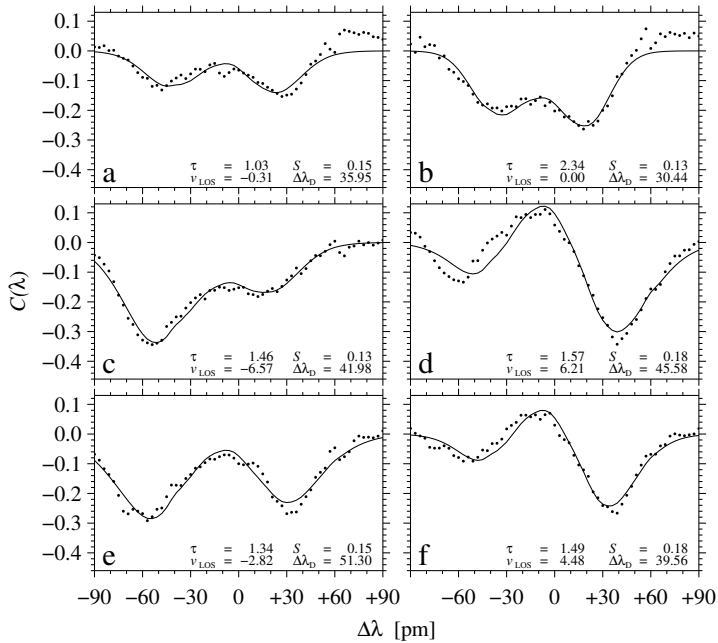


Figure 2.5: Observed contrast profiles $C(\lambda)$ (dotted) and results of CM inversions $C'(\lambda)$ (solid). The CM parameters (omitting the commonly used units) of the inversions are given in the lower right corner of each panel. The alphabetical labels correspond to the locations marked in Fig. 2.1.

(2) The saved CM parameters are the initial estimates to perform a Levenberg-Markwardt least-squares minimization (Moré, 1977; Moré and Wright, 1993) using the MPFIT software package (Markwardt, 2009). The quiet-Sun spectral profile is handed to the fitting routine as private data avoiding common block variables, and MPFIT’s diagnostic capabilities provide the means to easily discriminate between successful fits and situations, where the iterative algorithm does not converge.

Mediocre fits result in high χ^2 -values (Fig. 2.3), which are cospatial with the $H\alpha$ line-core brightenings at the footpoints of the dark filamentary features of the AFS. In addition, for much of the area covered with granulation, the χ^2 goodness-of-fit statistics is low. Good CM inversions correspond in general to regions, where the contrast profiles exhibit enhanced contrast as is evident in Fig. 2.4 for the AFS. Only for regions with high positive contrasts, i.e., the footprint regions, CM inversions fail.

Typical examples of observed $C(\lambda)$ and fitted contrast profiles $C'(\lambda)$ are shown in Fig. 2.5 to illustrate the quality of the CM inversions (positions of the profiles marked in Fig. 2.1). The contrast profiles labeled ‘a’ and ‘b’ have low and high values of the optical thickness τ_0 , respectively. Profile ‘a’ is taken from the quiet-Sun region with an optical thickness $\tau_0 \approx 1.0$, while profile ‘b’ belongs to a prominent dark filamentary feature with $\tau_0 \approx 2.3$. In both cases, the velocity v_{LOS} is close to zero. Contrast profiles ‘c’ and ‘d’ correspond to a dark filamentary feature and a location near the right $H\alpha$ brightening, respectively. They differ mainly in the direction of the velocity v_{LOS} and source function S . The other two CM fit parameters are very similar. The last two examples ‘e’ and ‘f’ are related to counter-streaming in a dark filamentary feature (see Chap. 2.3.3) exhibiting blue- and redshifts, respectively. Counter-streaming is evident in time-lapse movies of $H\alpha$ line-core images. The blueshifted profile is characterized by a very high value of $\Delta\lambda_D = 51.3$ pm and a relatively low value of $\tau_0 = 1.3$.

A fit of an observed $H\alpha$ profile can be derived by solving Eqn. 2.1 for $I(\lambda)$ using the respective fitted contrast profile $C'(\lambda)$ and the quiet-Sun profile $I_0(\lambda)$. The $H\alpha$ profiles corresponding to Fig. 2.5 are shown in Fig. 2.6. Generally, observed and fitted $H\alpha$ profiles are in very good agreement. Only for $H\alpha$ profiles with lower line depths fits and observations significantly deviate, i.e., in regions with high χ^2 -values in Fig. 2.3. This test lends additional credibility to the results of the CM inversions.

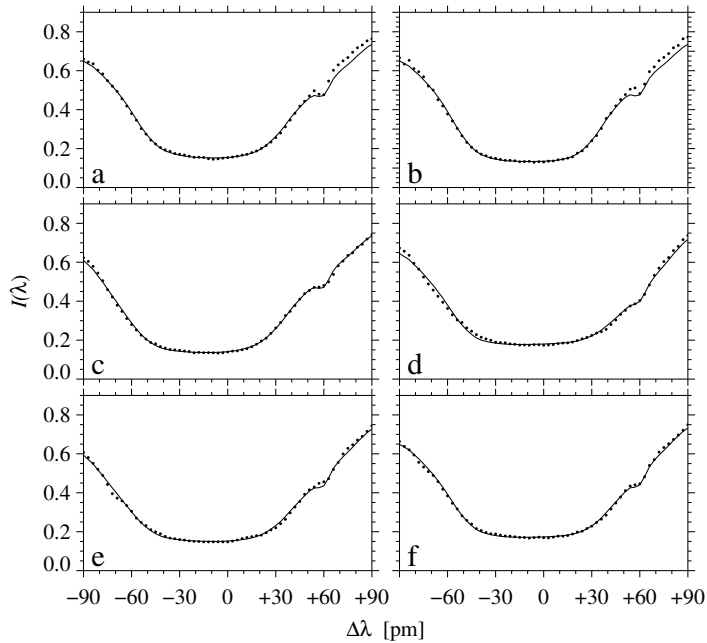


Figure 2.6: Observed normalized H α intensity profiles $I(\lambda)$ (dotted) and converted results of CM inversions $I'(\lambda)$ (solid). The profiles correspond to the contrast profiles $C(\lambda)$ in Fig. 2.5.

2.2.3 Cluster analysis

The four fit parameters of the CM inversion are available for all pixels within the FOV, where the least-squares minimization algorithm converged and where the χ^2 -values are acceptable. However, the presence of different features (arch filaments, bright footpoint regions, quiet Sun, etc.) within the FOV raises the question if these populations can be characterized by distinct CM parameters. Cluster analysis (Everitt *et al.*, 2011) is a powerful tool to identify populations in an n -dimensional parameter space and to locate them in the FOV. These populations might be hidden in histograms of CM parameters (see Chap. 2.3.5), which can only provide hints of their presence due to a particular shape of the distributions. Since $n = 4$ for the CM parameter space, cluster analysis only delivers meaningful results for less than four populations, where two is the most likely number of clusters given the histograms of CM parameters in Chap. 2.3.5). The cluster finding algorithm, a built-in function of the Interactive Data Language (IDL),¹ maximizes the Euclidean distance of the cluster centers while minimizing the intra-cluster distances in the CM parameter space. The algorithm does not deliver the number of clusters. Thus, a priori knowledge is required about the number of clusters.

2.3 Results

The broad-band image in Fig. 2.1 contains two micro-pores (see Rouppe van der Voort *et al.*, 2006) within the quiet Sun, which are indications of a small EFR close to disk center. As seen in MDI magnetograms, a small, compact negative-polarity feature emerges first at 8:00 UT on 2008 August 6 (not shown here). In the next 96-minute magnetogram (see Fig. 2.2), the positive polarity emerges, more extended and with a faint halo-like structure. The positive-polarity patch splits in several kernels while the bipole evolves. The more stable negative-polarity region hosts the two micro-pores. Tracking the EFR was possible until 23:58 UT on 2008 August 7, when a data gap of 14 hours prevented us from reliably identifying the EFR, i.e., only (isolated) small-scale magnetic features were present at the predicted location. Therefore, we conclude that the lifetime of the EFR was at least 40 hours and at maximum 54 hours. Even though the EFR is small, it follows the Hale-Nicholson law (Tlatov, Vasil'eva, and Pevtsov, 2010) and possesses the typical magnetic configuration for the 23rd solar cycle. The dipole emerged around 24 hours before the observations were taken, and the total magnetic flux increased until the beginning of our observations (see Chap. 2.3.1). Although the total magnetic flux in the EFR remained

¹www.harrisgeospatial.com

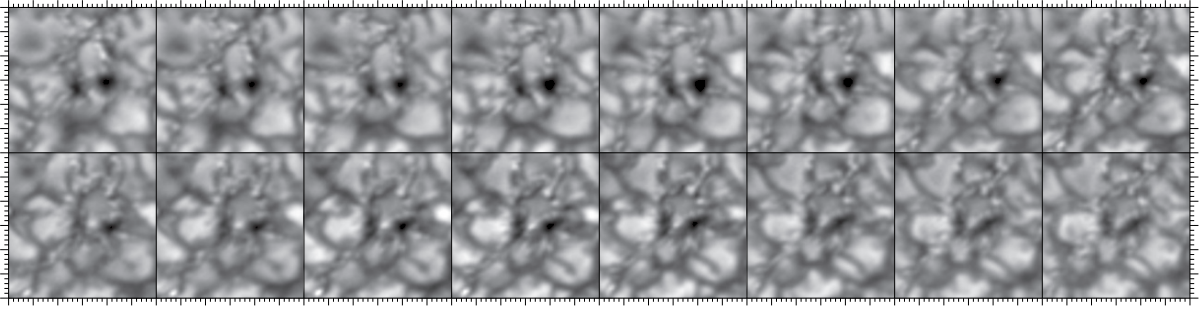


Figure 2.7: Temporal evolution of micro-pores shown at 34-second intervals starting at 08:07 UT (*top-left to bottom-right*). The ROI is $6'' \times 6''$ as indicated by the white square in Fig. 2.1. Major tick marks are separated by one second of arc. All images are from the reconstructed broad-band channel and are displayed in the same intensity range of $0.75 - 1.35 I_0$.

constant for some time after our observations, we use the term EFR throughout the article because of its bipolar structure and the presence of the small AFS.

2.3.1 Temporal evolution of micro-pores

A region-of-interest (ROI) with a size of $6'' \times 6''$ centered on the micro-pores (white square in Fig. 2.1) is chosen to illustrate the temporal evolution of these structures in Fig. 2.7. The time sequence starts at 08:07 UT, the cadence is $\Delta t = 34$ s, and the total duration of the time sequence is about $\Delta T \sim 10$ min.

Initially, two micro-pores are present with diameters of less than $1''$, which evolve with time in intensity, size, and shape. The right micro-pore is circular, whereas the left micro-pore exhibits some star-like extrusions. The intensity of both micro-pores gradually increases, and at the same time the area decreases. Besides the term ‘micro-pore’, [Rouppé van der Voort et al. \(2005\)](#) introduced the nomenclature ‘ribbon’ and ‘flower’ for elongated and more circular magnetic structures, respectively, to capture their morphology at sub-arcsecond scales. The transition from flower to ribbon begins for the left micro-pore early-on in the time-series, whereas the right micro-pore maintains its perceptual structure for about three minutes and then makes the transition from flower to ribbon. Small-scale brightenings and signatures of abnormal granulation ([de Boer and Kneer, 1992](#)) are present everywhere in the vicinity of the micro-pores (e.g., near the coordinates $(30'', 30'')$ and $(29'', 21'')$ in Fig. 2.1).

The 10-minute time-series in Fig. 2.7 displays the two micro-pores under the best seeing conditions. However, the other three time-series also contain moments of good seeing, thus allowing us to study the evolution of the micro-pores more quantitatively over a period of about 40 minutes. Smoothing using anisotropic diffusion ([Perona and Malik, 1990](#)), intensity thresholding ($< 0.9 I_0$), and standard tools for ‘blob analysis’ ([Fanning, 2011](#)) yield the area of the micro-pores, their intensity distribution, and their center coordinates, which in turn provide the distance between the micro-pores. A more detailed description of this procedure is given in [Verma and Denker \(2014\)](#). The temporal evolution of the total area A_{mp} of the micro-pores, their average intensity I_{mp} given in terms of the quiet-Sun intensity I_0 , and the center-to-center distance s_{mp} are presented in Fig. 2.8. Because the micro-pores evolve in a dynamic environment, being constantly jostled around by granules, they change shape and sometimes even seem to merge or split (mediocre seeing also affects the feature identification). Therefore, only data points are included for the distance, where the two micro-pores can be clearly identified. In addition, some restored broad-band images were omitted because of mediocre seeing conditions.

All aforementioned parameters indicate the photometric decay of the system of micro-pores; the total magnetic flux of the EFR, however, remains constant but its distribution within the region changes. At the beginning of the sequence the micro-pores are about 1.1 Mm apart, have a total area of around 0.8 Mm², and their average intensity is just $0.75 I_0$. Linear least-squares fits establish that the two micro-pores approach each other with a speed of $ds_{\text{mp}}/dt = -0.11$ km s⁻¹,

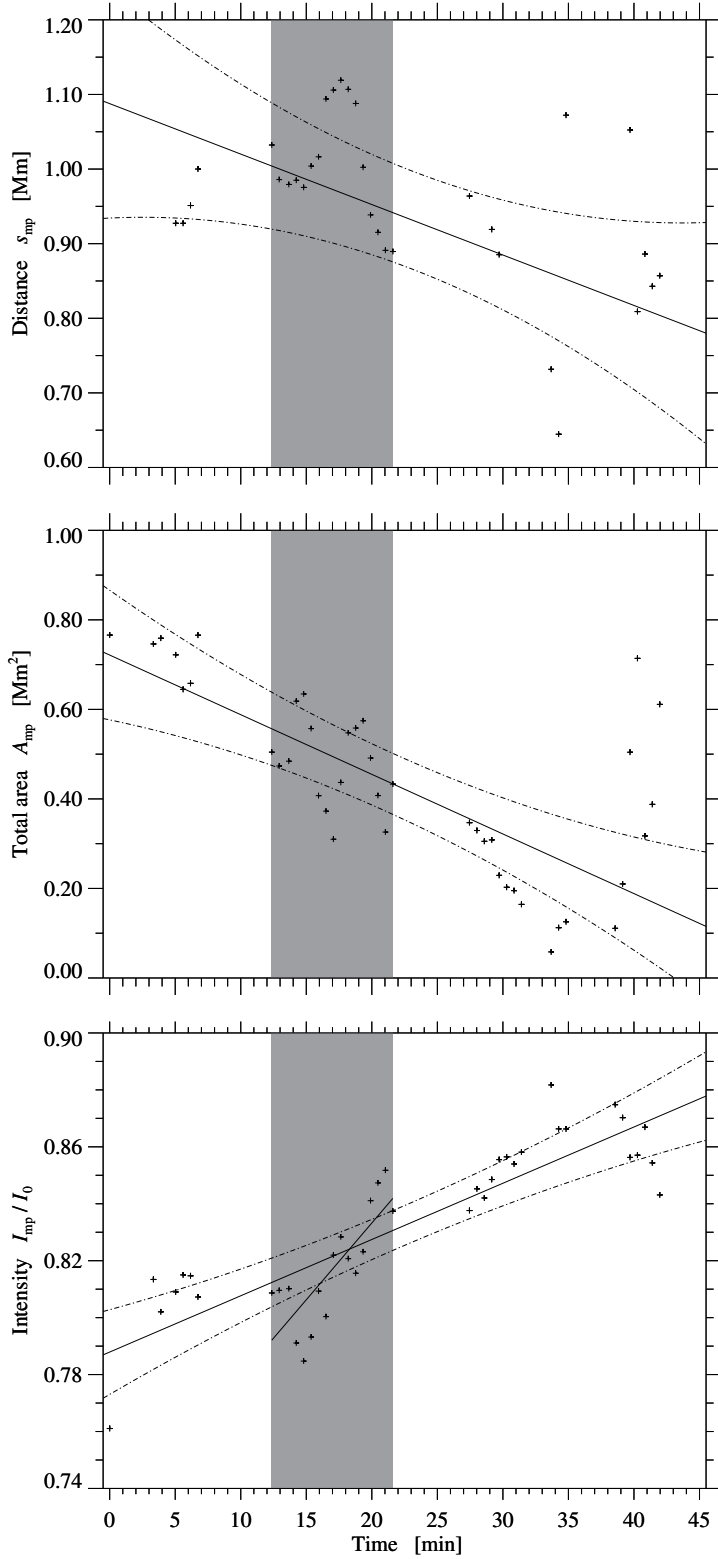


Figure 2.8: Chronological sequence of parameters describing the decay process of the micro-pores starting at 07:54 UT, i.e., center-to-center distance of the micro-pores s_{mp} , total area A_{mp} , and average intensity I_{mp}/I_0 (top to bottom). The gray background indicates the 17 sequences with the best seeing conditions. The solid lines are linear fits to the parameters, and the dash-dotted lines represent the 3σ -error margins.

shrink at a rate of $dA_{\text{mp}}/dt = -0.22 \text{ km}^2 \text{ s}^{-1}$, and approach quiet-Sun intensity levels at $dI_{\text{mp}}/dt = 0.033 I_0 \text{ s}^{-1}$.

Measuring the magnetic flux and thus the growth and decay rates is hampered by the low cadence (96 min), the varying noise level as a function of the heliocentric angle, the geometric foreshortening of the pixel area, the angle of the magnetic field lines (assumed to be perpendicular to the surface) with the LOS, and the small number of pixels having a flux density of more than 20 G. Therefore, we conservatively report only the total unsigned magnetic flux of 2.2×10^{20} Mx (the negative magnetic flux is 1.2×10^{20} Mx) at 08:00 UT on 2008 August 7, which attains a maximum right at the time of the high-resolution Göttingen FPI observations. The flux

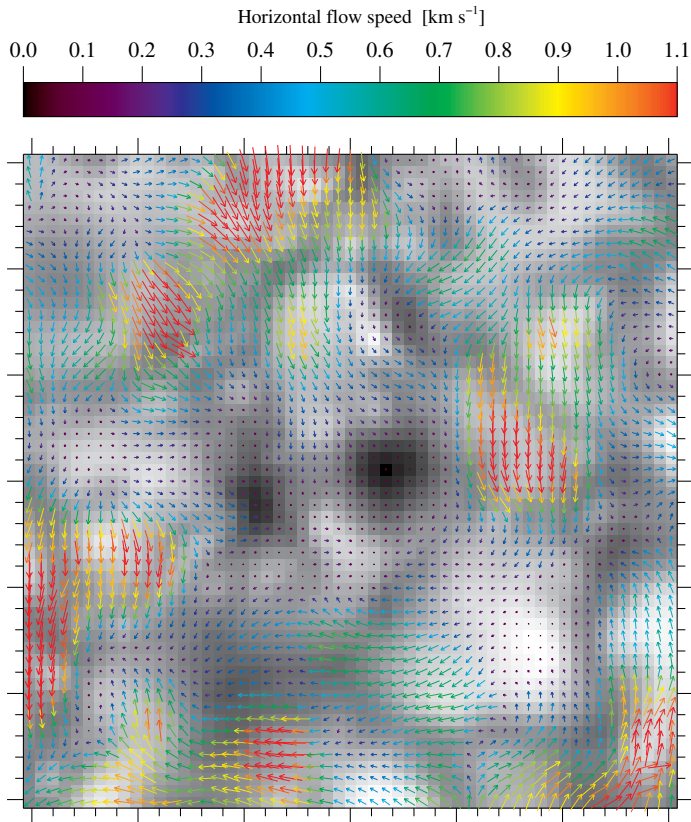


Figure 2.9: Horizontal proper motions in the vicinity of the two micro-pores. Color-coded arrows indicate magnitude and direction of horizontal flows for each pixel of the first broad-band image shown in Fig. 2.7, an enlarged version of which serves as the background. Major tick marks are separated by one second of arc. The FOV $6'' \times 6''$ as indicated by the white square in Fig. 2.1.

contained in the EFR is slightly larger than the upper limit for ephemeral regions (see [van Driel-Gesztelyi and Green, 2015](#)), i.e., much too small to form larger pores or even sunspots. Even though the time resolution is too coarse to provide a growth rate for the magnetic field, our measurements agree with a rapid rise time (already significant changes between the first two magnetograms) and a much slower decay rate (total unsigned flux of 1.3×10^{20} Mx at 22:24 UT on 2008 August 7). However, we cannot use the MDI continuum images to determine the lifetime of the micro-pores because their size is only a small fraction of an MDI pixel.

The 3σ -errors given in Fig. 2.8 demonstrate that a linear model for the decay process of the micro-pores is in general appropriate – at least for the time interval under study. However, there are some deviations, in particular during the time with the best seeing (highlighted gray area in Fig. 2.8), where a more detailed inspection is warranted. The two micro-pores start to separate, while becoming darker. During this period the left micro-pore almost vanishes while the one on the right changes its shape from roundish to more elongated. Towards the end of the sequence shown in Fig. 2.7, the left micro-pore slowly recovers. A linear least-squares fit for just this time period yields an increased intensity gradient of $dI_{\text{mp}}/dt = 0.045 I_0 \text{ s}^{-1}$. The increase in total area towards the end of the sequence is caused by newly forming and merging micro-pores. A slight decrease in intensity accompanies this emergence process, as expected for a small-scale magnetic flux kernel with increasing magnetic flux. Taking the temporal derivatives ds_{mp}/dt , dA_{mp}/dt , and dI_{mp}/dt at face value leads to the conclusion that the decaying micro-pores will vanish before merging.

2.3.2 Horizontal flow field around micro-pores

Magnetic field concentration are known to influences horizontal proper motions. We used LCT ([Verma and Denker, 2011](#)) to investigate if even micro-pores potentially impact the surrounding plasma motions. The mean flow speed is $\bar{v} = 0.59 \pm 0.41 \text{ km s}^{-1}$ across the entire FOV and $\bar{v} = 0.49 \pm 0.31 \text{ km s}^{-1}$ in the ROI shown in Fig. 2.9. In both cases, the standard deviation refers to the variation within the observed field rather than to a formal error estimate. The corresponding 10th percentiles of the speed distributions are $v_{10} = 1.15$ and 0.93 km s^{-1} , respectively. These

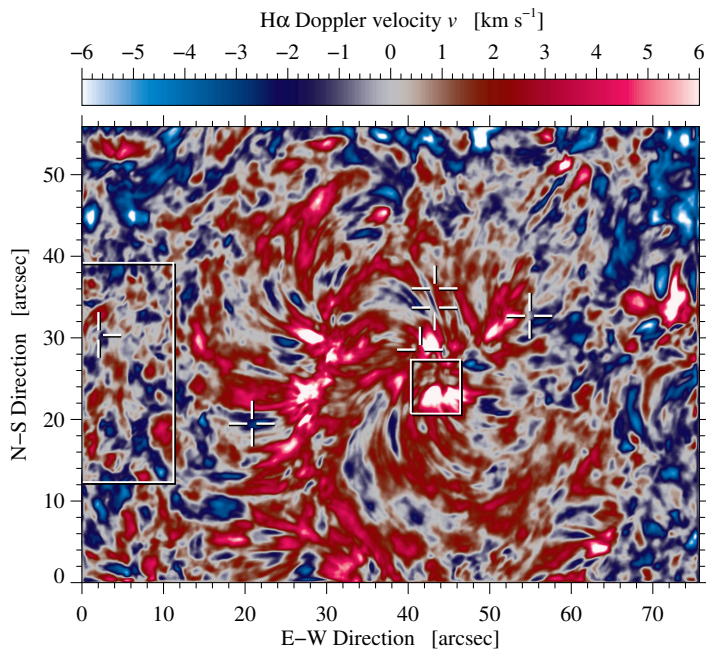


Figure 2.10: Chromospheric Doppler velocity map corresponding to Fig. 2.1 derived with the center-of-gravity method. Blue and red colors represent up- and down-flows, respectively.

values are slightly higher than those provided in Fig. 7 of Verma, Steffen, and Denker (2013). However, considering the shorter averaging time of $\Delta T \approx 10$ min as compared to $\Delta T = 60$ min for Hinode G-band images, the LCT results are in good agreement.

Neither in- nor outflows surround the two micro-pores. The flow field is still dominated by the jostling motion of the solar granulation. As already noted in Verma and Denker (2011), much longer averaging times are needed to clearly detect persistent flows. However, the flow speed is significantly reduced in the immediate surroundings of the micro-pores ($\pm 1''$). Detecting (micro-) pores at spatial scales of one second of arc or below is a formidable task. In their extensive statistical study based on Hinode data, Verma and Denker (2014) consequently required an area of at least 0.8 Mm^2 for pores to be included in the sample, which would exclude the two micro-pores depicted in Fig. 2.9. Therefore, this case study provides additional information for the smallest features that can still be considered a pore.

2.3.3 Chromospheric fine structure and Doppler velocity

Both the $\text{H}\alpha$ line-core intensity (bottom panel in Fig. 2.1) and the $\text{H}\alpha$ Doppler velocity maps (Fig. 2.10) reveal the rich fine structure of the solar chromosphere. The center-of-gravity method (Schmidt, Stix, and Wöhl, 1999) is very efficient and robust in retrieving the $\text{H}\alpha$ Doppler velocities. Repeating the white rectangle and square already drawn in Fig. 2.1 facilitates easy comparison with the photospheric observations – in particular, the rectangle validates the choice of the quiet-Sun region as the Doppler velocity reference, because this region is free of any chromospheric filamentary structure and does not exhibit any peculiar chromospheric flows; and the square illustrates the association of the micro-pores with $\text{H}\alpha$ brightenings and strong downflows in excess of 6 km s^{-1} near the footpoints of small-scale $\text{H}\alpha$ loops belonging to the AFS. However, the Doppler velocities are close to zero at the exact location of the micro-pores.

The AFS consists of two regions with $\text{H}\alpha$ line-core brightenings. Some small-scale loops connect these areas containing the bipolar EFR. Other loops rooted in the bright patches connect to the outside of the EFR. Some bright fibrils are interspersed among the dark filaments. The width of the loops is just a few seconds of arc, and their length is about $6'' - 8''$. Typical aspect ratios for the dark filaments are 1:4 to 1:5. The morphology of the micro-pores, the EFR, and the small AFS closely resembles structures reported in other studies (e.g., Strous *et al.*, 1996; Tziotziou, Tsiropoula, and Mein, 2003; Wedemeyer-Böhm, Lagg, and Nordlund, 2009; Zuccarello *et al.*, 2009). The cross-shaped markers labeled ‘a–f’ identify the locations of some exemplary $\text{H}\alpha$ contrast profiles, e.g., labels ‘c’ and ‘d’ refer to a dark arch filament and a

Table 2.1: Mean value and standard deviation of CM parameters for the quiet Sun, the dark filamentary features, and all fitted contrast profiles.

	quiet Sun	dark filaments	all profiles
S	0.14 ± 0.07	0.12 ± 0.02	0.15 ± 0.05
$\Delta\lambda_D$ [pm]	30.44 ± 10.36	41.62 ± 7.17	33.96 ± 10.74
τ_0	0.44 ± 0.30	1.19 ± 0.45	0.85 ± 0.53
v_{LOS} [km s ⁻¹]	-1.41 ± 10.16	-0.94 ± 3.84	0.41 ± 8.61

Table 2.2: Gaussian and log-normal fit parameters of the normalized histograms of the CM parameters shown in Fig. 2.14.

	μ_1	σ_1	μ_2	σ_2	P_1
S	0.14	0.02	0.18	0.01	0.83
$\Delta\lambda_D$ [pm]	25.92	6.81	42.09	6.35	0.54
τ_0^\dagger	0.17	3.50	1.00	2.60	0.50
v_{LOS} [km s ⁻¹]	0.61	9.77	0.39	3.45	0.76

[†]Two Gaussians are fitted to the normalized histograms of the CM fit parameters with the exception of τ_0 , where the fit consists of a two log-normal distributions.

footpoint, respectively. Properties and parameters derived from CM inversions of the contrast profiles are discussed in Chap. 2.3.5.

H α Doppler velocities v are computed for the dark filaments of the AFS and the bright footpoint areas. Intensity and size thresholds in combination with morphological image processing of the H α line-core intensity maps yield binary masks of bright and dark features. Indexing of pixels belonging to these areas facilitates computing histograms for dark filamentary features ($n = 7009$ pixels) and bright footpoints ($n = 2827$ pixels) shown in the left and right panels of Fig. 2.11, respectively. The histogram of the dark filamentary features is characterized by a median value of $v_{\text{d,med}} = -0.10$ km s⁻¹, a mean value of $\bar{v}_{\text{d}} = -0.13$ km s⁻¹, and a standard deviation of $\sigma_{\text{d}} = 1.31$ km s⁻¹. The corresponding values for the bright footpoints are $v_{\text{b,med}} = 3.77$ km s⁻¹, $\bar{v}_{\text{b}} = 3.97$ km s⁻¹, and $\sigma_{\text{b}} = 1.86$ km s⁻¹.

Both up- and downflows occur in the dark filaments with a small imbalance towards blueshifts. Notwithstanding, the bright footpoint regions almost exclusively harbor downflows with velocities as high as 12 km s⁻¹. Interestingly, blue- and redshifted H α profiles appear in close proximity along the loops (see labels ‘e’ and ‘f’), which can be interpreted as up- and downflows. However, counter-streaming and even rotation along the filament axis are possibilities depending on the specific three-dimensional loop topology. The typical mean upflow velocity at the loop tops is $\bar{v}_{\text{lt}} = -1.13$ km s⁻¹, and extreme values approach $v_{\text{lt,max}} = -3$ km s⁻¹. In general, the ratio of the area between up- and downflowing cloud material is $A_{\text{up}}/A_{\text{down}} = 0.22$.

2.3.4 Cloud model inversions

The rms-deviation between observed and inverted contrast profiles is taken as an additional criterion to select only the best-matched profiles (60% of the entire FOV) as shown in Fig. 2.12, where mediocre fits are excluded and indicated as light gray areas. Rejected regions include much of the quiet Sun and the micro-pores including the surrounding regions with H α line-core brightenings. In all cases, the underlying assumption of CM inversions is not valid, i.e., the premise of cool absorbing plasma suspended by the magnetic field above the photosphere does not apply. Mean values and standard deviations of the CM fit parameters are summarized in Table 2.1 for the quiet-Sun region indicated by the white rectangles in Figs. 2.1 and 2.10, the

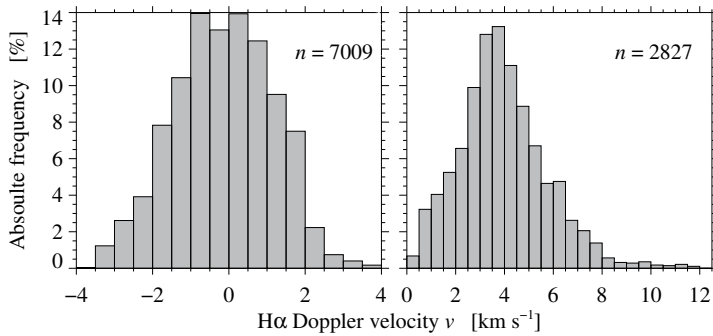


Figure 2.11: Normalized histograms of the chromospheric Doppler velocities v_d for dark filamentary features (*left*) and v_b for bright footpoints (*right*) of the small AFS in Figs. 2.1 and 2.10. The variable n indicates the number of H α line profiles on which the distributions are based.

dark filamentary features, and all fitted profiles. The dark filamentary features represent just 2% of all contrast profiles in the image. In all three case, the source function S is virtually the same, except for the lower standard deviation of the dark filamentary features. The Doppler width $\Delta\lambda_D$ and the optical thickness τ_0 are significantly larger in the dark filamentary features as compared to quiet-Sun regions. The dark features show on average a small upflow similar to the quiet Sun. The quiet-Sun LOS velocity v_{LOS} is not zero like the H α Doppler velocity v , which is likely a selection effect because CM inversions are not available for all pixels of the reference region. The LOS velocity v_{LOS} for the entire FOV is slightly redshifted because of the downflows encountered in the EFR and AFS. The small standard deviation of all CM fit parameters for the dark filamentary features indicates that they belong to a specific class of absorption features.

2.3.5 Properties of the arch filament system

The results of the CM inversions are presented in Fig. 2.12 for the parameters source function S , Doppler width $\Delta\lambda_D$, optical thickness τ_0 , and LOS velocity of the cloud material v_{LOS} , which is not the same as the Doppler velocity v obtained with the center-of-gravity method. The linear correlation coefficient between these two quantities is $\rho(v_{\text{LOS}}, v) = 0.80$. The linear regression model can be written as $v = c_0 + c_1 \cdot v_{\text{LOS}}$ with the constants $c_0 = 0.20 \text{ km s}^{-1}$ and $c_1 = 0.15$. The linear correlation of v_{LOS} and v reduces to $\rho_{lt} = 0.73$ and $\rho_{qs} = 0.64$ for specific features such as loop tops and the quiet Sun.

The parameters S , $\Delta\lambda_D$, and τ_0 reach their largest values in proximity to the H α line-core brightenings. In regions, which are free of any filamentary structure, the values for this set of parameters are much lower. The velocity v_{LOS} within the EFR and the AFS is predominantly directed downwards with the exception of the loop tops of the dark filamentary features, where significant upflows arise, which are clearly in excess of the H α Doppler velocity v (compare with Fig. 2.1).

The temporal evolution of selected CM parameter maps is shown in Fig. 2.13 for the central ROI containing the EFR and AFS as indicated in the top-left panel of Fig. 2.12. The first row corresponds to Fig. 2.12 at 08:07 UT, whereas the other rows display maps at 136-second intervals (every fourth image in Fig. 2.7). The CM inversions and the quiet-Sun selection follow the same procedure as for the first CM map. The backgrounds of source function S and optical thickness τ_0 remain very stable but changes of their extreme values closely track the evolution of the dark arch filaments. The Doppler width $\Delta\lambda_D$ of the arch filaments reaches a maximum in the third map. The velocity v_{LOS} at the loop tops reveals upflows in the first three maps while in the last two maps downflows appear at the same position. This points to the very dynamic nature of AFSs. Despite individual active features, in particular the loop tops, on the whole the AFS is very stable over the 10-minute time-series, which is consistent with the results of Tsiropoula *et al.* (1992).

Normalized histograms for all CM parameters are given in Fig. 2.14. The distributions for source function S and optical thickness τ_0 show a conspicuous ‘shoulder’ on the right side, the one for the Doppler width $\Delta\lambda_D$ is double-peaked, and the one for the velocity v_{LOS} possess an extended base. All these characteristics are indicative for a sample with two (or more) distinct

Table 2.3: Results of cluster analysis for the CM parameters depicted in in Figs. 2.14 and 2.12.

2 populations		w_1	w_2	w_3	w_4	$\mu_1 \pm \sigma_1$	$\mu_2 \pm \sigma_2$	$\mu_3 \pm \sigma_3$	$\mu_4 \pm \sigma_4$
S		0.15	0.15			0.13 ± 0.04	0.15 ± 0.04		
$\Delta\lambda_D$	[pm]	16.00	47.00			23.96 ± 4.98	41.54 ± 5.57		
τ_0		0.31	0.33			0.66 ± 0.45	1.02 ± 0.52		
v_{LOS}	[km s ⁻¹]	-7.03	-6.29			0.67 ± 10.58	0.19 ± 5.84		
Cluster fraction		$c_1 = 43.4\%$	$c_2 = 56.6\%$						
3 populations									
S		0.14	0.15	0.15		0.13 ± 0.05	0.13 ± 0.04	0.15 ± 0.04	
$\Delta\lambda_D$	[pm]	20.18	16.80	47.50		24.99 ± 5.15	25.37 ± 6.19	42.30 ± 6.52	
τ_0		0.36	0.34	0.32		0.56 ± 0.39	0.72 ± 0.48	1.04 ± 0.52	
v_{LOS}	[km s ⁻¹]	-16.04	10.09	-6.14		-11.18 ± 5.34	7.79 ± 5.88	-0.71 ± 4.78	
Cluster fraction		$c_1 = 16.2\%$	$c_2 = 33.0$	$c_3 = 50.8\%$					
4 populations									
S		0.14	0.15	0.15	0.16	0.13 ± 0.05	0.13 ± 0.04	0.16 ± 0.04	0.15 ± 0.03
$\Delta\lambda_D$	[pm]	19.73	16.67	48.55	39.71	23.72 ± 4.98	23.81 ± 5.47	49.43 ± 4.30	37.03 ± 4.91
τ_0		0.32	0.31	0.30	1.18	0.50 ± 0.36	0.67 ± 0.47	1.06 ± 0.55	1.00 ± 0.50
v_{LOS}	[km s ⁻¹]	-16.38	10.20	-5.51	-4.75	-12.33 ± 5.18	8.31 ± 6.10	-0.41 ± 4.72	-0.62 ± 5.48
Cluster fraction		$c_1 = 43.1\%$	$c_2 = 17.2\%$	$c_3 = 27.3\%$	$c_4 = 12.4\%$				

The cluster analysis was performed for $k = 2, 3,$ and 4 populations. The weights w_i refer to the cluster centers. In addition, mean values μ_i along with the standard deviations σ_i were computed for the CM parameters of each cluster. The cluster fractions c_i are given with respect to all good CM fits.

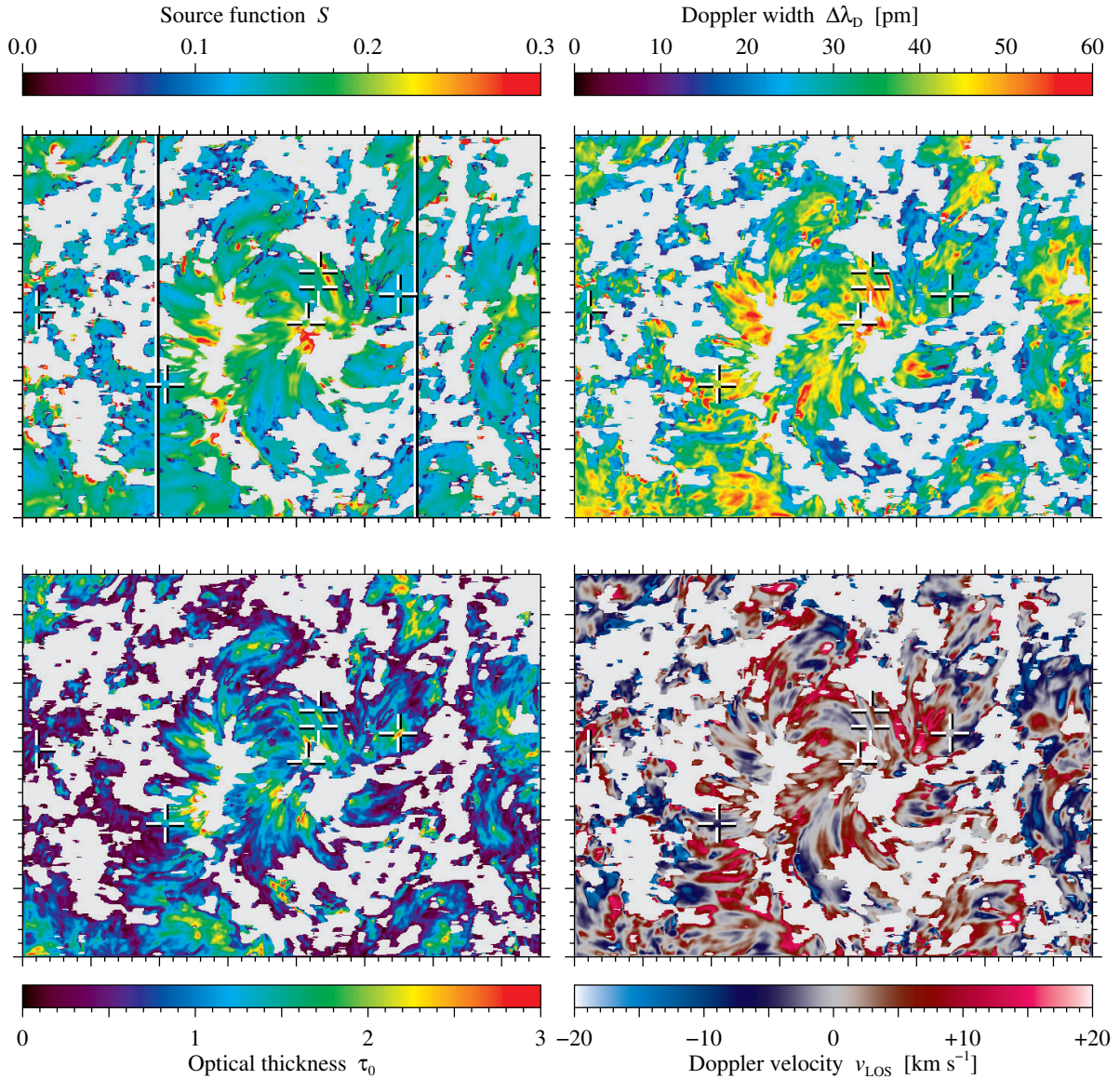


Figure 2.12: Maps of CM parameters for the inverted H α contrast profiles corresponding to Fig. 2.1, i.e., source function S , Doppler width $\Delta\lambda_D$, optical thickness τ_0 , and LOS velocity v_{LOS} (*top-left to bottom-right*). Light gray areas indicate regions, where the CM inversions did not deliver good fits. The two white vertical lines in the upper-left panel enclose the ROI, which was selected to show the evolution of the AFS in Fig. 2.13. The FOV is the same as shown in Fig. 2.1.

populations, e.g., quiet Sun and AFS. In general, the frequency of occurrence is well represented by two Gaussians (S , $\Delta\lambda_D$, and v_{LOS}). Only in case of the optical thickness τ_0 , two log-normal distributions are a more appropriate model. The mean values $\mu_{1,2}$ and standard deviations $\sigma_{1,2}$ of the fit parameters (or the parameter's natural logarithm for τ_0) are given in Table 2.2 along with the normalized frequency of occurrence P_1 of the dominant population.

The histograms provide indirect evidence that two features with distinct CM parameters are present within the observed FOV. However, they do not offer hints, where these features are located, because the distributions strongly overlap. Cluster analysis offers a variety of statistical tools to identify distinct populations in an n -dimensional parameter space, i.e., in our case the 4-dimensional space of CM parameters (see Figs. 2.14 and 2.12). The number of samples in each histogram is $m = 200\,188$. The k -means clustering algorithm implemented in IDL (Everitt *et al.*, 2011) requires a priori knowledge about the number of clusters k . The histograms favor $k = 2$. However, the cases $k = 3$ and $k = 4$ are also investigated to validate that two distinct

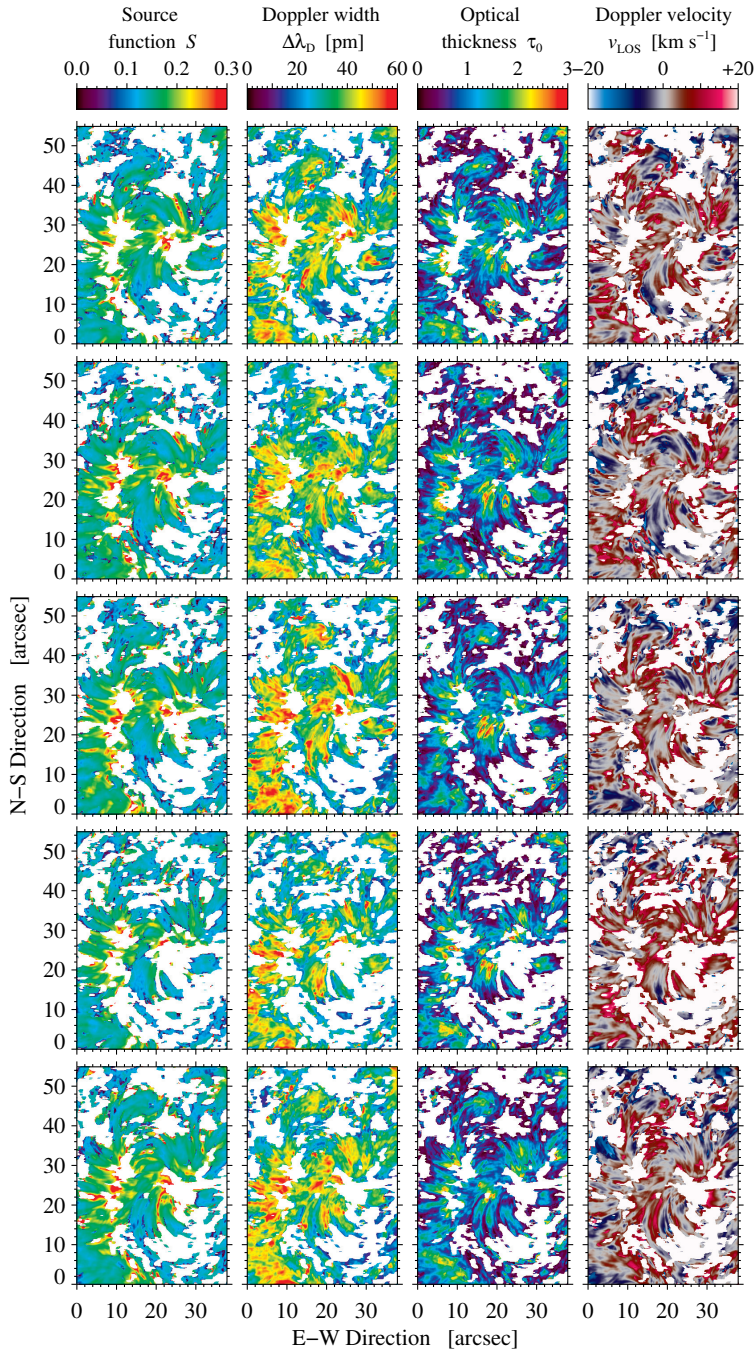


Figure 2.13: Temporal evolution of CM parameters (*top to bottom*) for the ROI containing the EFR and AFS. The maps are depicted at 136-second intervals starting at 08:07 UT (see Fig. 2.12) and show source function S , Doppler width $\Delta\lambda_D$, optical thickness τ_0 , and LOS velocity v_{LOS} (*left to right*). The two white vertical lines in the upper-left panel shown in Fig. 2.12 enclose the FOV of this figure.

populations are indeed sufficient to represent the data. The clustering algorithm assigns the samples to a cluster such that the squared distance from the cluster center is minimized and the distance between the cluster centers is maximized. The clustering algorithm provides additional information to explain the different shapes observed in the histogram of Fig. 2.14, i.e., two peaks for the Doppler width $\Delta\lambda_D$, the halo for the LOS velocity v_{LOS} and the shoulders for the optical thickness τ_0 and the source function S .

Cluster centers or weights w_i are not necessarily the same as the mean values μ_i of the clusters because of the above optimization scheme. In addition to the mean values μ_i , we list in Table 2.3 the respective standard deviations σ_i to illustrate the extend and potential overlap of the clusters. The size of each population is given by the cluster fraction c_i , and the normalized histograms for all the CM parameters are given in Fig. 2.15 for the case $k = 2$.

In the case of just two populations, the Doppler width of the absorption profiles $\Delta\lambda_D$ has the strongest discriminatory power. These broad absorption profiles also have a higher optical thickness τ_0 . On the whole, the mean values and standard deviations of the other CM parameters

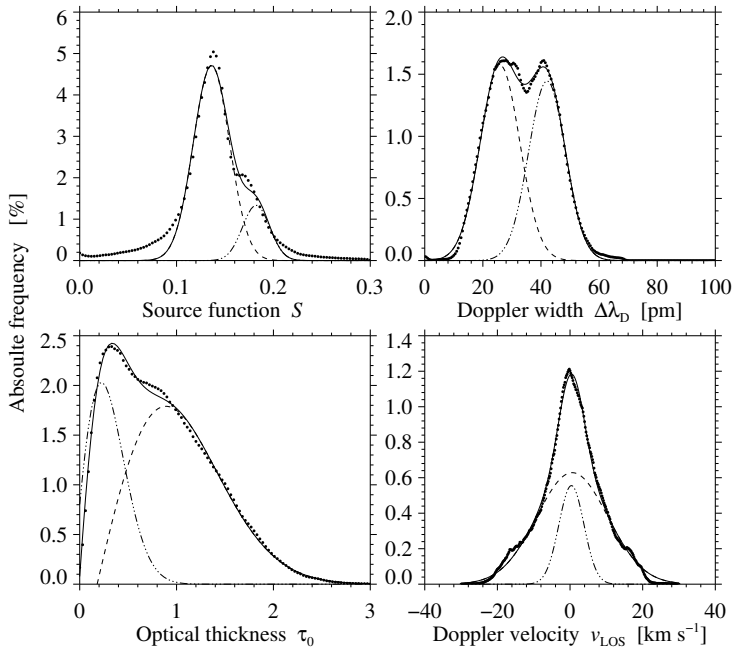


Figure 2.14: Normalized histograms of the CM parameters (dotted) depicted in Fig. 2.12. The dashed and dash-dotted curves are double Gaussian fits with an exception for τ_0 , where two log-normal distributions replace the two Gaussians. The solid curves correspond to the sum of the fitted distributions.

are very similar with the exception of the larger standard deviation σ_1 for the velocity v_{LOS} . This broader distribution is also easily perceived in Fig. 2.15. In general, there is a good agreement between the distributions in Figs. 2.14 and 2.15. Only a secondary peak for the source function S of cluster c_1 and the strong deviation from a log-normal distribution of the optical thickness τ_0 of the cluster c_2 point to the presence of more than two populations. The cluster fractions of $c_1 = 43.3\%$ and $c_2 = 56.6\%$ are very similar, which however might be related to the k -means clustering algorithm’s tendency to produce clusters of similar size.

Increasing the number of clusters to $k = 3$ splits the population according to the velocity v_{LOS} into up- and downflows, while at the same time populations 1 and 2 maintain a similar Doppler width $\Delta\lambda_{\text{D}}$ as before. Increasing the number of clusters to $k = 4$, population 3 for the case $k = 3$ separates into populations 3 and 4 according to the Doppler width, which is still significantly larger than for populations 1 and 2. In summary, increasing successively the number of clusters from $k = 2$ to $k = 4$, first forks population 1 into up- and downflows and then branches population 2 into contrast profiles with narrower and broader Doppler width $\Delta\lambda_{\text{D}}$. However, we conclude that two populations are sufficient to represent the distributions of the CM parameters, which are most easily distinguishable by the Doppler width $\Delta\lambda_{\text{D}}$ and to a lesser extend by the optical thickness τ_0 of the cloud material. More than two populations likely overinterpret the data because they cannot be associated with any particular chromospheric feature.

The locations of the two populations are depicted in Fig. 2.16 in blue and red colors, whereas the gray areas indicate the same regions as in Fig. 2.12 with mediocre CM fits. The background of the figure is the $\text{H}\alpha$ line-core intensity image presented in Fig. 2.1 to assist in matching the two populations to chromospheric features. Population 1 (blue) marks the transition to the quiet Sun, where the cloud material turns more transparent, i.e., $\Delta\lambda_{\text{D}}$ and τ_0 become increasingly smaller. Population 2 (red) is thus more representative for the small AFS, and the corresponding CM parameters in Tables 2.2 and 2.3 should be used in comparisons to values provided in literature. To ensure that these two populations are not some artifacts of the CM inversions, we examine their χ^2 -statistics. The mean values along with their standard deviations are $\chi_1^2 = 0.064 \pm 0.040$ and $\chi_2^2 = 0.048 \pm 0.033$, which are essentially the same.

2.4 Discussion

In this study, we analyze a short period in the evolution of the photospheric and chromospheric signatures belonging to a small EFR containing two micro-pores and a small AFS, where sig-

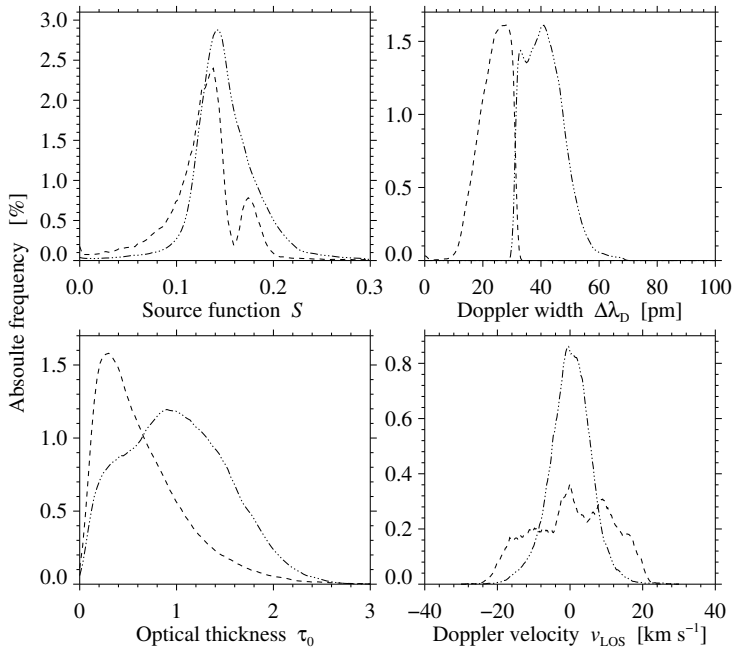


Figure 2.15: Normalized histograms of the CM parameters based on cluster analysis with the same data as in Fig. 2.12. The dashed and dash-dotted curves refer to the two clusters c_1 and c_2 , respectively.

nificant changes take place in just a few tens of minutes. These micro-pores with sizes of less than one second of arc, as seen at photospheric level, are evolving with time in intensity, shape, and size. Their average intensity increased and concurrently the total area decreased, which we interpret as a signature of a local decaying process. Fade-out and disintegration of strong magnetic elements is also supported by the presence of small-scale continuum brightenings and transient signatures of abnormal granulation (de Boer and Kneer, 1992) in the vicinity of the micro-pores. The shape of the micro-pores evolves as first reported by Ruppe van der Voort *et al.* (2005), i.e., alternating between ribbons and flowers. These authors ascribe the dynamics of micro-pores to a fluid-like behavior of magnetic flux, which they relate to magnetic features evident in magneto-hydrodynamic simulations (e.g., Carlsson *et al.*, 2004; Vögler *et al.*, 2005), see also Beeck *et al.* (2015) for more recent simulation results. At very high spatial and temporal resolution, the present study confirms the overall picture of the evolution of magnetic concentrations as presented by Schrijver *et al.* (1997), among others, in which (micro-)pores can split, merge, or vanish.

The temporal derivatives of the mean total area ($dA_{\text{mp}}/dt = -0.22 \text{ km}^2 \text{ s}^{-1}$) and the average intensity ($dI_{\text{mp}}/dt = 0.033 I_0 \text{ s}^{-1}$) can be boundary conditions of magneto-hydrodynamic simulations on flux emergence in general and particularly in solar pore formation (e.g., Cameron *et al.*, 2007; Stein *et al.*, 2011; Stein and Nordlund, 2012a; Rempel and Cheung, 2014). Even if the statistical values in the present study only represent the evolution of one set of micro-pores, the initial mean intensity $0.75 I_0$ and size 0.8 Mm^2 are consistent with other observations and simulations (e.g., Bonet, Sobotka, and Vazquez, 1995; Keppens and Martinez Pillet, 1996; Cameron *et al.*, 2007; Mathew *et al.*, 2007). Small pores are not as dark as larger ones. The brightness increases when pores decay, and they contract and lose flux (Cameron *et al.*, 2007). These authors suggest that increasing lateral radiative heating reduces the pore's size. This effect is compounded by the irregular shape of decaying pores.

The LCT results of horizontal flow field around the micro-pores agree quantitatively with Verma and Denker (2011). However, the short averaging time implies that the flow speeds more closely reflect motions of individual granules, dark micro-pores, and small-scale brightenings. Persistent flows become only apparent with longer averaging times (Verma, Steffen, and Denker, 2013). Yet, the significantly reduced flow speed in the micro-pores clearly indicates that the magnetic field is sufficiently strong to suppress the convective motions in close proximity to the micro-pores and to cancel horizontal motions inside the two $\text{H}\alpha$ line-core brightenings (see Fig. 2.9).

The statistical description of micro-pores is still inadequate and limited to pores with diameters of about 1 Mm, even when resorting to high-resolution Hinode data (Verma and Denker, 2014). In addition, advanced simulations of emerging bipolar pore-like features (e.g., Stein *et al.*, 2011) use larger boxes (about 50 Mm wide) with larger pores (about 10 Mm diameters) and larger separations of the bipoles (about 15 Mm), i.e., they do not necessarily capture the physics and dynamics of micro-pores at sub-arcsecond scales. The observed micro-pores are ‘isolated’ pores, which represent about 10% of the pore population (Verma and Denker, 2014). Isolated pores may have their origin in a solar surface dynamo (Vögler and Schüssler, 2007). Therefore, (micro-)pores in the quiet Sun and in active regions are potentially due to different dynamo actions.

The H α line-core intensity, Doppler velocity maps and MDI magnetograms reveal a chromospheric arch filamentary structure with two regions of H α line-core brightenings and small loops connecting these two areas in a bipolar region with opposite polarities. A similar region was also described in Harvey and Martin (1973). The width of the dark filaments is a few seconds of arc, and their length is around 6''–8'', which is smaller than the mean lengths reported by Tsiropoula *et al.* (1992). We find typical aspect ratios of the loops of 1:4 to 1:5. Overall, but with smaller spatial dimensions, the morphology of the observed AFS agrees with the findings reported in several studies (e.g., Strous *et al.*, 1996; Tziotziou, Tsiropoula, and Mein, 2003; Wedemeyer-Böhm, Lagg, and Nordlund, 2009; Zuccarello *et al.*, 2009).

The H α Doppler velocity v at the bright footpoints is mainly downwards with a flow speed of up to 12 km s $^{-1}$. The up- and downflows in the dark filamentary system possess an imbalance towards blueshifts with typical mean upflow velocities of $\bar{v}_{LT} \approx -1.13$ km s $^{-1}$ at the loop tops, but some upflows reach values close to -3 km s $^{-1}$. Furthermore, the close proximity of some up- and downflows taken together with their appearance in time-lapse movies support the presence of twisting motions along the loop axis. Many other spectroscopic or spectropolarimetry studies have observed AFS in the chromospheric absorption line H α and in the Ca II H & K lines (Bruzek, 1969; Zwaan, 1985; Chou and Zirin, 1988; Lites, Skumanich, and Martinez Pillet, 1998). The range of the downflow Doppler velocities v near the footpoints spans 30–50 km s $^{-1}$, whereas upflows of about 1.5–22 km s $^{-1}$ are observed at the loop tops.

In general, the velocities in the present study are much lower than those reported by the aforementioned authors. This can be attributed to the smaller size of the loop system as compared to previous studies. The higher the velocities, the higher the size of the loop systems. The small and isolated upflow patches in the present study are closer to the Doppler velocities reported in Lites, Skumanich, and Martinez Pillet (1998) with observations near the disk center. They suggest that the observed AFS is not caused by a monolithic flux rope but the result of the dynamical emergence of a filamentary flux bundle. The most accepted flux emergence scenario suggests that the EFRs are formed by magnetic flux tubes that are transported from the base of the solar convection zone (tachocline) to the solar surface by buoyancy (Zwaan, 1987). Normally, these emerging field appears on the solar surface in form of bipolar regions as in our observations known as EFR. The two polarities are commonly the footpoints of an Ω -loops system rising to the solar surface even up to the solar corona (e.g., Strous *et al.*, 1996; Strous and Zwaan, 1999; Schmieder *et al.*, 2004). Furthermore, at chromospheric level, flows occur within the AFS accompanied by draining material from the H α loops towards the footpoints, where the higher downflows reside. In the case of Lites, Skumanich, and Martinez Pillet (1998), this occurs where pores and sunspots form. In our case, only one footpoint shows an intensity signatures, i.e., micro-pores evolving in the photosphere. Another explanations of the physical processes in loops connecting the two footpoints is an upflow that starts in the middle of two regions with opposite magnetic flux, in our case, in the middle and upper part of the two footpoints (magnetic configuration of the case C in Fig. 12 of Lee, Chae, and Wang (2000)). The origin of the upflow events is then explained by magnetic reconnection. The mass moves upward through the small loops and falls down in other areas far away.

We have presented maps of four CM parameters and the corresponding normalized histograms based on CM inversions of H α contrast profiles (Figs. 2.14 and 2.12), i.e., source func-

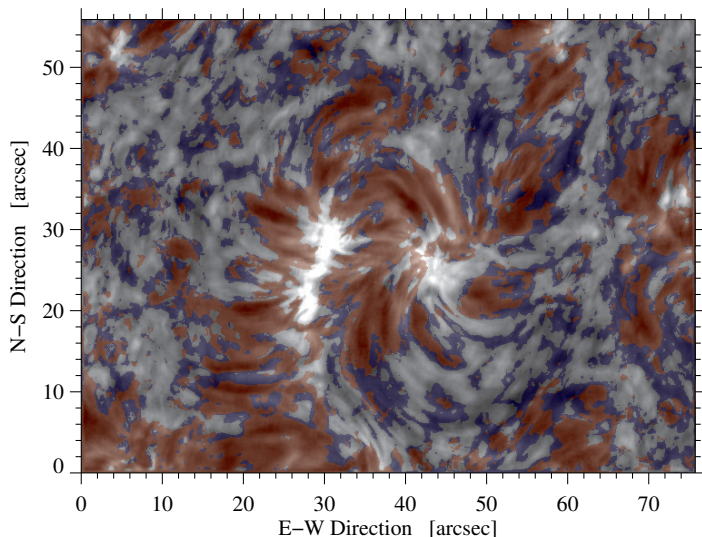


Figure 2.16: Two-dimensional map containing the locations of the two clusters c_1 (blue) and c_2 (red), which were identified in the cluster analysis assuming that the histograms of the CM parameters contain only two distinct populations. The $H\alpha$ line-core intensity image of Fig. 2.1 serves as the background. The gray/transparent areas indicate the same regions as in Fig. 2.12, where the CM inversions result in mediocre fits.

tion S , Doppler width $\Delta\lambda_D$, optical thickness τ_0 , and velocity of the cloud material v_{LOS} . The inversion scheme provided well matched profiles for around 60% of the entire FOV. The population of the inverted AFS contrast profiles covered only about 2% of the entire FOV. Failed CM inversions are mainly related to much of the quiet-Sun regions and the $H\alpha$ line-core brightenings, where the underlying assumptions of the model are violated.

The inversion results for quiet-Sun regions, dark filamentary features, and the ensemble average show in general similar values. However, the Doppler width and the optical thickness of the dark chromospheric filaments are much larger than in the quiet-Sun regions, and the velocity v_{LOS} possesses, similar to the quiet-Sun regions, a small upflow on average. Note that the average quiet-Sun Doppler velocity is based on the center-of-gravity methods not the CM inversions. Furthermore, the velocity v_{LOS} of the entire FOV is on average redshifted because of the downflows being present in the EFR and the AFS, with the exception of the loop tops. In the CM maps it is clearly seen that the parameters S , $\Delta\lambda_D$, and τ_0 reach the largest values in proximity to the $H\alpha$ line-core brightenings. In regions lacking any filamentary structure, the values are much lower. The results of the CM parameters in Table 2.2 are very similar to the ones presented by Bostanci (2011) for dark mottles. They are also close to the results of AFSs investigated by Alissandrakis, Tsiropoula, and Mein (1990), whereas the source function S and optical thickness τ_0 deviate from the results presented by Lee, Chae, and Wang (2000); Bostanci and Erdogan (2010).

The AFS in the present study certainly belongs to the smallest observed chromospheric filaments. Only mini-filaments (Wang *et al.*, 2000) are smaller. Interestingly, the CM inversion results are similar as compared to a giant filament investigated by Kuckein, Verma, and Denker (2016). As expected, their mean optical thickness τ_0 is larger than our average inferred values.

The normalized histograms suggest that the CM parameters represent two different populations, which is corroborated by the cluster analysis and the computed absolute contrast that clearly distinguishes between features with higher contrast belonging to the AFS and those being part of quiet-Sun regions or the interface between the quiet Sun and the AFS. We expect that for similar observations of AFSs two populations appear again all over the solar disk and that we can distinguish between dark AFS, the regions of the quiet-Sun, and the transition to the quiet Sun (note that in several studies the authors just select a region of interest, i.e., the features with high contrast and they do not invert the any other region, (e.g., Contarino *et al.*, 2009; Kuckein, Verma, and Denker, 2016)). For larger FOVs that may contain different features like active regions, filaments, quiet-Sun, rosette structures, etc., we foresee that CM inversions together with cluster analysis will separate these chromospheric features in different populations as well based on the four CM parameters.

2.5 Conclusions

Photospheric and chromospheric structures like sunspots and pores cover a broad range of spatial scales. Sunspots come into existence as pores, grow, and potentially assemble into large (complex) active regions. In the chromosphere, cool plasma is suspended by the magnetic field in structures ranging in size from mini-filaments (a few megameters) to giant and polar crown filaments (several hundred megameters). This raises the questions if scaling laws exist characterizing the physical properties of these phenomena. In EFRs with AFSs both photospheric and chromospheric properties are relevant. Exploring the lower end of their spatial scales requires large-aperture solar telescopes with dedicated instruments. As a consequence the observed FOV is small, time-series cover at most a few hours, and synoptic observations building up a database are often impracticable. Therefore, case studies are the only means of advancing our knowledge about EFRs and AFSs at sub-arcsecond scales.

In the present study, we used the Göttingen FPI to investigate a very small EFR with its accompanying AFS. It is hardly conceivable that even smaller systems exist, which still have a clear bipolar magnetic structure. Mini-filaments are not considered in this context because they reside at the PIL between opposite magnetic polarities (Wang *et al.*, 2000), thus representing a different magnetic field topology. In our observations, the AFS connects the micro-pores to a quiet-Sun region of opposite polarity flux, i.e., the small-scale filaments are perpendicular to the PIL. The filaments or dark fibrils are a clear indication of a newly emerging flux in the form of Ω -loops. The magnetograms represented in Fig. 2.2 show that the trailing polarity is formed earlier than the leading polarity and that it is formed earlier than the leading polarity. However, the leading polarity is more compact and survives longer. This asymmetry is a typical property of EFRs, also for larger ones (van Driel-Gesztelyi and Petrovay, 1990). The decay of the EFR is characterized by flux cancellation and fragmentation. The flux system emerged and then submerged as a whole similar to a larger EFR studied by Verma *et al.* (2016). Flux fragmentation indicate that several Ω -loops and not just one monolithic loop connects the opposite polarities, which is also reflected in the multiple dark fibrils constituting the AFS.

The statistical description of micro-pores and flux emergence at spatial scale below 1 Mm remains challenging. We presented, among others, evolution time-scales for the area of micro-pores, their mean intensity, and the separation of footpoints, which match previous observations and simulations, when taking into account the size of the observed EFR and AFS. In the chromosphere, upflows are mainly observed at the loop tops and from there the cool plasma drains towards the footpoints. Generally, the LOS velocities inferred in the loops are two to four times lower than for larger AFSs. Buoyancy and curvature of the rising/submerging Ω -loops are here the determining factor but a statistically more meaningful sample is clearly needed to derive scaling laws. Pores occur on spatial scales ranging from sub-arcsecond to about ten arcseconds. Thus, comparing observations of EFRs and AFSs in this spatial domain with simulations of flux emergence and decay will be very beneficial for our understanding of the dynamic interaction of magnetic fields with the surrounding plasma.

A shortcoming of the present study was the lack of high-resolution spectropolarimetric observations, which motivates follow-up observations with the GFPI (Puschmann *et al.*, 2012) and GRIS (Collados *et al.*, 2012) at the 1.5-meter GREGOR solar telescope (Schmidt *et al.*, 2012). Both instruments are capable of full-Stokes polarimetry and allow multi-wavelength observations of multiple spectral lines (e.g., $H\alpha$ s with the GFPI and the spectral region around the He I triplet at 1083 nm with GRIS). In addition to magnetic field information, the height dependence of physical properties in EFRs and AFSs becomes thus accessible.

Chapter 3

Fitting peculiar spectral profiles in He I 10830 Å absorption features

The spectral window around the He I 10830 Å triplet has often been used to study the magnetic properties and dynamics in the solar chromosphere. The height of formation of this triplet lies in the upper chromosphere (Avrett, Fontenla, and Loeser, 1994). It comprises three transitions, which take place between the lower 2^3S_1 level and the upper $2^3P_{2,1,0}$ level. However, two transitions are blended and therefore only two spectral lines are observed. Generally, the blended line at ~ 10830.30 Å is called “red” component, while the non-blended line at 10829.09 Å is called the “blue” component. The wavelengths were taken from the National Institute of Standards and Technology (NIST).¹

Of special interest are the strongly redshifted He I profiles, which have been reported by several authors (e.g., Penn and Kuhn, 1995; Muglach, Schmidt, and Knoelker, 1997; Muglach and Sütterlin, 1998). Commonly observed are two atmospheric components located within the same resolution element (Lagg *et al.*, 2007). These “dual flows” were reported for the first time by Schmidt, Muglach, and Knölker (2000) and have an easily recognizable spectral pattern with two or more peaks next to the red component of He I. One of the peaks is often subsonic while the other reaches supersonic velocities. At the average formation temperature of the He I triplet, velocities close to 10 km s^{-1} correspond to the sound speed (Lagg *et al.*, 2007). From now on we will label the profiles, which clearly show dual flow components of the He I triplet as the slow (the one close to rest) and fast (redshifted with respect to the slow one) components.

Several studies reported on dual or multiple-peak He I profiles in different phenomena on the Sun, e.g., Teriaca *et al.* (2003) in two ribbon flares, Sasso *et al.* (2007) and Sasso, Lagg, and Solanki (2011) during a C2.0 flare, Lagg *et al.* (2007) during an emerging flux process in an active region, or Aznar Cuadrado, Solanki, and Lagg (2005, 2007) in active and quiet-Sun regions. All of them reported supersonic velocities of the fast component between 40 and 90 km s^{-1} . Lagg *et al.* (2007) suggested that these dual flows are formed in extremely filamentary structures and that their origin might be related to the magnetic field. It is expected that these profiles provide information on two different heights in the atmosphere.

Several inversion codes are able to synthesize and invert the Stokes profiles of the He I 10830 Å triplet, for example, the He-Line Information Extractor code (HELIX⁺, Lagg *et al.*, 2004, 2009), the HAZEL code (Asensio Ramos, Trujillo Bueno, and Landi Degl’Innocenti, 2008), or the MELANIE code (Socas-Navarro, 2001). These codes infer physical parameters such as the LOS velocity and the vector magnetic field, among others. Usually these inversion codes require considerable computation time. In this paper, we present a simple and very fast technique to infer the LOS velocities for single and double-peaked profiles. Thus, the information present in the polarized Stokes parameters is for the moment disregarded. In particular, we adapted the technique to fit the slow and fast components of the He I 10830 Å triplet.

¹www.nist.gov

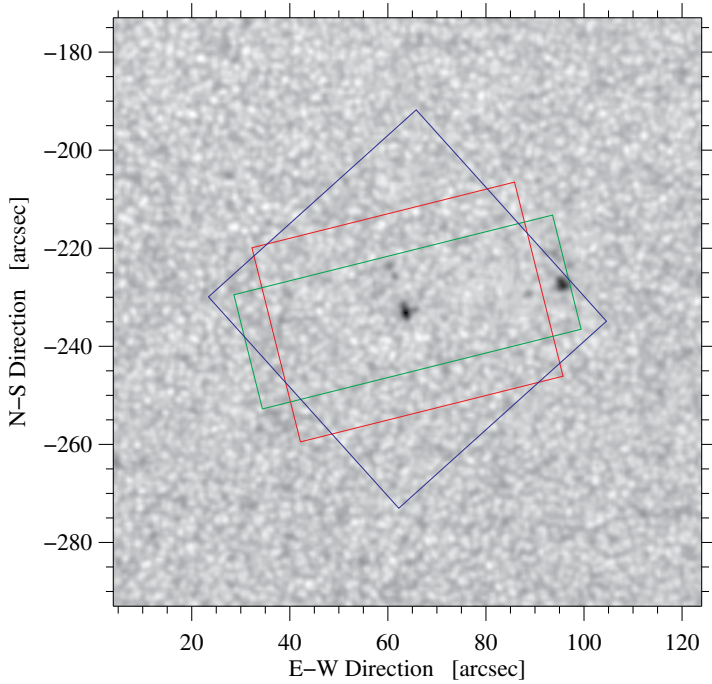


Figure 3.1: Overlap of the FOV of the three instruments: GRIS (green), GFPI (red), and CRISP (blue). The background continuum image is from SDO/HMI taken at 08:47 UT on 2015 April 17.

3.1 Observations

Our two-component fitting code was applied to one data set acquired with the 1.5-meter GREGOR solar telescope (Schmidt *et al.*, 2012; Denker *et al.*, 2012) at Observatorio del Teide, Tenerife, Spain. An EFR located at heliographic coordinates S19 and W4 ($\mu \equiv \cos \theta = 0.97$) was observed on 2015 April 17 between 08:16 UT and 09:18 UT. Several instruments and telescopes were involved in this campaign. We will concentrate on GRIS (Collados *et al.*, 2012).

For the first time the instrument was operated in the very fast spectroscopic mode (no polarimetry) in the He I 10830 Å spectral region. Typically, in polarimetric mode several integrations reduce the noise in the spectra but also prolongate the cadence of the scans. The fast mode relies on a single integration and accepts higher noise in exchange for an improved cadence. The standard deviation $\sigma = 3.3\%$ of the normalized quiet-Sun continuum in the wavelength range 10835.8–10837.1 Å for all spectra in the scan gives an estimate of the noise level, which will slightly increase for darker features like pores.

The spectral window of about 18 Å comprised the photospheric Si I 10827 Å line, the chromospheric He I 10830 Å triplet, the photospheric Ca I 10834 and 10839 Å lines, and several telluric lines among other weaker spectral lines. The spectral sampling was $\delta_\lambda = 18.03 \text{ m}\text{\AA} \text{ pix}^{-1}$, and the number of spectral points was $N_\lambda = 1010$. The slit was by chance in parallel to two small pores belonging to the EFR (see Fig. 3.1). The pixel size along the slit was $\sim 0''.136$, thus covering a length of $66''.3$. For each position of the slit, the integration time was $t = 100 \text{ ms}$ with only one accumulation. This allowed for very fast spectroscopic scans covering an height of $24''.12$ (with 180 steps and a step size of $\sim 0''.134$) in only $\sim 58 \text{ s}$. During roughly one hour of observations (62 min), the GREGOR's altitude-azimuthal mount introduced an image rotation, which had to be corrected (Volkmer *et al.*, 2012). The total rotation angle for the period of observation was 22.3° . However, the image rotation for each map is small (never larger than 0.4°) and therefore negligible.

In total 65 scans were taken covering an area of $66''.3 \times 24''.1$. Nevertheless, only one map (08:42–08:43 UT) with abundant two-component profiles will be presented in this work (see Fig. 3.2). The data were taken under good seeing conditions with real-time corrections provided by GAOS (Berkefeld *et al.*, 2012). Simultaneous multi-wavelength observations were carried out with additional instruments including the GFPI (Denker *et al.*, 2010; Puschmann *et al.*, 2012) at the GREGOR telescope and CRISP (Scharmer *et al.*, 2008) installed at the SST (Scharmer *et al.*,

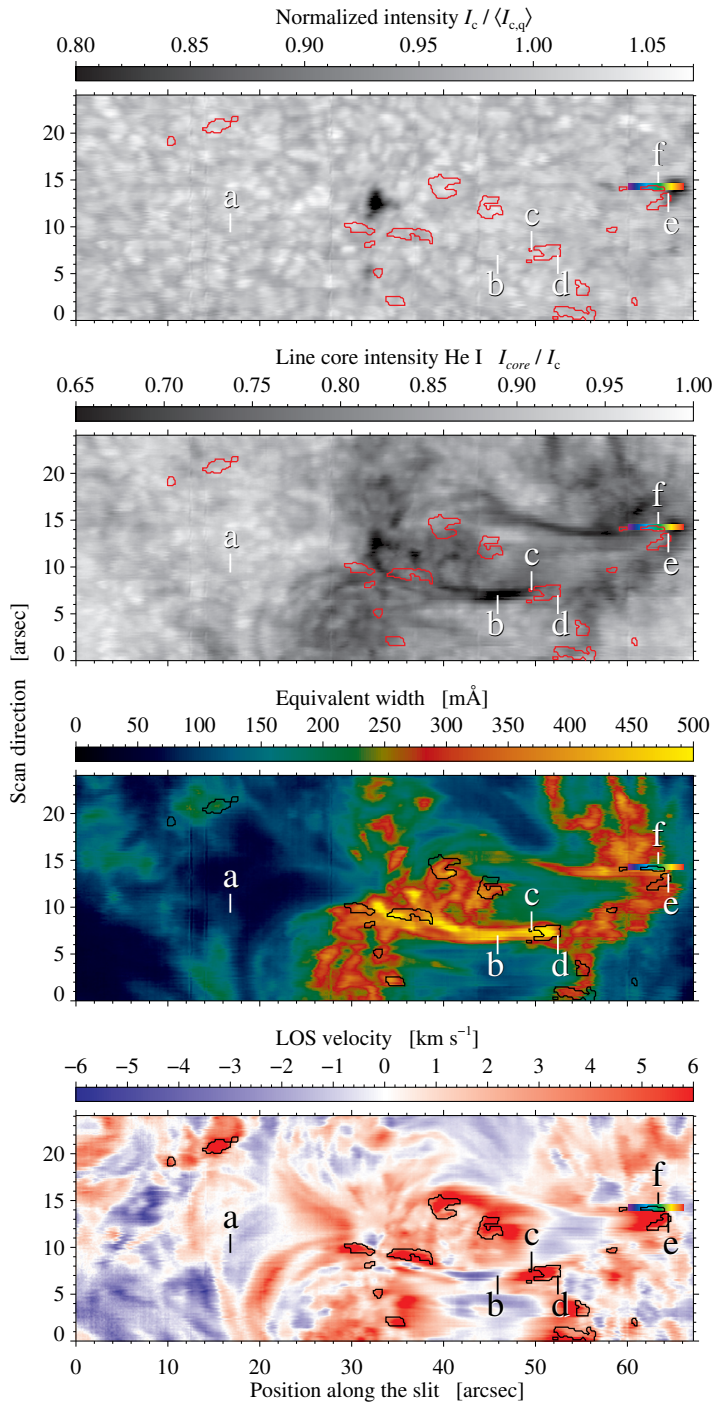


Figure 3.2: GRIS slit-reconstructed images on 2015 April 17 at 08:42 UT of the observed region. From top to bottom: continuum intensity, line core intensity of the red component of the He I triplet, equivalent width, and the one-component LOS velocity. The LOS velocity was inferred using a single Lorentzian fit. The labels “a” to “f” mark the locations of six He I profiles shown in Fig. 3.3. The contours encompass only clearly discernible dual-flow components in He I profiles. The rainbow-colored bar marks in all maps the location of the profiles plotted in Fig. 3.4.

2003) located at Observatorio Roque de los Muchachos, La Palma, Spain. An overview of all the involved FOVs is shown in Fig. 3.1 after alignment with a continuum image of HMI (Scherrer *et al.*, 2012; Schou *et al.*, 2012) on-board the SDO (Pesnell, Thompson, and Chamberlin, 2012). The analysis of the full data set and an investigation of the dynamics related to the EFR are deferred in Chap. 4.

3.2 Data reduction

Dark and flat-field corrections were applied as part of the data reduction. The proper continuum of the GRIS spectra was derived by comparing the average quiet-Sun spectrum $I_{qs}(\lambda)$ with that of a Fourier Transform Spectrometer (FTS, Neckel and Labs, 1984), which was convolved with a Gaussian to take into account the degradation of the observed spectrum by straylight (see Allende Prieto, Asplund, and Fabiani Bendicho, 2004, for a description of the procedure). The

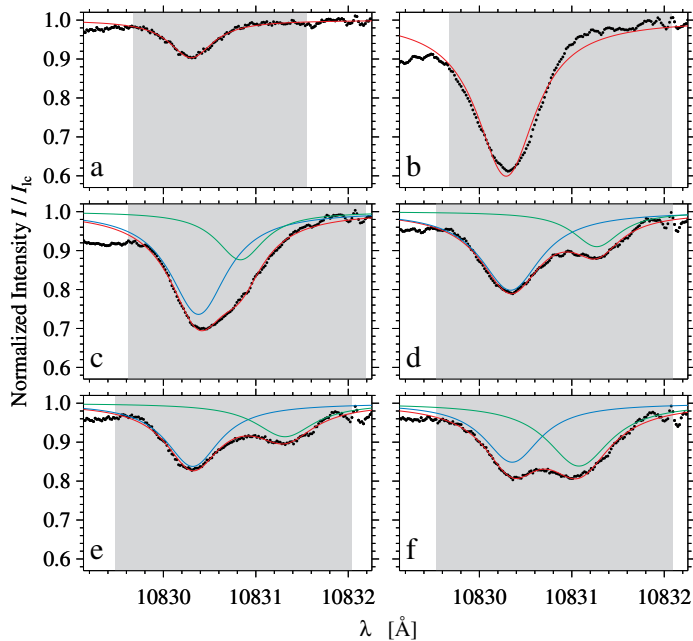


Figure 3.3: The dots represent the observed He I red-component profiles and the best Lorentzian fit is shown with a solid red line. When dual-flow He I profiles are present, the fit (solid red line) is a superposition of two individual Lorentzians (blue and green solid lines). Labels ‘a’ to ‘f’ show the locations of the profiles in the map of Fig. 3.2. The grey background marks the fitting range.

average quiet-Sun profile was computed in an area where the He I absorption was almost absent. Common fringes were removed by multiplying every spectrum by the ratio between the equivalent quiet-Sun mean profile and the quiet-Sun mean profile I'/I_{qs} . Dust particles along the slit and other bright artifacts had to be removed from the data by using an additional flat field based on the science data assuming that the granulation was uniform and isotropic. Abnormal intensity peaks were found along some spectra due to the bad pixels on the detector chip. The peaks were detected by calculating the wavelength derivative of the spectrum of each pixel and searching for absolute values above a suitable threshold. Abnormal intensities were then replaced by an interpolated value between the previous and the next pixels.

The wavelength calibration was carried out using the two telluric lines located next to the He I 10830 Å triplet. An area of the quiet Sun was chosen to compute an average intensity profile. A direct comparison between the separation of the two telluric lines of the averaged intensity profile and the atlas profile of the Fourier Transform Spectrometer (Neckel and Labs, 1984) provided the dispersion ($18.03 \text{ mÅ pixel}^{-1}$). The first telluric line at 10832.108 Å was then used as the wavelength reference. In addition, the wavelength scale was corrected for solar orbital motion and rotation, Earth’s rotation, and the solar gravitational redshift (see appendices A and B in Kuckein, Martínez Pillet, and Centeno 2012b).

The fast component is blended by a telluric line for high LOS velocities. Therefore, the telluric line was removed from our spectra. To accomplish this task we averaged all spectral profiles from the map to compute a mean intensity profile. We assumed that the telluric line has a constant wavelength, i.e., it does not shift along the wavelength axis at any time. The telluric line was fitted in the spectral range of $10831.48\text{--}10832.56 \text{ Å}$ with a single Lorentzian profile. Hence, we have computed a synthetic telluric profile. The telluric line was then removed by dividing each spectrum by the synthetic profile. A smooth transition of the spectrum at the location where the telluric line started was assured by forcing the continuum in the line wings of the telluric line to be $I_c = 1$. Therefore, each spectrum was normalized to the local continuum before removing the telluric line.

Figure 3.2 shows a slit-reconstructed continuum intensity map in the top panel and a line-core intensity map of the red He I component in the panel below (using the minimum of the line for each spectrum), which was normalized to the local continuum intensity I_{core}/I_c .

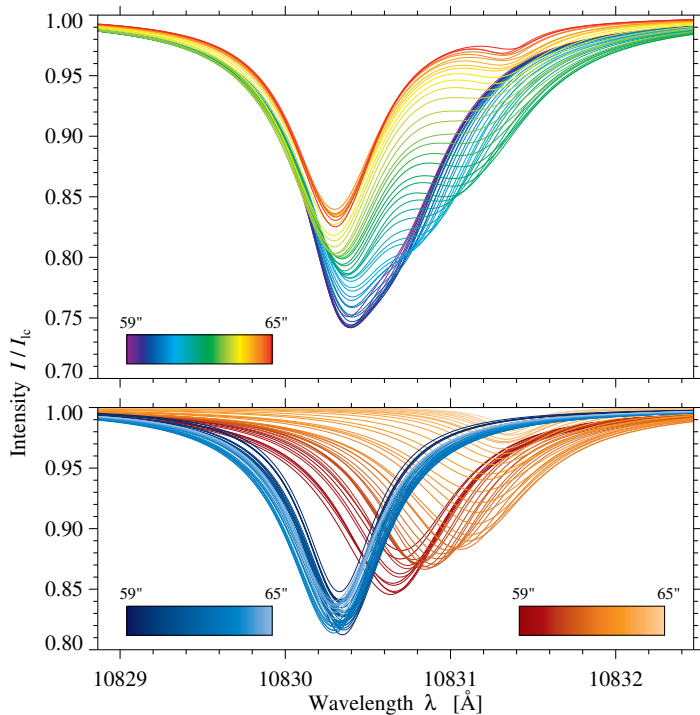


Figure 3.4: Top: synthetic He I dual-flow profiles using the fit parameters retrieved from the double-Lorentzian fits. The color-coded bar extends over a distance of $\sim 6''$ (see Fig. 3.2) linking profiles and positions. Note that dual-flow components are hardly discernible in the first (violet) and last (red) profiles. Bottom: decomposition of the dual-flow profiles into two Lorentzian (blue and red) components.

3.3 Method

Most of the He I 10830 Å intensity profiles show the expected two spectral lines, which comprise the blue and red components. However, a few percent of these profiles, around 3% in our data set, shows a clear signature of a fast component in the He I triplet (see the contours in Fig. 3.2). As a first approach we assume that all profiles have only one component. Hence, we use a single Lorentzian profile to fit all He I profiles:

$$F = 1 - \frac{A_0}{u^2 + 1} \quad \text{with} \quad (3.1)$$

$$u = \frac{x - A_1}{A_2}, \quad (3.2)$$

where A_0 is the amplitude, A_1 the peak centroid, A_2 the half-width-at-half-minimum (HWHM), and the equation implements spectral profiles with a normalized continuum intensity that is set to unity. The profiles were fitted using the Levenberg-Marquardt least-squares minimization (Moré, 1977; Moré and Wright, 1993), where the MINPACK-1 software package was implemented in IDL by Markwardt (2009). An advantage of using this routine is that it is possible to impose independently upper and lower boundaries for each free parameter of Eq. 3.1. As a first approach, we retrieved suitable limits by fitting the mean quiet-Sun profile. The limits were then modified to increase the accuracy of the fits. The fitted wavelength range is automatically adjusted depending on the amplitude of the spectral profile. The larger the amplitude of the line the broader the spectral range. Since the dual-flow profiles are systematically redshifted we did not include the blue component in the analysis.

The LOS velocities inferred with the single Lorentzian fits are shown in the bottom panel of Fig. 3.2. Positive velocities are related to downflows (red) while negative velocities (blue) represent upflows. Note that double-peaked profiles, i.e., dual-flow He I profiles, are not well fitted with a single Lorentzian profile. Since the wavelength is given on an absolute scale, the wavelength reference for the LOS velocities was set to 10830.30 Å, which corresponds to the average laboratory wavelength of the He I red component (10830.25 Å and 10830.34 Å respectively, from the NIST database). The second panel from the top of Fig. 3.2 also shows the equivalent width obtained from the single-Lorentzian fits.

The next step concerns fitting the dual-flow profiles with double-Lorentzian profiles:

$$F = 1 - \frac{A_0}{u_1^2 + 1} - \frac{A_3}{u_2^2 + 1} \quad \text{with} \quad (3.3)$$

$$u_1 = \frac{x - A_1}{A_2} \quad \text{and} \quad u_2 = \frac{x - A_4}{A_5}, \quad (3.4)$$

where $A_{0,3}$ are the amplitudes, $A_{1,4}$ are the centroids, and $A_{2,5}$ are the HWHM of each Lorentzian, respectively. Due to the very short computation time (a few minutes), all spectral profiles were fitted again with two Lorentzians. However, in the future we will adapt the code to only fit the two-component profiles.

An adaptive wavelength range was not used this time. We chose two different wavelength ranges depending on the position of the line core of the He I red component. This ignored the He I blue component in the selected wavelength range. Therefore, if the line core of the He I red component was located below 10830.49 Å, then the wavelength range was $[-0.83, +1.73]$ Å with respect to the line core. Otherwise, if the position of the line core was larger than 10830.49 Å, then the wavelength range was $[-1.37, +1.73]$ Å with respect to the line core.

The initial estimates of the fit parameters A_0 – A_5 were based on the single-Lorentzian fits and on the location of the deepest line core of the dual-flow components. The peak centroid of the fast component is always more redshifted than the slow component. The peak centroid of the slow component is always at rest. The amplitudes A_0 and A_3 are both initially set to the amplitude inferred from the single-Lorentzian fit but they are allowed to vary in the course of the fitting. The parameters A_2 and A_5 have a fixed value of the HWHM of 0.32 Å (mean HWHM values of all the profiles fitted with a single Lorentzian).

In order to localize the dual-flow profiles, different types of these profiles were manually selected and then correlated with all the profiles of the map. The wavelength range for this correlation was between $[10829.50\text{--}10832.56]$ Å. In our particular case, we have selected more than 70 clearly distinguishable dual-flow profiles. Weak dual-flow profiles like, for instance, the first violet and red (too small amplitude) synthetic profiles shown in Fig. 3.4, were not selected because they are too weak to clearly identify the fast component. The median value of the correlation of all profiles were used as a threshold. Hence, only profiles which showed a larger linear correlation than 0.98% were considered as two-component profiles. The contours in Fig. 3.2 encompass these profiles. Developing an automatic algorithm to select the dual-flow profiles remains as future work.

3.4 Results

Some examples to illustrate the quality of the fitting method are shown in Fig. 3.3. All profiles are also marked in Fig. 3.2. Profile ‘a’ represents a common quiet-Sun profile with a LOS velocity close to zero (-0.01 km s^{-1}). An example of a profile with a large equivalent width ($472.4 \text{ m}\text{\AA}$) is shown in panel ‘b’. It arises from a dark filamentary structure in the chromosphere (see Fig. 3.2). However, the LOS velocity is rather small and only reaches -0.3 km s^{-1} (upflow). Profiles ‘c’–‘f’ represent different types of dual-flow profiles. In particular, profile ‘c’ was selected because of its deep line core, i.e., higher absorption. The LOS velocity of the fast component (solid green line) was about 14.8 km s^{-1} while the slow component (solid blue line) only showed about 2.2 km s^{-1} . Profiles ‘d’ and ‘e’ are located near the footpoints of the filamentary structure. The latter had one of the largest inferred velocities of the fast component ($\sim 28.1 \text{ km s}^{-1}$). The remaining profile ‘f’ presents two components with similar amplitudes. The fast component reached a LOS velocity of about 21.5 km s^{-1} .

The normalized frequency distribution of the LOS velocities belonging to the He I fast component is shown in Fig. 3.5. Velocities are in the range of $1\text{--}32 \text{ km s}^{-1}$. The distribution is clearly double-peaked. The maxima are located close to 7 km s^{-1} (subsonic) and 16 km s^{-1} (supersonic), respectively. However, two distinct populations cannot be identified in the FOV, either because the statistical sample is too small or sub-/supersonic flows are transitory in a

confined space. Our normalized frequency distribution is similar to the one reported by [Aznar Cuadrado, Solanki, and Lagg \(2007\)](#) in magnetic field-free areas.

We traced the distribution of the dual-flow profiles along a given slit position. The slit position was chosen close to the footpoints of the filamentary structure and next to the pore. The rainbow-colored bar in Fig. 3.2 shows the location of the profiles. For an easy inspection, the colors in the color bar are associated to the colors of the 44 profiles shown in Fig. 3.4. We do not plot the observed profiles to avoid a crowded display. Instead, Fig. 3.4 shows the synthetic profiles computed from the inferred parameters of the double-Lorentzian fits. One interesting observational feature seen in the top panel of Fig. 3.4 is that the first profiles (violet profiles) only have the slow component. However, once we enter the area of the footpoints (turquoise-green profiles), clearly a fast component appears. The shifted profiles next to the pore exhibit the strongest redshifts (green-yellow profiles) but possess the smallest amplitudes. The bottom panel of Fig. 3.4 shows the individual Lorentzian profiles, which yield the dual-flow profile shown in the top panel. Blue colors always show the slow component while red colors show the fast component. The slow component is always stationary around the reference laboratory wavelength 10830.30 \AA , whereas the fast component is always redshifted reaching values of up to 10831.40 \AA in the line core.

Random and systematic errors can influence the measurements. Using the noise estimate ($\sigma = 3.3\%$) based on continuum intensity variations (see Chap. 3.2) and the fit parameters from Eqs. 3.1 and 3.2 for single Lorentzian profiles, mock spectra are created and analyzed in the same way as the observed data. The linear correlation coefficient for amplitude and HWHM is $\rho = 0.99$ and that for the velocity is $\rho = 0.94$. However, higher Doppler speeds are underestimated. The 3σ -uncertainties for amplitude, velocity, and HWHM are 2.2%, 210 m s^{-1} , and 1.17 pm , respectively, whereas the mean values and the shape of the distributions are barely affected. These random errors also apply to the double-Lorentzian fits, which are however additionally influenced by systematic errors. Dual-flow profiles imply high velocities for the fast component. Therefore, the slow component of the He I red component will be blended with the fast component of the He I blue component.

Using the fit parameters of Eqs. 3.3 and 3.4 for the red He I doublet and scaling them appropriately for the blue line of the He I triplet, mock spectra are generated to obtain an error estimate. The aforementioned blend mostly impacts the blue wing of the slow component of the He I red component, which leads on average to a -300 m s^{-1} zero point offset for the velocity and a 3σ -uncertainty of 1.24 km s^{-1} . On average the amplitude of the slow component is overestimated by 8% with a 3σ -uncertainty of about 27%. In principle, these systematic errors can be reduced either by fitting the entire He I triplet or by appropriately modeling the He I triplet's blue line when fitting the red doublet. In summary, random and systematic errors are sufficiently small to allow a scientific interpretation of the 2D maps of physical parameters (for example those in Fig. 3.2) and of dual-flow He I spectral profiles.

3.5 Conclusions and outlook

In this paper we introduce a simple and rapid technique for determining the velocity of multiple atmospheric components within a single spatial pixel. This technique produces good fits and gives reasonable velocity values, suggesting that after some further tests it can be applied to additional data. For example, an implicit assumption is that the He I line is always optically thin in the wavelength range of the telluric line and has to be tested.

We presented GRIS observations of an EFR containing two small pores. The observations were complemented with simultaneous imaging spectropolarimetry acquired with the GFPI in the photospheric Fe I 6302 \AA line. The FOV for the broad-band images is shown in Fig. 3.1 (red box). In addition, simultaneous observations with CRISP were carried out. Several full spectropolarimetric scans of the photospheric Fe I 6173 \AA line and the chromospheric Ca II 8542 \AA line were taken with a FOV of $54'' \times 54''$ (blue box in Fig. 3.1).

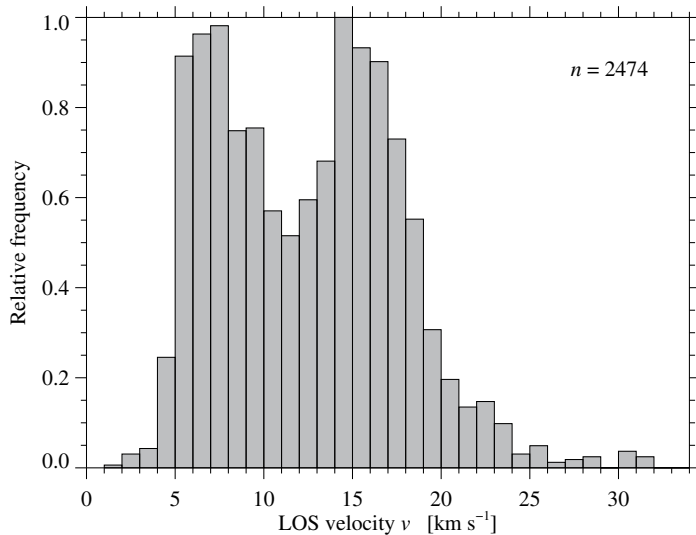


Figure 3.5: Normalized frequency distribution of the LOS velocities of the redshifted He I component obtained with dual-flow fitting using two Lorentzians. The variable n is the total number of pixels which were used for the histogram. The pixels belong to the areas encompassed by the contours shown in Fig. 3.2.

The remaining task will be to extract all the information of the available data sets to understand the physical processes that lead to the formation, evolution, and disappearance of these filamentary structures. The photospheric Fe I 6302 Å and 6173 Å lines from GFPI and CRISP will be used to study the dynamics and temporal evolution of photospheric structures. In addition, the former data will be complemented by the photospheric lines acquired with GRIS, e.g., Si I 10827 Å, Ca I 10834 Å, and Ca I 10839 Å, in order to track the dynamics along several heights within the photosphere. The dynamics in the chromosphere will be covered by the He I 10830 Å triplet as well as with the Ca II 8542 Å line. By analyzing all available GRIS scans we will be able to further characterize the dual-flow profiles seen in the He I triplet and thus elucidate the origin of the two populations shown in Fig. 3.5. The link between the chromospheric filamentary structures and the underlying photosphere is still an open question. Does the plasma of the chromospheric structures, which exhibit supersonic LOS downflows near the footpoints, reach the photosphere? Are the loops also seen in the corona and if yes, what is their behavior? SDO can provide such information (e.g., in the quiet corona and upper transition region with Fe IX 171 Å EUV images) to study the evolution of the loops in the corona. The magnetic field information of the photosphere and the chromosphere will be obtained based on high-resolution imaging spectropolarimetric data observed with CRISP.

Regarding the method to fit the dual flows, we need to expand our study to different data sets. The goal is to build a database, which includes many different types of He I 10830 Å profiles to automatically detect the ones with dual-flow components. This database will include profiles extracted from (more mature) active regions, sunspots, arch filament systems, and quiet-Sun regions. The χ^2 -statistics of the fit can provide hints, where a single component fit is not sufficient. However, noise and the strength of the He I absorption feature potentially obfuscate such a simplistic approach. Therefore, an automatic detection of dual-flow profiles has to rely on easily measured line properties as, for example, the line asymmetry. Additional improvements of the algorithm concern the blue component of the He I triplet. In double-peaked profiles, the fast blue component blends with the slow red component, thus affecting the accuracy of the double-Lorentzian fitting method.

Chapter 4

Tracking photospheric and chromospheric high-velocity features in an arch filament system

This chapter contains a more detailed scientific analysis of the data already introduced in Chap. 3. A new generation of solar instruments provides high spectral, spatial, and temporal resolution for a better understanding of the physical processes that take place on the Sun. Multiple-component spectral profiles are commonly observed with these instruments. Particularly, the He I 10830 Å triplet presents such peculiar spectral profiles, which give information on the velocity and magnetic fine structure of the upper chromosphere. Here, we present observations of an EFR, including two small pores in the photosphere and an AFS in the chromosphere, taken on 2015 April 17 with the very fast spectroscopic mode (~ 1 min) of GRIS. Simultaneous observations of the photospheric 6302 Å line were taken with the GFPI. These data were taken at the 1.5-meter GREGOR solar telescope, located at Observatorio del Teide, Tenerife, Spain. On the island of La Palma, the SST observed the same EFR using CRISP carrying out spectropolarimetry of the photospheric 6173 Å and the chromospheric 8542 Å lines. The aim of this work is to track locations of high velocities within the footpoints of the arch filaments down to the photosphere. The dynamics of the chromosphere will be covered by the He I 10830 Å triplet as well as by the Ca II 8542 Å line. The photospheric Si I 10827 Å and Ca I 10839 Å lines will be used to study the dynamics and temporal evolution of photospheric structures. In addition, the former data will be complemented by the broad-band images from the GFPI.

4.1 Observations

A small EFR, containing two principal pores with opposite polarities and an associated AFS in the chromosphere, was observed between 08:16 UT and 09:20 UT on 2015 April 17. The ROI is located at heliographic coordinates S19 and W4 ($\mu \equiv \cos \theta = 0.97$). Three instruments and two telescopes were involved in this coordinated observing campaign: (1) the GRIS (Collados *et al.*, 2012) and the GFPI (Puschmann *et al.*, 2012; Denker *et al.*, 2010) located at the 1.5-meter GREGOR solar telescope (Schmidt *et al.*, 2012; Denker *et al.*, 2012) at Observatorio del Teide, Tenerife, Spain and (2) the CRISP (Scharmer *et al.*, 2008) located at the SST (Scharmer *et al.*, 2003) located at Observatorio Roque de los Muchachos, La Palma, Spain. The overview of the EFR/AFS in Fig. 4.1 contains all the different FOV of the high-resolution observations, which are superposed on continuum and EUV images and a photospheric magnetogram obtained with the HMI (Scherrer *et al.*, 2012; Schou *et al.*, 2012) and the AIA (Lemen *et al.*, 2012) on-board the SDO (Pesnell, Thompson, and Chamberlin, 2012) at 9:00 UT on 2015 April 17.

GRIS was operated in the very fast spectroscopic mode (no polarimetry) in the He I 10830 Å spectral region (González Manrique *et al.*, 2017). With the fast mode, it is possible to scan the ROI with only a single integration with higher cadence while accepting a higher noise level than in the standard polarimetric mode with several integrations. Preliminary results, discussing noise

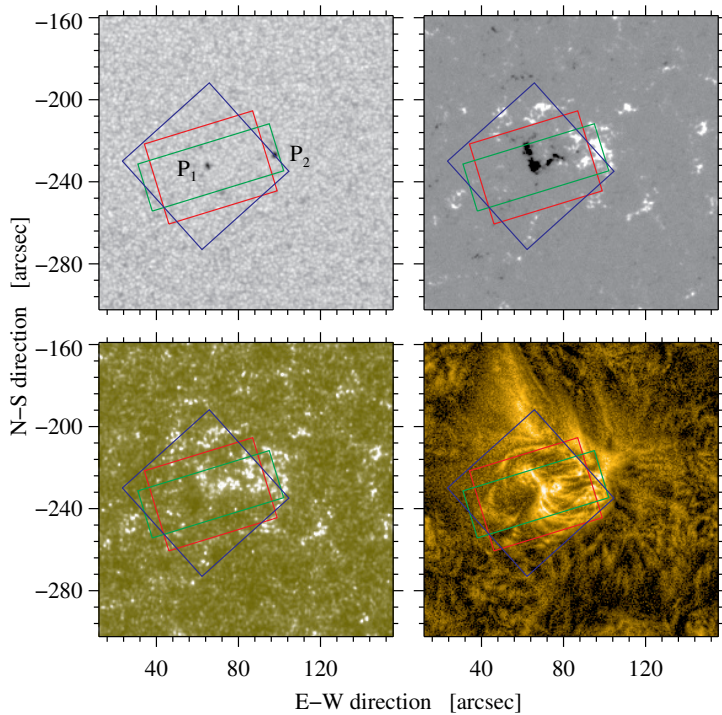


Figure 4.1: Overview of the EFR at 09:00 UT on 2015 April 17: SDO HMI continuum image (*top-left*), HMI magnetogram (*top-right*), AIA 1600 Å image (*bottom-left*), and NAFE-corrected AIA Fe IX 171 Å image (*bottom-right*). The colored rectangles delineate the FOV covered by three instruments GRIS (*green*), GFPI (*red*), and CRISP (*blue*).

level and fitting procedures for dual-components He I 10830 Å spectral profiles were presented in [González Manrique *et al.* \(2016\)](#).

The observed spectral region covers a wavelength range in the NIR of about 18 Å containing the photospheric Si I 10827 Å Ca I 10834 Å, and Ca I 10839 Å lines, the chromospheric He I 10830 Å triplet, and other spectral and telluric lines. The dispersion is $\delta_\lambda = 18.0 \text{ mÅ pixel}^{-1}$, and the number of spectral points along the wavelength axis is $N_\lambda = 1010$. The spatial step size and the pixel size along the slit are very similar, i.e., $0''.134$ and $0''.136$, respectively. The integration time is $t = 100 \text{ ms}$ for one accumulation. A spatial scan consists of 180 steps in total. Thus, the FOV is $66''.3 \times 24''.1$, and it takes about 58 s to cover it. This time interval includes overhead for reading out the camera and writing the data to disk. The observations continued for about one hour resulting in 64 spatio-spectral data cubes. The NIR spectra were taken under good seeing conditions. The GAOS ([Berkefeld *et al.*, 2012](#)) provided real-time correction ensuring a better quality of the spectral data cubes. In this observing period, the GREGOR's alt-azimuthal mount ([Volkmer *et al.*, 2012](#)) introduced an image rotation of 22.3° , which had to be corrected in the data reduction shrinking significantly the common FOV ([González Manrique *et al.*, 2016](#)).

At around 09:00 UT the seeing conditions were good to very good at the GREGOR telescope and fair at the SST. Therefore, the 45th scan at 09:00:56 UT (see Fig. 4.2) was selected as a reference for the GRIS data. The corresponding data sets of GFPI and CRISP were taken at 09:00:54 UT and 09:01:08 UT, respectively. However, there are GRIS scans recorded under better observing conditions. If not otherwise noted in the text, all data refer to this time frame.

GRIS was operated in parallel with GFPI, which scanned the photospheric Fe I 6302 Å line. In this study, only time-series of broad-band images are included (see Fig. 4.3), which were observed with an interference filter (FWHM = 105 Å) centered at 6327 Å. In total 72 data sets with 432 images are available covering the one-hour observing period at a cadence of about 53 s. The FOV of the instrument is $55''.7 \times 41''.5$ (688×512 pixel using the 2×2 -pixel binning) with an image scale of $0''.081 \text{ pixel}^{-1}$. The image rotation is corrected with the same method already employed for the GRIS data cube.

Five time-series were recorded with CRISP consisting of ten data sets with full-Stokes measurements in the photospheric Fe I 6173 Å line and in the chromospheric Ca II 8542 Å line. The observations cover the evolution of the region between 08:47 UT and 9:20 UT with a FOV of $54'' \times 54''$. The spectral sampling of the Fe I line consist of 19 wavelength positions with an

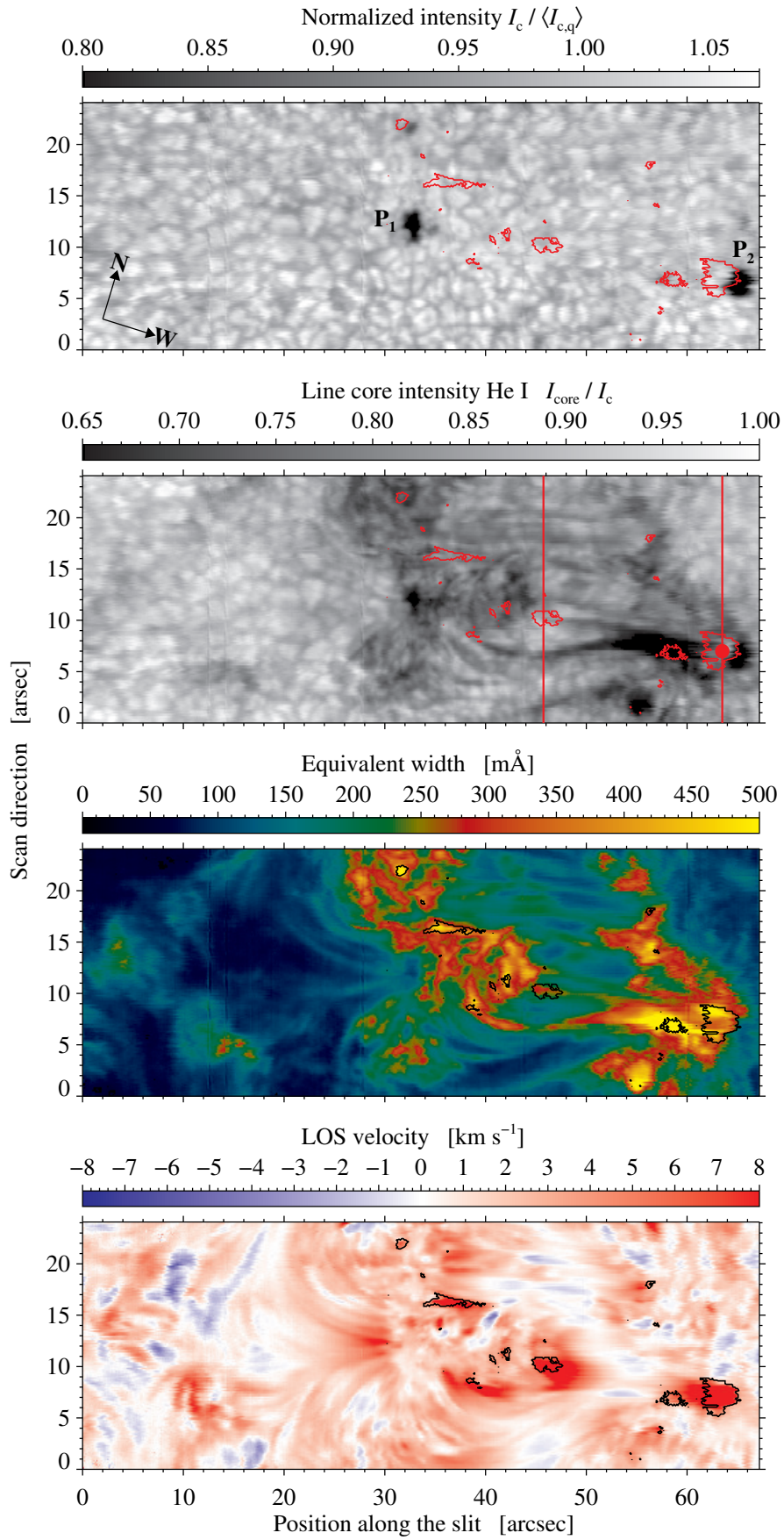


Figure 4.2: Slit-reconstructed GRIS images at 09:00:56 UT on 2015 April 17 of the EFR centered on the pore with negative polarity shown in Fig. 4.1: continuum intensity, line core intensity of the red component of the He I triplet, equivalent width, and He I LOS velocity calculated assuming only a single flow component (*top to bottom*).

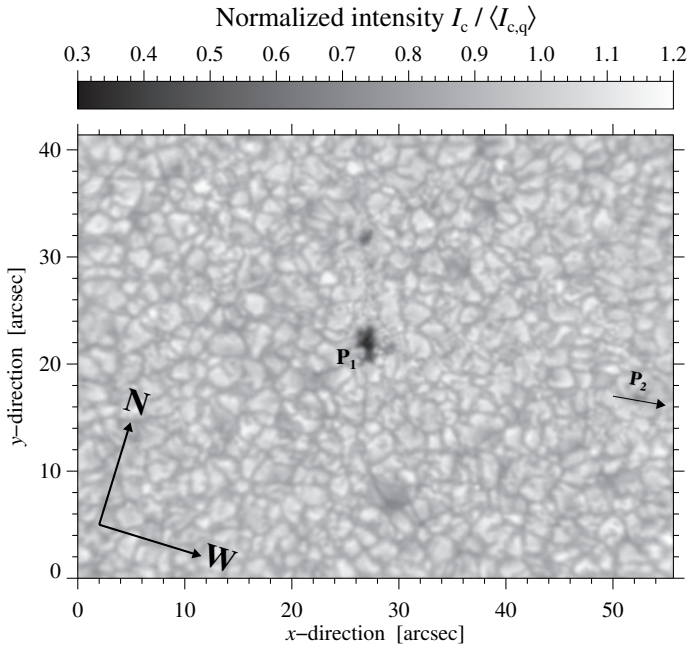


Figure 4.3: MFBD-restored broad-band image at around 6302 Å of the EFR centered on the pore with a negative polarity shown in Fig. 4.1. The image was observed with the GFPI at 09:00:54 UT on 2015 April 17.

equidistant step of 25 mÅ. Thus, the spectral range extends from -225 mÅ to $+225$ mÅ with respect to the central wavelength of the Fe I line at solar disk center, which was measured at the time of the etalon calibration at around 07:30 UT. In addition, the spectral scan includes a continuum position at $+525$ mÅ. The scanning sequence consists of four different modulations states at every spectral position with 12 accumulations. The exposure time amounts to 18 ms for a single image, and a full spectral scan takes about 32 s.

Spectral scans of the photospheric Fe I line are followed by sweeps across the chromospheric Ca II line. Here, the spectral sampling comprises 21 wavelength positions, where the sampling is equidistant in the core (70 mÅ) but becomes coarser in the line wings. The exact wavelength positions are $[0, \pm 70, \pm 140, \pm 210, \pm 280, \pm 350, \pm 455, \pm 595, \pm 735, \pm 945, \text{ and } \pm 1750]$ mÅ. The scanning sequence consists again of four different modulations states at every spectral position but with only six accumulations. The exposure time amounts to 100 ms for a single image, and a full spectral scan takes about 17 s. Sequentially observing both lines leads to a total cadence of about 50 s. The seeing conditions during the observing campaign at the SST were variable. Thus, only the best data set at 09:01:08 UT (see Fig. 4.4) was selected using the Median Filter Gradient Similarity (MFGS, Deng *et al.*, 2015) method and applying it to the continuum images of the Fe I spectral line scans. The MFGS image quality metrics is almost independent of the observed solar feature and thus helps to quantify the seeing conditions. The image scale with this wavelength is $0.059'' \text{ pixel}^{-1}$ (e.g., Esteban Pozuelo, Bellot Rubio, and de la Cruz Rodríguez (2015)). The reflectivity R of the dual etalon Fabry-Pérot amounts to 84.5% for the low resolution etalon and 93.5% for the high resolution etalon, with a FWHM of 181.7 mÅ and 49.2 mÅ respectively.¹

Context data is provided by SDO, where HMI takes full-disk filtergrams at six wavelength positions at $[\pm 34, \pm 103, \text{ and } \pm 172]$ mÅ around the center of the photospheric Fe I 6173.3 Å line. The filtergrams are combined to form continuum intensity images, LOS magnetograms, and Dopplergrams at a 45 s cadence, and the image scale is $0''.5 \text{ pixel}^{-1}$. The longitudinal magnetograms are obtained with a precision of 10 G and allow us to track the temporal evolution of the magnetic flux contained within the active region. The response of upper atmospheric layers, i.e., the transition region and corona, is monitored at different plasma temperatures with EUV and UV images provided by AIA at a cadence of 12 s and 24 s, respectively. The image scale of $0''.6 \text{ pixel}^{-1}$ is slightly larger as compared to HMI because explosive events like coronal mass ejections, filament eruptions, and flares extend beyond the solar limb. Thus, a larger

¹dubshen.astro.su.se/wiki/index.php?title=CRISP

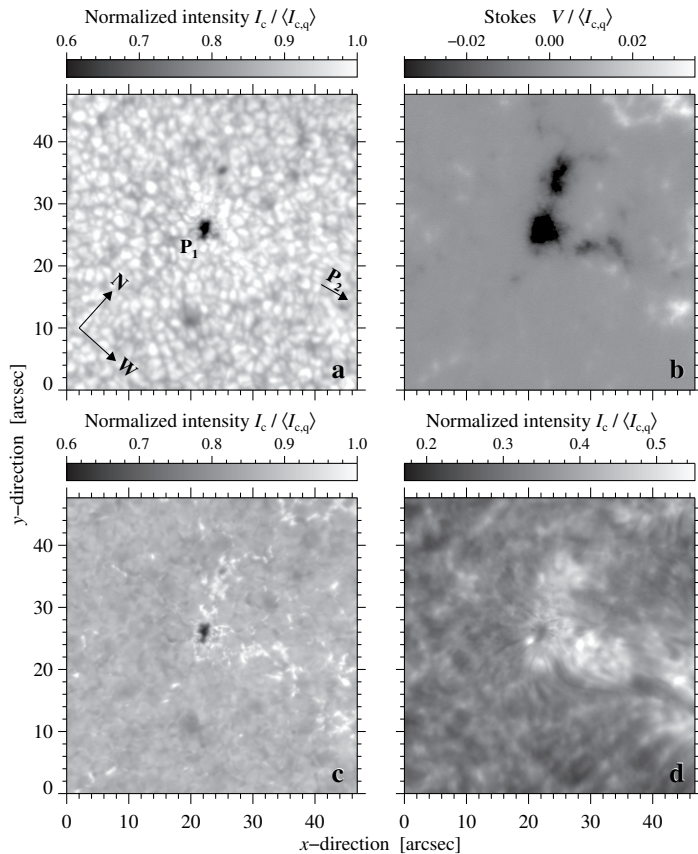


Figure 4.4: Restored CRISP images at 09:01:08 UT on 2015 April 17 of the EFR centered on the pore with negative polarity shown in Fig. 4.1: continuum intensity of the photospheric Fe I 6173 Å line (*top-left*), core of the negative polarity Stokes V of Fe I 6173 Å line (*top-right*), blue wing of the chromospheric Ca II 8542 Å line (*bottom-left*), and line core intensity of the chromospheric Ca II 8542 Å line (*bottom-right*).

FOV is required accommodating an image size up to $1.3 R_{\odot}$. The EUV images are beneficial establishing the topology of low-lying filamentary structures and overarching loops, which are indicative of the magnetic connectivity within the active region and its surroundings.

4.2 Data reduction

Reduction and calibration of the GRIS data cube includes standard dark and flat-field corrections (González Manrique *et al.*, 2016). Wavelength calibration comprises orbital motions and solar gravity redshift corrections, as described by Kuckein, Martínez Pillet, and Centeno (2012b). Hence, the LOS velocities refer to an absolute scale. Common fringes, dust particles along the slit, and abnormal intensity peaks are removed, and the proper continuum of the spectral line is determined. In addition, the telluric line at 10832.108 Å was eliminated from the spectra. This telluric line interferes in some cases with the fast component of the He I 10830 Å triplet González Manrique *et al.* (2016). The slit-reconstructed continuum and the line-core intensity map of the red component are depicted in the first and second panel of Fig. 4.2, respectively.

The data reduction of the GFPI broad-band images was carried out with the data reduction pipeline sTools (Kuckein *et al.*, 2017). Dark and flat-field corrections were applied to the broad-band images. The seeing conditions were monitored using the MFGS image quality metrics. This gives also a feedback, which data set of the time-series has the best data quality. However, the broad-band images were restored with Multi-Frame Blind Deconvolution (MFBD, Löfdahl, 2002) without frame selection. Figure 4.3 shows a restored broad-band image taken at 09:00:54 UT under very good seeing conditions.

The CRISPRED data pipeline (de la Cruz Rodríguez *et al.*, 2015) was used for the CRISP imaging spectropolarimeter. We decided to just destretch the data and to do without image restoration. Standard data reduction includes, among others, bias subtraction, flat-field correction, data demodulation, prefilter correction, and in the case of the Ca II line ‘backscatter’ correction (de la Cruz Rodríguez *et al.*, 2013). In addition, further data reduction steps are needed in preparation for data analysis: (1) Residual fringes in the spectra hamper the analysis

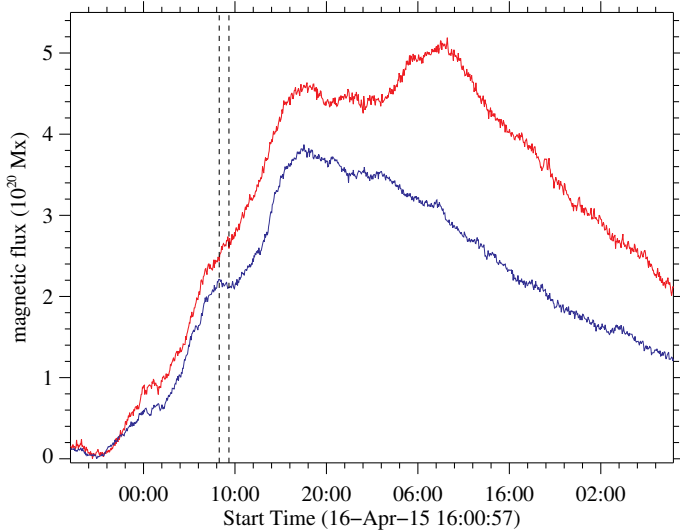


Figure 4.5: Temporal evolution of the magnetic flux covering the entire EFR. The red and blue solid lines represent the magnetic flux of the positive and negative polarity, respectively. The dashed vertical lines mark the time of the high-resolution observations with GREGOR.

of polarimetric data. These fringes were removed. (2) The remaining residual cross-talk is corrected using the technique described by [Schlichenmaier and Collados \(2002\)](#), i.e., the cross-talk from Stokes I to Q , U , and V as well as that from V to Q and U . (3) The last step is to normalized the Ca II spectral line to the local continuum intensity. The corresponding average Stokes I profile was compared to an atlas spectrum obtained with the FTS ([Brault and Neckel, 1987](#)).

The AIA and HMI data were downloaded from the Virtual Solar Observatory (VSO) in level 1.0 and 1.5 format, respectively. The AIA data have already been partially processed including bad-pixel removal, depiking, and flat-fielding but they are not exposure time corrected. The HMI data were also photometrically corrected. Moreover, maps of physical observables were already created from individual filtergrams, i.e., continuum images, magnetograms and Dopplergrams. All data were processed with the instrument-specific data pipeline, which is a part of the SolarSoft software library ([Bentley and Freeland, 1998](#); [Freeland and Handy, 1998](#)) mainly implemented with the IDL. This adjusts different AIA filtergrams and HMI data products to a common image scale and coordinate system. Finally, all data were compensated for differential rotation with respect to the central meridian. The reference images was taken at 00:00:57 UT on 2015 April 17 because at this time the EFR was exactly at the central meridian. As the plasma parameters can evolve fast in an EFR, the observing times have to be stated very precisely when comparing data from different instruments. Therefore, we always use the midpoint of the particular AIA or HMI exposure given in universal time.

4.3 Data analysis

4.3.1 Temporal evolution of emerging magnetic flux

The temporal evolution of the emerging magnetic flux is based on time-series of HMI magnetograms compensated for solar differential rotation. We assume that the magnetic field is mostly perpendicular to the solar surface, which is justified because the FOV only contains pores but no sunspots with more horizontal fields in the penumbra. The data cover both flux emergence and decay, and the high-resolution data were recorded roughly in the middle of the flux emergence period. The rectangular ROI includes the entire EFR. Rise and decay the magnetic flux is tracked for both magnetic polarities as shown Fig. 4.5, where the red and blue curves correspond to the positive and negative magnetic polarities, respectively. The pre-existing magnetic flux was determined as the median value of a two-hour time-series just before onset of the flux emergence and was subtracted separately for each polarity.

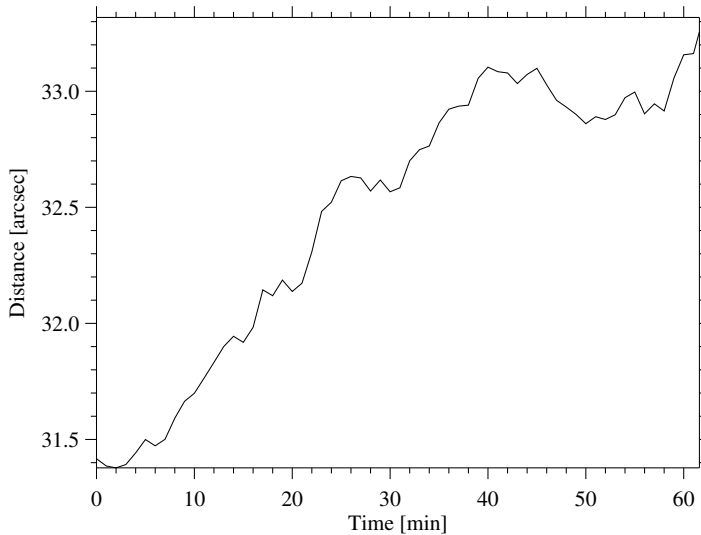


Figure 4.6: Temporal evolution of the center-to-center distance between pores P_1 and P_2 . The distance was calculated using the time-series of 64 slit-reconstructed continuum images.

4.3.2 Center-to-center distance of pores

The center-to-center distance of the two pores is derived from the time-series of 64 slit-reconstructed GRIS continuum images. The continuum images are smoothed by convolving them with a two-dimensional Gaussian of 32×32 pixels and a FWHM = 16 pixels. A two-dimensional Gaussian fit (25×25 pixels) centered on the intensity minimum of the pore yields the position of the pore’s midpoint with sub-pixel accuracy. The separation of the two pores is given as the Euclidean distance between their centers, which evolves as depicted in Fig. 4.6.

4.3.3 Line-of-sight velocities of NIR lines

Spectral line fitting was applied to the Si I 10827 Å (Gaussian) and the Ca I 10839 Å (Lorentzian) spectral lines to infer the respective LOS velocities. The profiles were fitted using the Levenberg-Marquardt least-squares minimization as implemented in the MPFIT IDL software package [Markwardt \(2009\)](#). The wavelength ranges were ± 0.36 Å and ± 0.45 Å for the Si I and Ca I lines, respectively. The wavelength references for the LOS velocities were set to the laboratory wavelengths 10827.09 Å (Ritz wavelength) and 10838.97 Å (observed wavelength) for the Si I and Ca I lines, respectively, which were taken from NIST data base. The Ritz wavelengths, derived from the transition probabilities of the lower and upper levels, are potentially more precise than the observed wavelengths, specially in the vacuum UV spectral band.

Generally, the He I 10830 Å triplet in the observed data cube consists just of the blue and blended red components. Nevertheless, a small percentage of spectral profiles reveals clear signatures of “dual flows” ([Schmidt, Muglach, and Knölker, 2000](#)), which splits the red component into a slow and fast component. An approach to fit the two parts of the red component is described by [González Manrique *et al.* \(2016\)](#) based on a subset of the current data set. Initially, all profiles are fitted with a single Lorentzian profile using a Levenberg-Marquardt least-squares minimization implemented in the MPFIT IDL software package ([Markwardt, 2009](#)). The wavelength range automatically adjusts to the line depths, i.e., it is broader for strong lines, to enhance the accuracy and stability of the fits ([González Manrique *et al.*, 2016](#)). The wavelength reference for the LOS velocities is the average laboratory wavelength 10830.30 Å of the blended red component given by the NIST data base.

In a second step, only dual-flow profiles are fitted with a double-Lorentzian profile. This deviates from the approach in [González Manrique *et al.* \(2016\)](#), where all profiles were fitted with a double-Lorentzian followed by an evaluation, whether single- or double-peaked profiles are more appropriate. In the current implementation dual-flow profiles are automatically detected based on the single-Lorentzian fits. Their locations are indicated by the red and black contours in all panels of Fig. 4.2. Selection criteria for dual-flow profiles are: (1) strong asymmetry of the blue and red line wings at half the line depth, (2) presence of two clearly defined minima, where

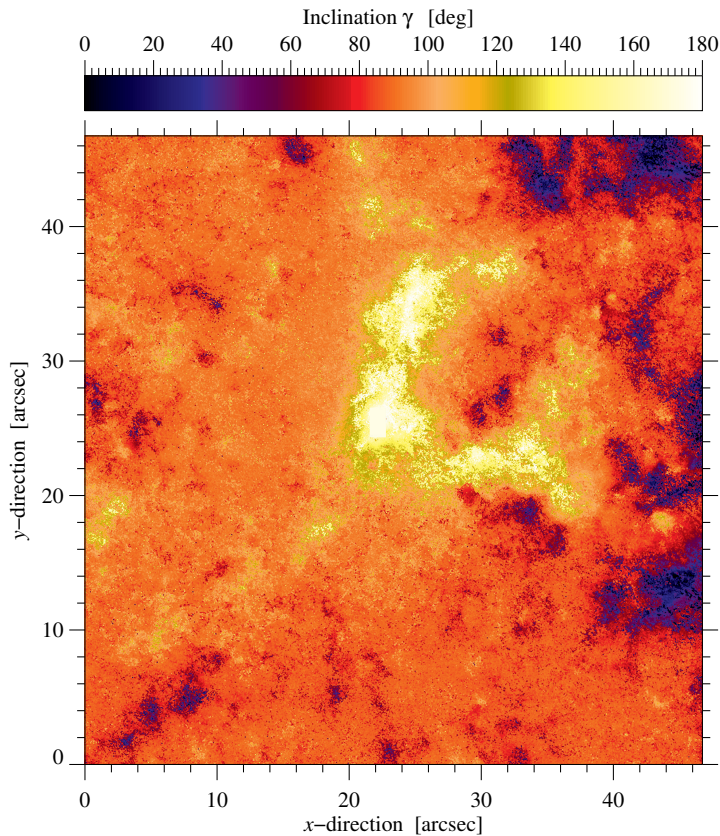


Figure 4.7: Magnetic field inclination γ inferred with SIR at an optical depth of $\log \tau = -1$ corresponding to the CRISP data of the photospheric Fe I 6173 Å line in Fig. 4.4.

the line depths is deeper in the fast component, (3) very large FWHM of the line profiles, and (4) line core is strongly redshifted with respect to the mean central wavelength.

4.3.4 Bisectors and spectral inversions of the Si I line

The bisectors (e.g., [Stix, 2004](#)) of the Si I line were computed for the full time-series of spatio-spectral data cubes. The wavelength positions of the bisectors were calculated in 10%-steps of the line depth using linear interpolation in both line wings. Maps of the LOS velocity were derived for each point on the ordinate (0%, 10%, ..., 80%) because bisector points closer to the (local) continuum did not deliver reliable velocity maps (see Chap. 4.4.3). The value of 0% refers to the line core. The velocities were measured with respect to the laboratory wavelength of 10827.09 Å taken from the NIST data base.

Two different LOS velocity maps taken at 08:42:22 UT and 09:00:56 UT were inferred from the Si I spectral line using the height-dependent SIR ([Ruiz Cobo and del Toro Iniesta, 1992](#)) code. These velocity maps based on spectral line inversion were then compared with those originating from the bisector method. The height dependence in SIR is expressed in logarithmic units of the optical depth $\log \tau$. The Harvard-Smithsonian reference atmosphere (HSRA, [Gingerich et al., 1971](#)) was chosen as an initial guess for the solar atmosphere. This atmospheric model was iteratively perturbed to match the observed and computed Stokes I profiles. However, the perturbations are only calculated in a few nodes in the atmosphere to reduce both the computation time and number of free parameters. The remaining points along the optical depth are obtained by a linear or cubic-spline interpolation. For these particular inversions we used up to two nodes for the LOS velocity.

4.3.5 Inversion of the photospheric Fe I line

The inversion of the Fe I 6173 Å line was carried out with the SIR code but only for the best map of the time-series (see Fig. 4.4). The observed Stokes profiles can be affected by a significant amount of stray-light. The stray-light level was determined based on the mean

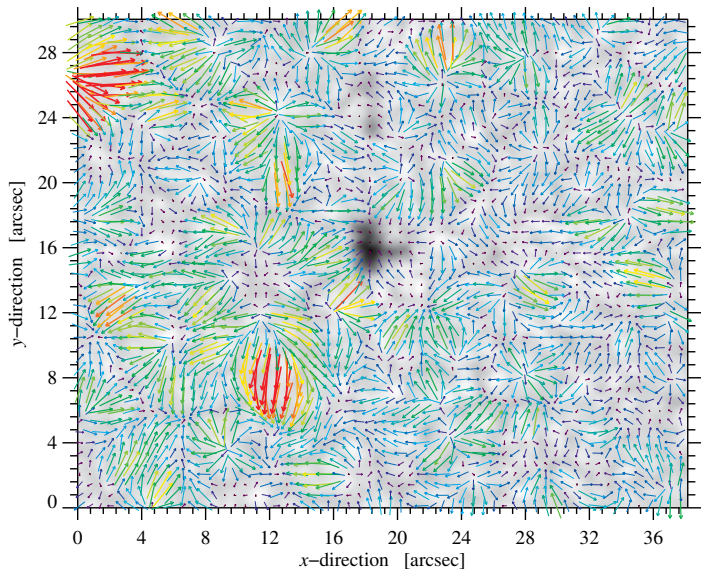


Figure 4.8: Horizontal flow field around the pore P_1 computed with LCT using GFPI broad-band images. The rainbow colored vectors are superposed on the average image of the time-series. Red vectors indicate flow speeds in excess of 1.2 km s^{-1} .

quiet-Sun spectrum. In principle, the stray-light correction could be implemented as a free parameter in the SIR code. However, in the inversion of the Fe I 6173 Å line, only a fixed value of 23% of the continuum intensity was used. This fixed value was derived and validated by inspecting 20 profiles with strong Stokes V signals. In this case, stray-light was a free parameter of the inversion. The HSRA served again as a first guess for the solar atmosphere, and the height-dependent model was iteratively perturbed to match the computed Stokes I , Q , U , and V profiles with the observations. The computational effort increased significantly as compared to the inversions presented in Chap. 4.3.4 because the perturbations were calculated with a maximum of four nodes for the temperature and up to three nodes for other parameters. Linear or cubic-spline interpolation was used for the remaining points along the optical depth.

4.3.6 Inversion of the chromospheric Ca I line

The information encoded in the chromospheric Ca II 8542 Å spectral line was analyzed using the non-LTE synthesis and inversion code NICOLE (Socas-Navarro *et al.*, 2015). The inversion process is especially complex and very time-consuming for non-LTE lines. Hence, we concentrated only on a small ROI of 49 pixels at coordinates (30'', 23'') in one snapshot taken at 09:01:08 UT (see Fig. 4.4). In this region, the polarization signals in Stokes Q , U , and V were small. However, the region coincided with one of the footpoints of the AFS which showed the second-strongest velocities beyond those close to pore P_2 . Since the aim is to retrieve the LOS velocities, we focused on the inversion of the Stokes I profiles inside this region.

For the inversions, we took into account the isotopic splitting of the Ca II NIR line (Leenaarts *et al.*, 2014) and used the FALC quiet-Sun model (Fontenla, Avrett, and Loeser, 1993) as an initial guess for the atmosphere. The observed Stokes I profiles were convolved with the instrumental profile of CRISP. In a first attempt, we carried out standard inversions with one initial atmosphere. Up to eight and twelve nodes were used for the LOS velocity and temperature, respectively. However, after testing with different nodes in all physical parameters the fit results of the synthetic intensity profiles were not satisfactory. Therefore, we opted for inversions with two atmospheric components. All parameters of both model atmospheres were the same except for the LOS velocities. One model had a small and constant positive velocity, i.e., redshift, while the other one was at rest. We used up to five nodes for the temperature and four for the LOS velocity. Micro- and macroturbulence were allowed to change by giving them only one node. The filling factor was set as a free parameter. This setup yielded reliable inversions of the chromospheric Ca II NIR line.

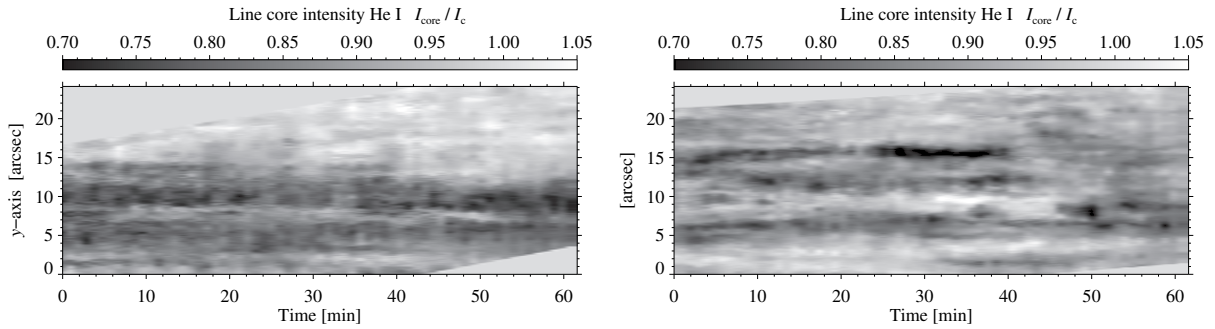


Figure 4.9: Space-time diagram of the He I line-core intensity I_{core} (normalized to the continuum intensity I_c) taken at the footpoint (*top*) and loop top (*bottom*) of the AFS. The positions are marked in Fig. 4.2 by vertical lines.

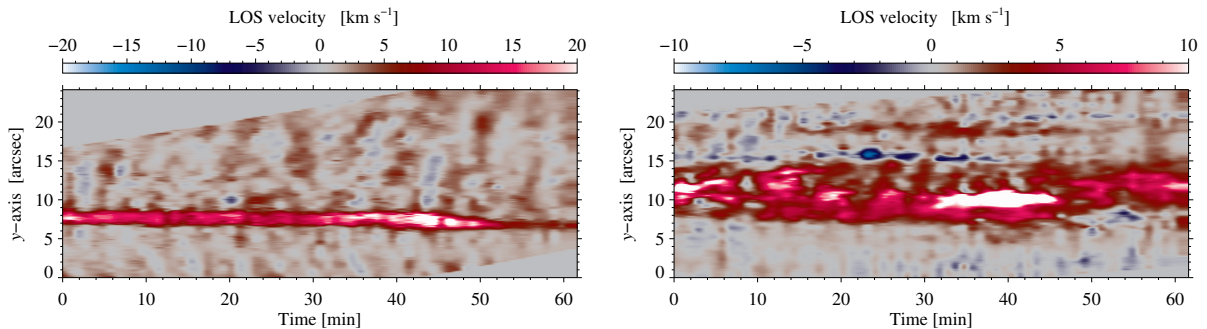


Figure 4.10: Space-time diagram of the He I LOS velocity (single-component fit) taken at the footpoint (*top*) and loop top (*bottom*) of the AFS. The positions are marked in Fig. 4.2 by vertical lines.

4.3.7 Horizontal proper motions

To compute the horizontal proper motions around the central pore, we applied LCT (November and Simon, 1988) to the GFPI time-series of MFBD-restored broad-band images. The implementation of the LCT algorithm is described in Verma and Denker (2011) and a comparison with radiation hydrodynamics simulations of granulation is given in Verma, Steffen, and Denker (2013). The images of the time-series were aligned, and the signature of the five-minute oscillation was removed using a subsonic Fourier filter, where the photospheric sound speed was chosen as the cut-off velocity. The LCT technique computes for each pixel local cross-correlations over 48×48 -pixel image tiles with a Gaussian kernel having a $\text{FWHM} = 1200 \text{ km}$. Thus, the sampling window is adapted to track features with sizes corresponding to granules. The time cadence was $\Delta t = 53 \text{ s}$, and the flow maps were averaged over $\Delta T = 63 \text{ min}$. The resulting average flow map is displayed in Fig. 4.8, where the FOV is much smaller than in Fig. 4.3 because of misaligned image, image rotation during the time-series, and the width of the sampling window.

4.4 Results

The high-resolution observations cover a short period in the lifetime of the EFR, which is marked by dashed horizontal lines in Fig. 4.5. At the time, when the observations started, flux emergence was roughly halfway finished. Thus, the outcome of this study primarily addresses questions related to continuous flux emergence. The lifetime of the EFR is about three days as observed with the SDO data (see Fig. 4.1). The EFR has two main pores with opposite polarities, and they become visible in the SDO/HMI magnetograms at around 20:08 UT on 2015 April 16. In the HMI continuum images the pores become visible around two hours later. Many small magnetic features with positive and negative polarities emerge between the two main pores. Some of them are canceling but others moves until they merge with the main pore of the same polarity. Approximately one day after emergence at 20:00 UT on 2015 April 17, the

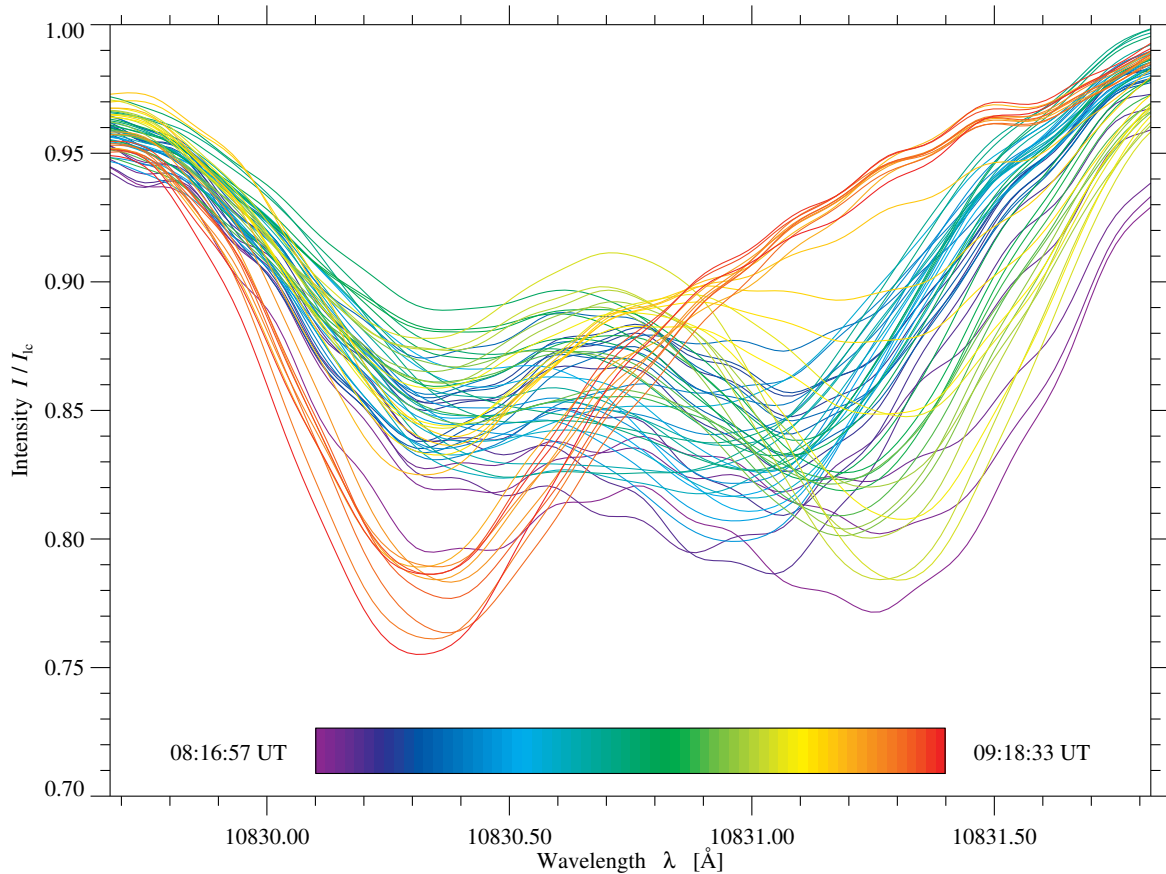


Figure 4.11: Temporal evolution of spectral profiles (normalized to the local continuum intensity I_c) for the red component of the He I triplet. The rainbow-colored bar marks the elapsed time after the start of the one-hour time-series. The spectra were taken at a strong downflow kernel marked by filled circles in Fig. 4.2. The spectra were slightly smoothed to avoid a cluttered display.

pores reached their maximum size and magnetic flux. The leading pore with positive polarity seems more fragmented while the negative pore is bigger and has a diameter of around $5''$. The negative flux reaches values up to 3.8×10^{20} Mx and the positive polarity up to 5×10^{20} Mx (see Fig. 4.5). The distance between the pores was obtained during the observing time (see Fig. 4.6) with an initial value of about $31.4''$. The distance was increasing during 40 min. After this time the distance between the pores stabilized around $33''$.

An AFS is visible in the chromosphere. The arch filaments connect both pores with opposite polarities and other small-scale magnetic elements that are emerging mainly between them. The individual arch filaments change with time during the observations on time-scale of minutes (see Chap. 4.4.2). The inversions of the photospheric Fe I 6173 Å line inferred with SIR (optical depth of $\log \tau = -1$) gives values of the magnetic field B in the central pore (negative polarity) of about 2500 Gauss. While the magnetic field values B of the small-scale magnetic elements around the main pore have values up to 1500 Gauss. Comparing the values of the inclination γ (see Fig. 4.7) with respect to the LOS at the same optical depth and the line core intensity of the chromospheric Ca II 8542 Å line (see Fig. 4.4), it is evident that the footpoints of the arch filaments are placed where the magnetic field lines are nearly vertical as expected. Note that 180° refers to downward field lines, and 0° indicates the upward direction.

4.4.1 Inflows associated with the central pore

The central pore P_1 in all ROIs of the high-resolution instruments possesses negative polarity. It also served as the lock point for the AO systems. Therefore, the highest image and data quality is expected in the vicinity of the central pore. To quantify the horizontal proper motions in and

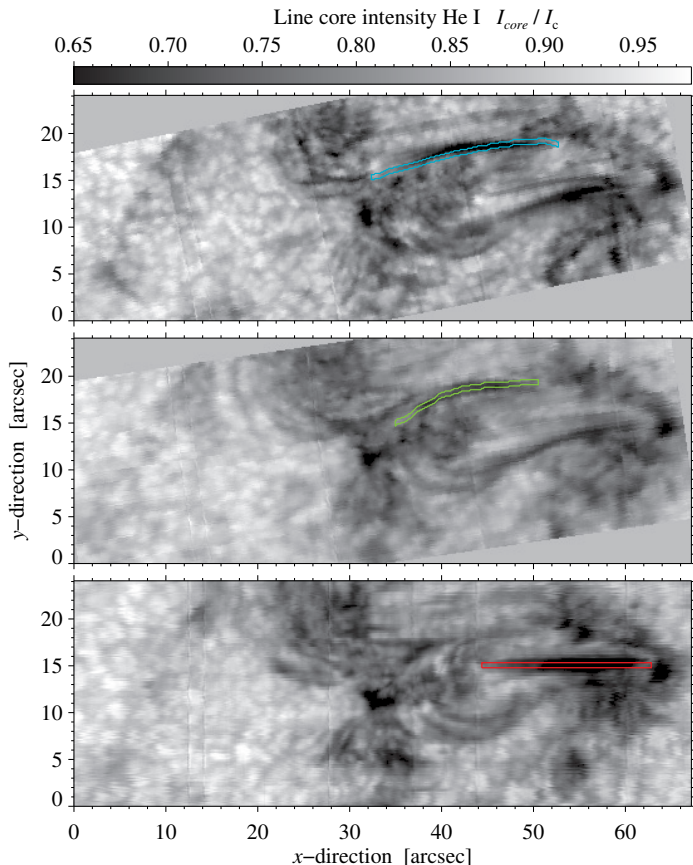


Figure 4.12: Slit-reconstructed GRIS images at 08:16:57 UT (*bottom*), 08:40:23 UT (*middle*), and 08:49:16 UT (*top*) on 2015 April 17. The contours outline different arch filaments at different times.

around this pore in the EFR, we computed an LCT map (see Fig. 4.8). The mean velocity was $\bar{v} = 0.48 \text{ km s}^{-1}$ with a standard deviation of $\sigma_v = 0.25 \text{ km s}^{-1}$. As expected in the pore’s surrounding we find many diverging centers with the size of granulation and mesogranulation. Additionally, in the LCT map we capture flows associated with expanding granules. The signature of such expanding granules can be seen at coordinates $(12'', 8'')$ in Fig. 4.8. The mean velocity in the expanding granule was $\bar{v} = 1.2 \text{ km s}^{-1}$. Recently, similar expanding granules were observed by Verma *et al.* (2016), who interpreted the striking flow pattern and the exceptional size of the expanding granule as an indicator of ongoing flux emergence. Another prominent horizontal flow feature are the inflows associated with the central pore. According to Verma and Denker (2014) the inflows signify the coalescence of the small-scale flux tubes forming a larger magnetic feature like a solar pore. Furthermore, converging velocity patterns are also present in the region above the pore, where small dark features resembling magnetic knots are located.

4.4.2 Temporal evolution

The fast cadence of GRIS offers access to the highly dynamic chromosphere, which is monitored in this study using the red component of the He I 10830 Å triplet. The time-series of slit-reconstructed He I line-core intensity images (see example in Fig. 4.2) affirms the good to very good seeing conditions and demonstrates the stable performance of the AO system. Moments of mediocre seeing conditions are rare but become more frequent towards the end of the time-series. They appear in the line-core intensity maps as elongated stripes with low contrast and correspond typically to time intervals of about 10 s. However, for most of the time, the granulation pattern and chromospheric He I absorption features with sub-arcsecond fine structure are very prominently visible.

Spectral scan No. 45 at 09:00:56 UT (see Fig. 4.2) serves as reference for alignment and rotation correction of all spectral data cubes. The ROI contains two pores of opposite magnetic polarity, one in the center of the ROI at the AO lock-point and the other one at the right edge of the ROI. New magnetic flux is still emerging, which leads to an AFS connecting both pores

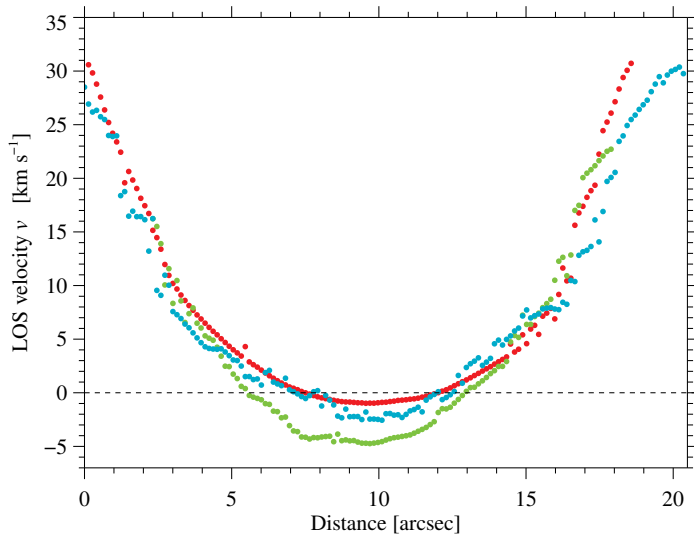


Figure 4.13: LOS velocities inferred from the He I triplet’s red component. The velocities are calculated along three arch filaments shown in Fig. 4.12. The colours of the plot symbols correspond to the contour lines in that figure.

and other small-scale magnetic elements with multiple dark filament strands. Individual arch filaments change significantly on time-scales of minutes or less. Time-lapse movies reveal motions along the arch filaments, which are consistent with continuously emerging Ω -loops, where cool material rises to chromospheric heights and beyond at the loop tops and then drains towards the footpoints of the loops.

The most interesting features in the ROI are the loop tops and footpoints of the arch filaments. Two vertical lines in Fig. 4.2 mark the positions, where space-time diagrams display the temporal evolution of the He I line-core intensity and LOS velocity in Figs. 4.9 and 4.10, respectively. Light gray areas indicate missing information in the ROI. The majority of LOS velocities results from single-component fits to the observed line profiles unless dual-component fits are more appropriate. In this case, the LOS velocity refers to the fast component. The bottom panel of Fig. 4.9 tracks the rising loop top of a thin dark arch filament ($y \approx 17''$), which becomes darkest about 30 min after the start of the time-series and abruptly vanishes after just over 40 min. A second, more persistent footpoint of a different loop exists at $y \approx 8''$, which shows more substructure streaming rapidly past the crosswise line. The associated LOS velocities (bottom panel of Fig. 4.10) of the former arch filament show upflows approaching 5 km s^{-1} , which are typical for a rising Ω -loop, whereas the latter absorption feature near the footpoint of a loop exhibits strong variations of downflows in excess of 10 km s^{-1} . The top panels of Figs. 4.9 and 4.10 are dedicated to a small kernel with a diameter of $2\text{--}3''$, where strong persistent downflows are present exceeding 20 km s^{-1} , sometimes even reaching more than 40 km s^{-1} . These downflows intensify just before the kernel vanishes at $t \approx 50 \text{ min}$. At this location He I absorption is moderately strong and does not change much in time. This downflow kernel is pointed out by filled circles with diameters of about $1.4''$ at coordinates $(63.2'', 7'')$.

The temporal evolution of He I spectra within this downflow kernel deserves further scrutiny. In Fig. 4.11, the time since the start of the time-series is color coded. The displayed spectra arise from 69 locally averaged spectra contained within the filled circles. They were slightly smoothed for better display but still contain some high-frequency oscillations due to fringes in the NIR spectra. The region was specifically selected because of the strong downflows and the presence of dual-component He I spectral profiles. The rainbow color code immediately reveals time intervals, where the shape of the red component significantly changes. Initially, the slow and fast component form w-shaped profiles with well separated minima of roughly the same intensity. Their line-core intensities are in the range $I_{\text{core}}/I_c \approx 0.80\text{--}0.85$. At around 08:41 UT, the combined profile of the slow and fast component becomes more ‘bathtub’-like, i.e., the minima are no longer well separated. Starting at 08:50 UT, the fast component becomes dominant reaching line-core intensities of $I_{\text{core}}/I_c < 0.8$, and the difference in line-core intensity between the slow and fast component can be as large as $\Delta I \approx 0.1$. The transition to single-component profiles begins abruptly at 09:08 UT resulting in profiles with extended wings towards

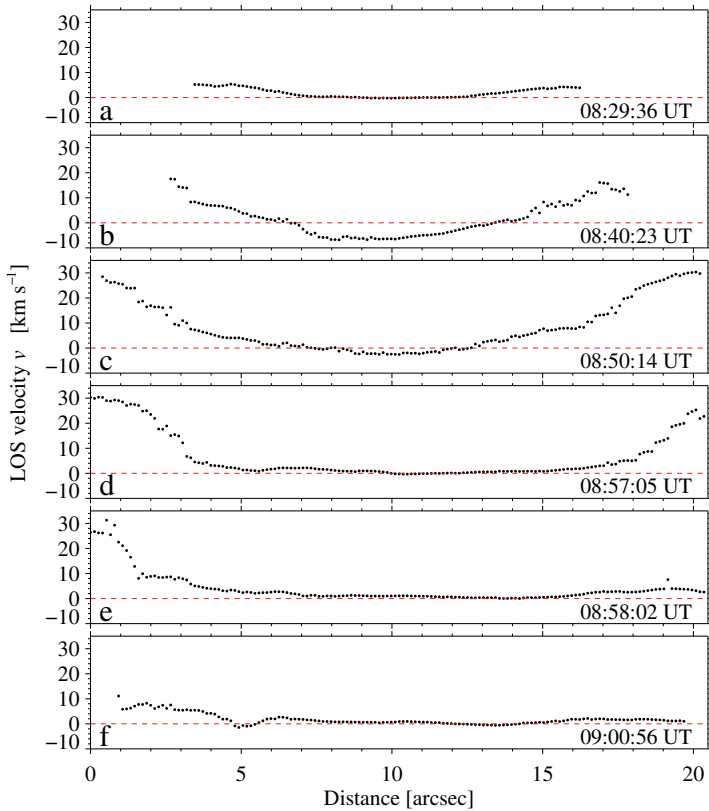


Figure 4.14: Temporal evolution of the LOS velocity along a single arch filament (blue and green contours in Fig. 4.12) based on the He I triplet’s red component.

higher wavelengths and in deep line cores of the slow component.

It is also possible to track in time the LOS velocities along a single arch filament. Figure 4.12 contains three slit-reconstructed GRIS images at three different times. The contours depict three arch filaments at 08:16:57 UT (red contour), 08:40:23 UT (green contour), and 08:49:16 UT (blue contour) on 2015 April 17. Note that the green and the blue represent the same arch filament at different time. We inferred the LOS velocities along the contours and calculated the mean values of five pixels in the y -direction for every position in the x -direction. The mean LOS velocities for every single arch filament are shown in Fig. 4.13. As expected the loop-tops show upflows up to 5 km s^{-1} in the case of the green arch filament because it is the same as in Fig. 4.10. As mentioned before they are the loop-top of new emerged loops transporting relatively cool material to the chromosphere. Then the material drains down towards the two opposite polarities where the footpoints are placed. Thus, as expected we find supersonic downflows velocities in the footpoints of these arch filaments. The speeds are higher as we approach the footpoints. Similar results are presented, for example, by Xu, Lagg, and Solanki (2010) and Lagg *et al.* (2007). The distance between the footpoints of these three arch filaments are up to $20''$ in the case of the one outlined by the red contour.

It is also possible to track the temporal evolution of a single arch filament and to calculate the LOS velocities along the arch filament. We selected the arch filament outlined by blue and green colours in Fig. 4.12. This arch filament is interesting because the single arch filament emerged and disappeared during the observing time. Figure 4.14 shows the temporal evolution of the LOS velocities along the arch filament at six different moments. The life-time of the arch filament is about 25–30 min, which is at the upper end of values given in literature of 10–30 min (Chou, 1993). Initially, the velocities are near 0 km s^{-1} at the loop-tops, and there are also small downflows near the footpoints. After approximately 10 min the loop-tops exhibit strong upflows (up to 5 km s^{-1}) and supersonic downflows at the footpoints (up to 31 km s^{-1}). Near the end, the velocities approach 0 km s^{-1} in the whole arch filament. In addition, the distance between the footpoints increases with time. At the beginning the distance is around $15''$ and at the end of the time-series the distance amounts to $20''$.

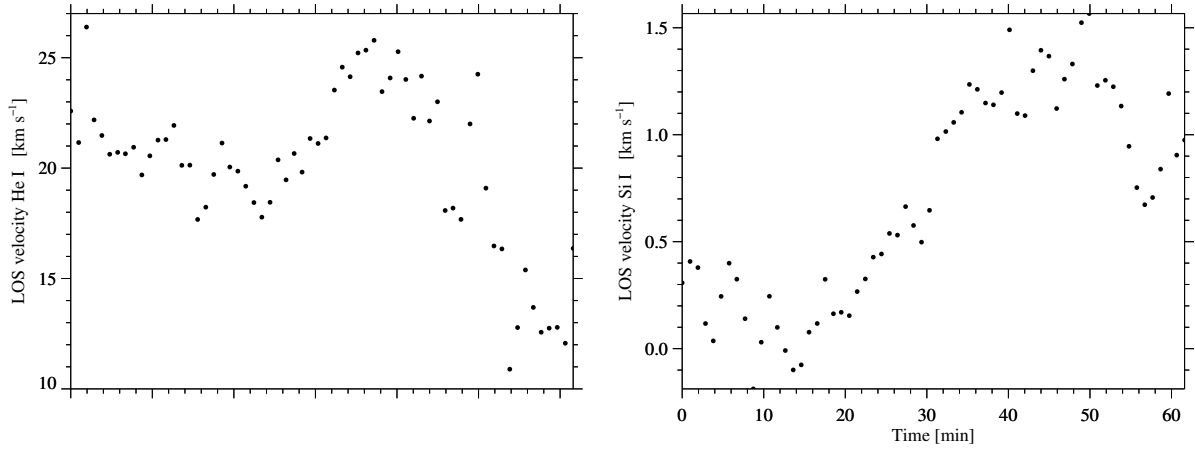


Figure 4.15: Mean He I (*top*) and Si I (*bottom*) velocities within the main footpoint near the right pore in Fig. 4.1. The region used to calculate the mean velocities is described in Chap. 4.4.3.

4.4.3 Height dependence

The time-series of GRIS data covers about one hour. Averaging various quantities over this time interval (see Fig. 4.16) reveals persistent chromospheric (top-left panel) and photospheric (bottom-left panels) downflows. The white contour in the top-left panel outlines the common FOV of all 64 maps in the time-series. Outside this region the averages are based on fewer values. A distinct kernel with downflows near pore P₂ is present in both maps of the photospheric Si I and the chromospheric He I LOS velocity. The kernel is marked by downward arrows in all panels. The maximum speed of the persistent chromospheric downflow is 13 km s^{-1} , which is supersonic in contrast to the 0.8 km s^{-1} measured in the upper photosphere. Other regions with high downflow velocities exist (marked by two parallel arrows in all panels), where the He I LOS mean velocities reach up to 10 km s^{-1} . The less pronounced appearance of these flow kernels suggests that the flows evolve on time-scales of less than one hour. These downflow kernels are in proximity to the footpoints of arch filaments, which terminate near pore P₂. The region between pores P₁ and P₂ is characterized by ongoing flux emergence of small-scale opposite-polarity magnetic features. The loop tops of the arch filaments have mean upflows up to 0.8 km s^{-1} in the chromosphere, clearly separating the footpoint regions with supersonic downflows in the He I LOS velocity map of Fig. 4.16. Note that all velocities mentioned in this paragraph are average velocities for the sum of all 64 velocity maps. The values for single maps can be significantly higher.

In Chap. 4.3.3, we described a method to automatically identify dual-flow profiles in the He I triplet as indicated by contours in Fig. 4.2. For each data set of the time-series we created a binary mask containing the locations of dual-flow profiles, which were added to obtain a map with their frequency of occurrence shown in the bottom-right panel of Fig. 4.16. Gray areas refer to regions, where dual-flow profiles are absent, and red colors indicate that more than 60 dual-flow profiles are present at the same location throughout the time-series. Dual-flow profiles are mainly associated with the AFS, and they are most common near the footpoints of arch filaments. However, at the location of pore P₁ they are almost absent, near the weak downflow kernels marked by parallel arrows they are encountered more frequently, and they are almost always present in proximity to pore P₂, which exhibits the strongest downflows. One of the regions with dual flow profiles has a circular shape, whereas the other one is elongated extending a distinct and persistent arch filament with strong He I absorption. The two-dimensional histogram of dual-flow profiles also provides guidance, where to find regions worthwhile for investigating temporal changes of flow speeds and spectral line shapes.

The mean LOS velocity maps only show persistent up- and downflows but they do not provide any clues about their dynamics, i.e., onset and cessation of up- or downflows – in principle periods with upflows could even be followed by periods with downflows and vice versa leading to an average velocity of zero. Single chromospheric LOS velocity maps display supersonic

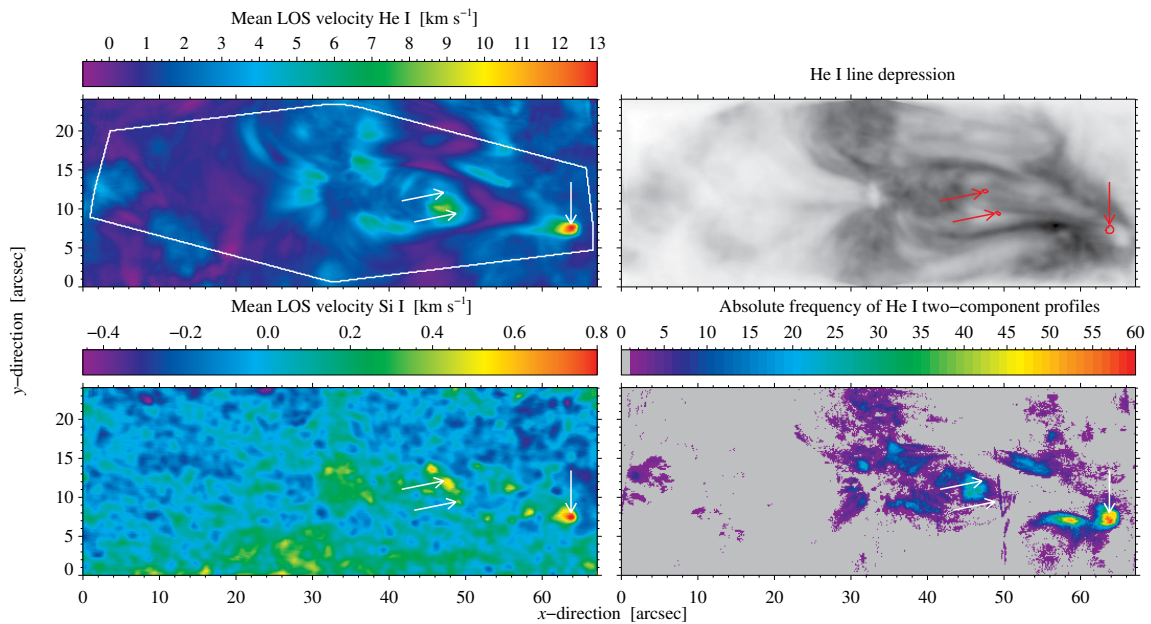


Figure 4.16: Average LOS velocities of all 64 GRIS maps for the chromosphere (*top-left*) and photosphere (*bottom-left*). A map with the frequency of occurrence of the dual-flow profiles is shown in the bottom-right panel. A mean map of the He I line depression is displayed in the top-right panel. The white contour in the top-left panel marks the common FOV of all 64 maps in the time-series. Kernels with persistent photospheric downflows are identified with arrows. The contours of these persistent flows are also plotted in red in the top-right panel.

downflows of up to 40 km s^{-1} at footpoints of arch filaments, and there is a tentative connection to photospheric downflows derived from the Si I line. To establish a more definitive link, we need to find a balance between persistent and dynamic flows. The evolution time-scale of photospheric features, e.g., granules, is generally a few minutes, sometimes up to 12 min near the pores (Darvann and Kusoffsky, 1989). In addition, solar p-modes can affect the LOS velocity measurements so that they have to be filtered. Ultimately, we created a set of 48 average flow maps with a sliding average, where each map is the mean of 16 consecutive Si I LOS velocity maps. The corresponding time interval of 16 min is three to four times longer than the mean lifetime of granules so that their intrinsic velocity pattern is smeared out and reduced. We obtained mean LOS velocity maps similar to the one in Fig. 4.16 for the Si I line. To select the velocity kernels, which we will track in time, we focused on regions with LOS velocities exceeding the mean LOS velocity \bar{v} by at least three times the standard deviation σ_v within the entire map, i.e., $\bar{v} + 3\sigma_v$.

Three regions exhibit mean velocities above the threshold mentioned above at some moments during the observations. Two small regions near the left footpoint are marked by two parallel arrows and with red contours in the map of the He I line depression (see Fig. 4.16). The downflow kernel belonging to the upper-left arrow shows elevated velocities in the first nine maps between 08:16:57 UT and 08:40:23 UT. The bottom-left arrow points to higher downflow velocities between 08:27:39 UT and 08:48:15 UT. The red contours encircle an area, where the downflows surpass the velocity threshold at least once in a single LOS velocity map comprising the 16-minute-average maps. The largest and strongest downflow kernel denoted by the right arrow is located near pore P₂. It is present throughout most of the time-series, i.e., between 08:40:23 UT and 09:18:33 UT. Applying the same technique to the LOS velocity maps of the Ca I 10839 Å line did not reveal any regions above the velocity threshold of $\bar{v} + 3\sigma$. The method for selecting flow kernels also provides the means to study the evolution of photospheric Si I and chromospheric He I LOS velocities and their correlation with time. Of particular interest is the strong downflow kernel near pore P₂. The contours referring to the velocity threshold were computed separately for each line and each map. Thus, the number of data points changes from map to map and is not the same for pairs of Si I and He I maps. The temporal evolution for both spectral lines is represented in Fig. 4.15. The chromospheric velocities within the

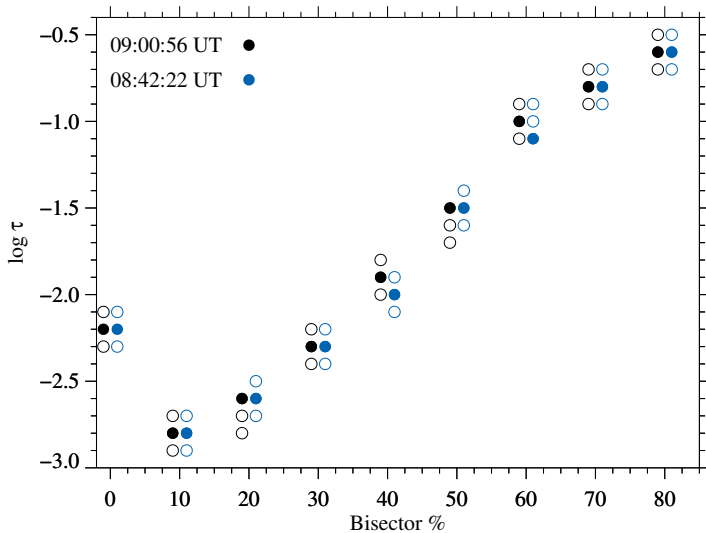


Figure 4.17: Comparison between Si I LOS velocity maps of the height-dependent bisectors method and SIR inversions. The study was carried out for the map shown in Fig. 4.2 (*black*) and another map taken at 08:42:22 UT (*blue*). The vertically aligned circles show the three highest correlations between both methods, and the filled circles indicates the highest correlation. The correlations were computed for the full FOV excluding the regions with pores, thus avoiding strong magnetic field concentrations.

downflow kernel are fairly constant for approximately the first 34 min of the time-series with a mean velocity around 20 km s^{-1} . Subsequently, the mean velocities rise up to 26 km s^{-1} within just 10 min, before declining to $11\text{--}12 \text{ km s}^{-1}$ over the remainder of the time-series. During the entire time-series the mean velocities were supersonic. The sound speed in the chromosphere is about 10 km s^{-1} . The temporal evolution of the photospheric mean LOS velocities follows a similar trend. The mean velocities in the first 34 min are in a range between -0.1 and $+0.6 \text{ km s}^{-1}$. However, the rise to higher mean velocities reaching up to 1.5 km s^{-1} starts already 15 min earlier than in the chromosphere. The maxima of chromospheric and photospheric LOS velocities coincide but the decline starts later in the photosphere by a few minutes. At the end of the time-series downflows are higher in the photosphere and lower in the chromosphere than in the beginning. The common trend of the temporal evolution of the velocities in the downflow kernel suggests a strong coupling between both atmospheric layers at the footpoint of the arch filament near pore P_2 .

The LOS velocities at the footpoint near pore P_2 show a maximum in Fig. 4.15 around $22\text{--}26 \text{ km s}^{-1}$ in the chromosphere and around $1.0\text{--}1.5 \text{ km s}^{-1}$ in the photosphere. In the following, we provide an approximation of the flux tube geometry for the arch filament and determine the height difference between chromospheric and photospheric flows. We assume that the plasma moves from the chromosphere to the photosphere along the flux tube. The cross-sectional area S of the tube is decreasing in the downward direction, and the plasma also gets denser.

The plasma motion is governed by equations of continuity, motion, and energy. The conservation of mass is given by the differential form of the continuity equation

$$\frac{\partial \rho}{\partial t} + \nabla(\rho v) = 0, \quad (4.1)$$

where ρ is the mass density and the Lagrangian derivative $d/dt \equiv \partial/\partial t + v \cdot \nabla$ was applied. If we also assume that the fluid is stationary $\partial\rho/\partial t = 0$, the the dynamic equilibrium is given by

$$\nabla(\rho v) = 0. \quad (4.2)$$

If in addition the fluid moves along the field lines, then the equation simplifies to

$$\rho v S = c_1, \quad (4.3)$$

where S is the area enclosing the field lines, and c_1 is a constant. Similarly, one of Maxwell's equations simplifies

$$\nabla B = 0, \quad (4.4)$$

where B is the magnetic field if the magnetic flux is conserved

$$BS = c_2, \quad (4.5)$$

where S is again the area enclosing the field lines and, c_2 is another constant. Dividing both Eqs. 4.3 and 4.5 yields

$$\frac{\rho v}{B} = c_3, \quad (4.6)$$

where $c_3 = c_1/c_2$ is a constant. The observations provide neither the density ρ nor the magnetic field B . Assuming that the density ρ is close to hydrostatic equilibrium and an isothermal atmosphere, we get an approximation for the density

$$\rho \sim e^{-z/H}, \quad (4.7)$$

where z is the distance between the footpoint in the chromosphere and the photosphere. The pressure scale-height H is derived from the ideal gas law $H = RT/\mu g$, where R is the ideal gas constant, μ is the mean molecular weight, g is the gravitational acceleration, and T refers to a constant temperature. Typically, the pressure scale-height H is 100–150 km in the photosphere (Priest, 2014).

In an isothermal atmosphere, the magnetic field B is given in the thin flux tube approximation as

$$B \sim e^{-z/2H}, \quad (4.8)$$

see Eqs. 4.7 and 4.8 in Spruit (1981). Substituting these equations into the Eq. 4.6 yields

$$v(z) \sim e^{z/2H}, \quad (4.9)$$

where $v(z) \sim v(z_1)/v(z_2)$, $v(z_1)$ is the mean LOS velocity measured at the footpoint in the photosphere, and $v(z_2)$ is the mean LOS velocity inferred at the footpoint in the chromosphere. Thus, $z = z_1 - z_2$ is the distance between the photospheric and the chromospheric footpoints. If we consider that $v(z_1) \sim 1.25 \text{ km s}^{-1}$, $v(z_2) \sim 24 \text{ km s}^{-1}$, and $H = 100\text{--}150 \text{ km}$, the distance between the photospheric and chromospheric cross-section of the flux tube, i.e., the footpoint of the arch filament, is $z \approx 600\text{--}900 \text{ km}$. Larger separations up to $z = 1100 \text{ km}$ are also plausible because some downflow velocities are weaker ($\sim 0.7 \text{ km s}^{-1}$) at the photosphere. Note that shock waves were not taken into account, which can be produced between photospheric and chromospheric layers (see Chap. 4.5).

Line-of-sight velocities based on the Ca II 8542 Å line

The height sensitivity of the Ca II line was studied by Quintero Noda *et al.* (2016) who used the NICOLE code studying the dependence of response functions to LOS velocity perturbations. They concluded that the line wings are sensitive to heights between $0 < \log \tau < -4$ and the line core to heights between $-4.5 < \log \tau < -5.5$. Hence, this line covers the photosphere as well as the middle chromosphere complementing the other lines involved in our study.

After a revision of the two-component inversions from NICOLE (see Chap. 4.3.6), we dropped 20% of the profiles because their fits were not satisfactory. The LOS velocities inferred from the remaining 80% (39 profiles) were averaged for each component in order to provide an overall estimate of the velocities inside the footpoint at a specific height. The decision of using two component inversions was supported by the fact that the two components show significantly different results. Moreover, the filling factor was close to 0.5 with a standard deviation of about 0.07, i.e., the weight of both atmospheric components within the resolution element is balanced.

For the first component, the highest velocities were found in the mid-chromosphere at an optical depth of $\log \tau \sim -4.9$ with a mean velocity of 2.7 km s^{-1} and a standard deviation of about 0.8 km s^{-1} . The velocities diminish with decreasing in height until they reach a mean velocity of 0.3 km s^{-1} with a standard deviation of 1.1 km s^{-1} at $\log \tau \sim 0$. This component coincides with the locations of the high redshifts found in the He I triplet. In contrast, the second component shows a larger dispersion in the LOS velocities and even oppositely directed flows, i.e., upflows of -1.3 km s^{-1} ($\sigma \sim 1.6 \text{ km s}^{-1}$) and -0.6 km s^{-1} ($\sigma \sim 0.6 \text{ km s}^{-1}$), at $\log \tau \sim -4.9$ and 0, respectively.

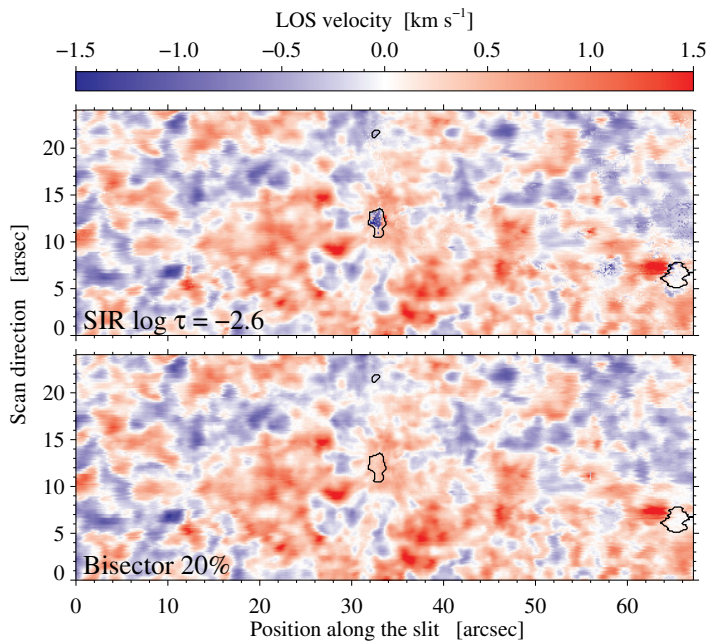


Figure 4.18: LOS velocity maps inferred from the Si I line using two different methods: SIR code (*top*) and bisectors (*bottom*). The maps refer to the same time and FOV as shown in Fig. 4.2. The highest linear correlation between both methods is 97.8% and corresponds to the bisector velocity at 20% and a $\log \tau = -2.6$ from SIR. The contours outline the pores in the continuum image ($\leq 0.89I_c$).

Comparison of bisectors with Stokes inversions based on response functions

The LOS velocities retrieved from the bisector method described in Chap. 4.3.4 were compared to the LOS velocities inferred from the height-dependent Stokes inversions based on SIR. As mentioned in Chap. 4.3.4, the height dependence in SIR is expressed in logarithmic optical depth units ($\log \tau$). This allows us to associate the bisectors for a specific line depths to a specific optical depth.

The comparison was performed for the map at 9:00:56 UT shown in Fig. 4.2 and another map taken earlier at 08:42:22 UT to confirm the results. The selected spectral line was the photospheric Si I line. We determined nine LOS velocity bisector maps in 10% steps of the line depth starting from the lower value at 10% and ending at the upper value of 80%. The extreme wings of the Si I line near the continuum are almost flat and contain small intensity perturbations producing large bisector shifts. Therefore, bisector maps close to the continuum are strongly affected by noise and are consequently discarded leading to our choice for the upper value. The LOS velocity map corresponding to the line core was calculated by a Gaussian fit (see Chap. 4.3.3).

The bisector and SIR velocity maps were compared using Pearson’s linear correlation coefficient. We excluded areas with strong magnetic field concentrations, i.e., where the Si I line exhibited Zeeman splitting, by creating a mask which eliminated the darkest pixels from the continuum image. Each of the LOS velocity bisector maps was compared and correlated with the 55 SIR LOS velocity maps. The height stratification of SIR covers the optical depth from $1.4 \geq \log \tau \geq -4.0$, in steps of 0.1 logarithmic units.

Figure 4.17 shows the results of this correlation analysis for both maps. The vertically aligned circles represent the three SIR velocity maps with the highest correlation for each bisector map at a given line depth, while the filled circle marks the highest correlation. The blue circles indicate the results from the map at 08:42:22 UT and the black circles those at 9:00:56 UT. The black and blue circles are slightly shifted to the left and right along the x -axis for clarity. Henceforth, we only refer to the map at 9:00:56 UT because the results of the other maps are very similar. High linear correlations in the range of 95–98% (see Tab. 4.1) are found for all values depicted in Fig. 4.17. As expected, bisector velocities obtained deeper in the line correspond to lower optical depth. As an example, the bisector at 10% above the line core shows correlations of 97.8%, 97.7%, and 97.3% with SIR maps at $\log \tau = [-2.6, -2.7, -2.8]$, respectively. The circle at 10% in Fig. 4.17 deviates from a linear relationship mainly because of the departure from local thermodynamic equilibrium (LTE) at the Si I line core. However, the SIR code assumes LTE conditions. Hence, in layers, where $\log \tau < -3$, the inferred velocities are not reliable.

Table 4.1: Linear correlation between velocity maps derived with the bisector method and with SIR inversions.

Bisector [%]	$\log \tau$	Correlation [%]
10	-2.8	97.2
20	-2.6	97.8
30	-2.3	97.8
40	-1.9	97.2
50	-1.5	96.7
60	-1.0	97.0
70	-0.8	96.9
80	-0.6	95.1

The two LOS velocity maps for which the best correlation was achieved (97.8%) are shown in Fig. 4.18. The top panel shows the results from the SIR inversions at $\log \tau = -2.6$ while the bottom panel depicts the results from the bisector method at 20%. Visually, both maps are very similar except in the area of the pores (inside the black contours). However, these areas were not included when computing the correlation between the bisector and SIR velocities.

4.5 Discussions and conclusions

The primary goal of this study is to link supersonic chromospheric downflows in the footpoints of the AFS with downflows observed in the photosphere. In particular, we want to answer the question if it is possible that plasma motions in photospheric layers are fed by supersonic chromospheric downflows – a question raised in previous studies that made an effort to connect both atmospheric layers of the Sun, for example, by [Lagg *et al.* \(2007\)](#) whose observations resemble ours. The magnetic field information is obviously missing in very fast spectroscopic mode but can be provided in the future with polarimetric GFPI observations (e.g., [Balthasar *et al.*, 2011](#)). The observed He I supersonic downflows (up to 40 km s^{-1}) at the footpoints of arch filaments near a pores of the EFR are in very good agreement with previous observations, for example, by [Schmidt, Muglach, and Knölker \(2000\)](#), [Lagg *et al.* \(2007\)](#), and [Xu, Lagg, and Solanki \(2010\)](#).

[Uitenbroek, Balasubramaniam, and Tritschler \(2006\)](#) observed supersonic downflows near the edge of a single solar pore in the chromospheric Ca II 8542 Å NIR line. In this study, we did not find supersonic velocities in the chromospheric Ca II 8542 Å line (see Chap. 4.4.3). The first component of the two-component inversions shows the highest velocity of 2.7 km s^{-1} in the mid-chromosphere with $\log \tau \sim -4.9$, and the velocity is decreasing towards the photosphere reaching velocities close to 0.3 km s^{-1} at $\log \tau \sim 0$. This component is consistent with the high downflows found in the He I triplet. The second component exhibits small upflow velocities of -1.3 km s^{-1} and -0.6 km s^{-1} at $\log \tau \sim -4.9$ and 0, respectively. This second component is also consistent with the small upflow velocities observed in the photospheric Si I line. Clearly, in this region at coordinates ($30''$, $23''$) in Fig. 4.4 and ($46''$, $11''$) in Fig. 4.18 the plasma does not reach the photosphere. Chromospheric upflows velocities inferred with the He I are also found at the loop tops with velocities up to 5 km s^{-1} , which is in agreement with other studies, for example, by [Solanki \(2003\)](#) who observed upflows up to 4 km s^{-1} or by [Spadaro *et al.* \(2004\)](#) who observed upflow velocities between $3\text{--}9 \text{ km s}^{-1}$.

Small photospheric velocities were observed by [Hirzberger \(2003\)](#) with the Göttingen FPI, but next to pores he detected downflow channels with velocities between 0.4 and 1.4 km s^{-1} . A downflow in pores was also seen by [Giordano *et al.* \(2008\)](#) with velocities of 0.2 km s^{-1} surrounded by ring-like downflows of 0.3 km s^{-1} . [Xu, Lagg, and Solanki \(2010\)](#) observed photospheric downflows up to 1.5 km s^{-1} cospatial with supersonic chromospheric downflows. [Lagg *et al.* \(2007\)](#) also inferred photospheric LOS velocities of a few 100 m s^{-1} based on the Si I line at the location of the chromospheric supersonic downflows. Initially, they measured photospheric

downflows of around 0.6 km s^{-1} , which increased to around 1.3 km s^{-1} at the end of their 73-minute time-series. These flow speeds are similar to the values presented in Fig. 4.15. However, the photospheric downflows were not attributed to the chromospheric supersonic downflows. Establishing this link is challenging as also stated by [Schad, Penn, and Lin \(2013\)](#) who observed a bipolar active region. Their observations were hampered by poor temporal resolution so that flows along the filament fibrils could not be tracked reliably. Tracking the temporal evolution of AFS loops with a lifetime of about 30 min ([Bruzek, 1969](#)) requires the very fast spectroscopic mode of GRIS, which offers a one-minute cadence and covers a significant part of the EFR/AFS (see Chap. 4.4.2).

Regarding the horizontal proper motions in the photosphere, the most striking horizontal flow feature are inflows around newly formed pores. [Wang and Zirin \(1992\)](#) noticed these inflows associated with pore and concluded that the pores are formed by the concentration of already existing magnetic field. However, [Hirzberger \(2003\)](#) in their LCT study did not confirm inflows in pores. In a detailed statistical study based on Hinode G-band images [Verma and Denker \(2014\)](#) found converging flows towards the center of pores. Recently, [Li, Yang, and Zhang \(2015\)](#) noticed inflows of moving magnetic features during the pore's growth phase. In the present case study we also see clear indications of inflows in the time-averaged LCT map. The average horizontal velocities presented here are in agreement with values computed by [Verma and Denker \(2011, 2012\)](#). Taken together with the photospheric and chromospheric LOS velocities, we conclude that plasma is moving vertically downwards along the arch filament and horizontally from the photosphere towards the pore, i.e., the footpoint of the filament. Another prominent horizontal flow feature of EFRs are large, elongated, and expanding granules (e.g., [Rezaei, Bello González, and Schlichenmaier, 2012](#); [Guglielmino et al., 2010](#)), which are also present in the surroundings of our EFR but not directly between two pores (cf., [Verma et al., 2016](#)). Nevertheless, the presence of these granules near the pores is a clear indication of ongoing flux emergence.

Several physical processes have been proposed to explain downflows along the magnetic field lines. The physical properties of the EFR are summarized by [Chou \(1993\)](#). [Lagg et al. \(2007\)](#) suggested that strong downflows can be explained by a flux tube. This flux tube is emptied as a consequence of the pressure balance between the flux tube that it is rising from the photosphere and the neighboring atmosphere. As a consequence, the hydrostatic support is lost and the material moves downwards to the solar surface. In the present study, our observations agree with the findings of [Lagg et al. \(2007\)](#) where the upflows are placed on the loop tops and the downflows are along the legs of the arch filaments. Another concept to explain the appearance of the photospheric footpoints of the flux tubes is convective collapse (e.g., [Spruit, 1979](#); [Parker, 1978](#); [Grossmann-Doerth, Schüssler, and Steiner, 1998](#); [Lagg et al., 2007](#)), which also offers an explanation for the converging horizontal proper motions around pores measured with LCT.

In this study, we found a clear connection between the chromospheric supersonic and photospheric velocities thanks to the very fast spectroscopic mode of GRIS, which offered the required cadence to track the velocities in both the chromosphere and the photosphere. The highest mean chromospheric LOS velocities were up to 26 km s^{-1} near the pore P₂, while the highest mean photospheric velocities approached 1.5 km s^{-1} (see Fig. 4.15). The analogue temporal evolution of the photospheric and chromospheric footpoint velocities presented in Fig. 4.15 confirms this link.

The height distance between the footpoint at the chromosphere and the photosphere near pore P₂ was estimated in Chap. 4.4.3 reaching values up to 1100 km. The He I triplet is formed under non-LTE conditions in the chromosphere with a height exceeding 1500 km (e.g., [Lagg et al., 2004](#)). Our assumptions did not take into account shock waves that can be produced in the chromosphere. The supersonic chromospheric downflows and the subsonic downflows in the photosphere suggest shocks between both layers. [Lagg et al. \(2004\)](#) proposed the 'uncombed model' with the field lines of the fast component being more horizontal than the field lines of the slow component. These components are generated in a single chromospheric layer, where the shocks originate. The other proposed model is the 'cloud model', where the fast component lies above the slow component, and the shock is produced between these two components. If these

models are correct, our assumptions made to calculate the distance between the photosphere and the chromosphere may not be valid. However, the results of [Xu, Lagg, and Solanki \(2010\)](#) do not reveal any sign of He I emission suggesting that the shock is constrained to layers below the formation height of the He I line.

In this study we also conclude that the bisectors method is suitable to infer LOS velocities from the Si I line at different heights. In addition, using the SIR code, we have associated the bisectors for a specific line depth to a specific optical depth of the atmosphere. We have demonstrated this with the data shown in [Fig. 4.4](#) and achieved correlation values above 95% between the bisector maps and the inferred SIR maps. The advantage of using the bisector method instead of the SIR code is the much faster computing time. The velocity maps from all 64 maps were computed in just one hour.

Chapter 5

Conclusions and outlook

In Chap. 1 of this thesis we introduced many physical properties of the EFR and its accompanying AFR in the chromosphere. We raised several questions that we were able to answer based on observations, analysis, and discussion of two small bipolar EFRs investigated in this thesis: (1) uni-polar micro-pores and (2) two small pores with opposite polarities.

Generally, photospheric and chromospheric structures like pores or sunspots cover a wide range of spatial scales. Pores can vanish after a few days like those of the EFRs discussed in this doctoral thesis or grow into sunspots and potentially assemble into complex active regions. In the chromosphere many structures can be observed with different sizes. The cool plasma is suspended by the magnetic field forming structures from mini-filaments (a few megameters) to giant filaments (several hundred megameters). The properties of the chromosphere and photosphere are important to understand EFRs with AFSs. To explore the smaller spatial scales requires large-aperture solar telescopes and dedicated instruments to observe magnetic features in multiple wavelengths. As a consequence the observed FOV is small, and time-series cover only a couple of hours at most. Synoptic observations are often impracticable due to the small spatial scales. Hence, only a small number of studies are available to increase our knowledge about EFRs and AFSs at sub-arcsecond scales.

Several techniques were applied in this thesis to infer different physical parameters, e.g., SIR and NICOLE inversions using various spectral lines, cloud model inversions, inferring the LOS velocity using the center-of-gravity method, developing a new and rapid technique for determining the velocity of multiple atmospheric components within a single spatial pixel using the He I triplet, and some other techniques.

The CM inverted parameters offer the opportunity to distinguish between features with higher contrasts belonging to the AFS and other regions of the quiet-Sun or the interface between the quiet Sun and the AFS. The method used to obtain the LOS velocity of the He I red component produced good fits and reasonable chromospheric velocities, which agree well with similar investigations of EFRs. This method assumes that the He I triplet is always optically thin in the wavelength range of the telluric line, an assumption that should be tested in the future. Improve the method to fit the red components of the He I triplet is also required because in some cases not only two components but three and even four components were visible. This technique should include multiple component fitting because this type of spectral profiles appears more frequently in active regions, which exhibit often higher velocities than in our observations (e.g., [Aznar Cuadrado, Solanki, and Lagg, 2005, 2007](#)).

In this doctoral thesis, we used the Göttingen FPI to analyze a very small EFR with micro-pores and its accompanying AFS, and the GFPI, GRIS, and CRISP to investigate a small EFR also with an AFS. In both observing campaigns the AFS connects the two opposite polarities: in one case coupling two main pores and in the other case connecting micro-pores to a quiet-Sun region of opposite polarity. In both cases the small-scale arch filaments are perpendicular to the PIL. These arch filaments are a clear indication of a newly emerging flux in the form of Ω -loops. In the case of the small EFR with micro-pores the magnetograms show that the trailing polarity is formed earlier, while in the EFR containing two pores the leading polarity

is formed earlier. In the first case the observations were taken during the declining phase of the 23rd solar cycle (southern hemisphere) with the leading part possessing polarity negative. In the second case, the observations were just after the maximum of the 24th solar cycle (also southern hemisphere) with the leading polarity being positive. Thus, the Hale-Nicholson law applies to both EFRs. The leading polarity containing the micro-pores is more compact and survives longer, while in the second case the leading pore of the EFR vanished first, and the magnetic field is more fragmented. In both cases the negative polarity survived longer, and the magnetic field is more compact. These asymmetries are typical properties of EFRs, even for larger ones (van Driel-Gesztelyi and Petrovay, 1990). In both cases flux cancellation is the likely cause of the EFR's decay. The flux fragmentation suggest that several Ω -loops are connecting the opposite polarities. Thus, several dark arch filaments comprise the AFS.

A statistical description was presented for both observations but the description of micro-pores and of flux emergence at very small spatial scales (below 1 Mm) remains challenging. In the case of the micro-pores the study focused on the temporal evolution of their area, their mean intensity, and the separation of footpoints. In the case of the two pores, the center-to-center distance evolution was also followed in time. All of these properties match with previous observations and simulations describing EFRs and AFSs on similar spatial scales.

The two observed EFRs show very much the same behaviour as those of previous observations and simulations. In the AFS upflows are commonly observed at the loop tops, and the cool plasma drains towards the footpoints along the flux tube connecting the opposite polarities. The LOS velocities of the EFR with the two pores exhibits velocities up to 5 km s^{-1} matching the maximum velocities obtained in other observations, while the LOS velocities inferred for the EFR with the micro-pores are much lower. LOS velocities were also inferred along the loops in both data sets. Generally, the LOS velocities are higher near the footpoints of the arch filaments reaching in many cases supersonic speeds. In the case of the micro-pores the LOS velocities in the loops are lower, i.e., two to four times lower than for larger AFSs. It was also possible to track the temporal evolution of the LOS velocities along the loops of the arch filaments. The plasma rises with the ascend of the flux tube leading to upflows at the loop tops. Afterwards the plasma contained in the flux tube drains towards the footpoints connecting the two polarities. These dynamics enabled us to calculate the lifetime of single arch filaments (around 30 min) confirming results of previous studies. The buoyancy and the curvature of the rising/submerging Ω -loops are the determining factor for the observed up- and downflows. Nonetheless, a better statistical sample is needed to derive scaling laws. The sizes of the pores can vary from sub-arcsecond to about ten arcseconds. Therefore, comparing a larger sample of EFRs and AFSs in a similar spatial domain with simulations of flux emergence and decay will be very beneficial for our understanding of the dynamic interaction of magnetic fields with the surrounding plasma.

In order to track the dynamics of the EFR (containing the two pores) along several heights within the chromosphere and the photosphere, a multi-wavelength study was carried out with the very fast spectroscopic mode of GRIS, which offered a good time resolution to track the velocities. The link between the chromospheric filamentary structures and the photosphere has been an open question but in this study we demonstrated that the plasma of chromospheric structures, which exhibit supersonic LOS downflows near the footpoints, reached the photosphere. Several physical processes have been proposed to explain downflows along magnetic flux tubes. One of the concepts explains photospheric footpoints of flux tubes as a result of convective collapse (e.g., Spruit, 1979; Parker, 1978; Grossmann-Doerth, Schüssler, and Steiner, 1998). Lagg *et al.* (2007) suggested that the supersonic downflows can be explained by a flux tube emptied as a consequence of the pressure balance between the flux tube and the surrounding atmosphere.

The approximated distance between chromospheric and photospheric footpoints was calculated using the velocities obtained in both layers of the solar atmosphere. The distance obtained between the two atmospheric layers is up to 1100 km, which is a very good match to other theories and simulations. Several assumptions were made to obtain this distance, e.g., the fluid is stationary, the magnetic flux is conserved, the flux tube is in hydrostatic equilibrium, the thin-flux-tube approximation applies, the atmosphere is isothermal, etc. In addition, shocks were not

taken into account, which can be produced between the chromosphere and the photosphere. It is still not clear at which heights these shocks are potentially formed. Some studies proposed that the emission associated with the shocks are produced at the formation height of the He I triplet. Other studies did not find signs of He I emission because of shocks at this height and they proposed that the shocks could be produced below this height so that some questions arise: At which height are the shocks formed? Are they produced even below the formation height of the Si I line, i.e., the upper photosphere?

Regarding the horizontal flows in the photosphere, LCT results indicate that the flow speeds in both studies reflect motions of individual granules, expanding granules, and small-scale brightenings. In the case of the micro-pores the reduced flow speed in the immediate surroundings of the micro-pores suggests that the magnetic field is already strong enough to affect the convective motions. In the case of the two pores we detected clear indications of inflows in pore P₁, which is in agreement with other studies. These converging horizontal proper motions also fit the scenario of convective collapse at the footpoints of arch filaments. All LCT results are a clear indication of ongoing flux emergence.

Another important conclusion of this thesis is that the bisector method can be used to rapidly infer LOS velocities from the Si I line at different heights. Additionally, comparing these bisector maps and the LOS velocities inferred with the SIR code, we associated the bisector maps at a certain line depth to a specific optical depth in the atmosphere.

Future observations and studies should aim at a better understanding of the physical properties of EFRs and AFSs. However, more detailed magnetic field information is obviously needed. First steps to overcome this deficiency were already taken in a similar study of an AFS using the GRIS spectropolarimetric mode (Balthasar *et al.*, 2016). The results of this doctoral thesis, including methods and techniques, are already being used in forthcoming studies of EFRs and active regions. High-resolution imaging spectropolarimetry was so far limited to CRISP but after refurbishing the GFPI polarimeter supplementary information about the photospheric and chromospheric magnetic fields will become available in the 2017 observing season. Observing a meaningful sample of EFRs at various heliocentric angles are needed to confirm some theoretical models, e.g., the uncombed model proposed by (Lagg *et al.*, 2007).

This study focused on photospheric and chromospheric properties and dynamics of EFRs and AFSs. However, the response to emerging flux of the upper atmosphere, i.e., the transition region and corona, is also a worthwhile endeavor offering challenges and posing questions: Are arch filament loops also seen in the corona and can the rise of Ω loops be tracked from the photosphere to the upper atmosphere? Do shocks leave a signature in the AIA UV continua? Conveniently, the space mission SDO facilitates studying the evolution of the loops in the transition region and corona with good spatial and excellent temporal resolution. Complementary spectroscopic information in the UV can be obtained in coordinated observing campaigns with Interface Region Imaging Spectrograph (IRIS, de Pontieu *et al.*, 2014) from space.

Multi-wavelength and multi-instrument observations were the basis of this doctoral thesis. We have demonstrated that high-resolution observations obtained with the VTT, the GREGOR solar telescope, and the SST provide new insights into the dynamic interaction of plasma and magnetic fields. However, the synergies between imaging and NIR long-slit spectropolarimetry have not yet been fully exploited. At the GREGOR solar telescope, GRIS, GFPI, and fast imagers for image restorations can nowadays be used to study the fine structure of the Sun. Powerful data pipelines significantly shorten the time between observations and scientific analysis and ultimately dissemination in peer-reviewed journals and conferences. Therefore, the work contained in this doctoral thesis is only a first stepping stone towards a better understanding of EFRs and AFSs in particular and flux emergence and decay in general.

Bibliography

- Abbett, W.P.: 2007, The Magnetic Connection between the Convection Zone and Corona in the Quiet Sun. *Astrophys. J.* **665**, 1469. doi:[10.1086/519788](https://doi.org/10.1086/519788).
- Abbett, W.P., Fisher, G.H.: 2010, Improving Large-Scale Convection-Zone-to-Corona Models. *Mem. Soc. Astron. Ital.* **81**, 721.
- Al, N., Bendlin, C., Hirzberger, J., Kneer, F., Trujillo Bueno, J.: 2004, Dynamics of an Enhanced Network Region Observed in H α . *Astron. Astrophys.* **418**, 1131. doi:[10.1051/0004-6361:20034501](https://doi.org/10.1051/0004-6361:20034501).
- Allisandrakis, C.E., Tsiropoula, G., Mein, P.: 1990, Physical Parameters of Solar H α Absorption Features Derived with the Cloud Model. *Astron. Astrophys.* **230**, 200.
- Allende Prieto, C., Asplund, M., Fabiani Bendicho, P.: 2004, Center-to-Limb Variation of Solar Line Profiles as a Test of NLTE Line Formation Calculations. *Astron. Astrophys.* **423**, 1109. doi:[10.1051/0004-6361:20047050](https://doi.org/10.1051/0004-6361:20047050).
- Andersen, T., Engvold, O., Owner-Pedersen, M.: 2002, Technology Demonstration Solar Telescope. Technical Report.
- Archontis, V.: 2012, Magnetic Flux Emergence and Associated Dynamic Phenomena in the Sun. *Phil. Trans. Roy. Soc. London Ser. A* **370**, 3088. doi:[10.1098/rsta.2012.0001](https://doi.org/10.1098/rsta.2012.0001).
- Asensio Ramos, A., Trujillo Bueno, J., Landi Degl'Innocenti, E.: 2008, Advanced Forward Modeling and Inversion of Stokes Profiles Resulting from the Joint Action of the Hanle and Zeeman Effects. *Astrophys. J.* **683**, 542. doi:[10.1086/589433](https://doi.org/10.1086/589433).
- Avrett, E.H., Fontenla, J.M., Loeser, R.: 1994, Formation of the Solar 10830 Angstrom Line. In: Rabin, D.M., Jefferies, J.T., Lindsey, C. (eds.) *Infrared Solar Physics, IAU Symp.* **154**, 35.
- Aznar Cuadrado, R., Solanki, S.K., Lagg, A.: 2005, Supersonic Downflows in the Solar Chromosphere are very Common. In: Innes, D.E., Lagg, A., Solanki, S.K. (eds.) *Chromospheric and Coronal Magnetic Fields, ESA Spec. Publ.* **596**, 49–1.
- Aznar Cuadrado, R., Solanki, S.K., Lagg, A.: 2007, Velocity Distribution of Chromospheric Downflows. In: Kneer, F., Puschmann, K.G., Wittmann, A.D. (eds.) *Modern Solar Facilities – Advanced Solar Science*, Universitätsverlag Göttingen, Göttingen, Germany, 173.
- Babcock, H.W., Babcock, H.D.: 1955, The Sun's Magnetic Field, 1952-1954. *Astrophys. J.* **121**, 349. doi:[10.1086/145994](https://doi.org/10.1086/145994).
- Balthasar, H., Bello González, N., Collados, M., Denker, C., Feller, A., Hofmann, A., Lagg, A., Nagaraju, L., Puschmann, K.G., Soltau, D., Volkmer, R.: 2011, Polarimetry with GREGOR. In: Kuhn, J.R., Harrington, D.M., Lin, H., Berdyugina, S.V., Trujillo-Bueno, J., Keil, S.L., Rimmele, T. (eds.) *Solar Polarization 6, ASP Conf. Ser.* **437**, 351.

- Balthasar, H., Gömöry, P., González Manrique, S.J., Kuckein, C., Kavka, J., Kučera, A., Schwartz, P., Vašková, R., Berkefeld, T., Collados Vera, M., Denker, C., Feller, A., Hofmann, A., Lagg, A., Nicklas, H., Orozco Suárez, D., Pastor Yabar, A., Rezaei, R., Schlichenmaier, R., Schmidt, D., Schmidt, W., Sigwarth, M., Sobotka, M., Solanki, S.K., Soltau, D., Staude, J., Strassmeier, K.G., Volkmer, R., von der Lühe, O., Waldmann, T.: 2016, Spectropolarimetric Observations of an Arch Filament system with the GREGOR Solar Telescope. *Astron. Nachr.* **337**, 1050. doi:[10.1002/asna.201612432](https://doi.org/10.1002/asna.201612432).
- Barthol, P., Chares, B., Deutsch, W., Feller, A., Gandorfer, A., Grauf, B., Hirzberger, J., Meller, R., Riethmüller, T., Schüssler, M., Solanki, S.K., Knölker, M., Martinez Pillet, V., Schmidt, W., Title, A.: 2010, High Resolution Imaging and Polarimetry with SUNRISE, a Balloon-Borne Stratospheric Solar Observatory. In: *38th COSPAR Scientific Assembly, COSPAR Meeting 38*, 16.
- Beckers, J.M.: 1964, A Study of the Fine Structures in the Solar Chromosphere. PhD Thesis, University of Utrecht.
- Beckers, J.M.: 1972, Solar Spicules. *Ann. Rev. Astron. Astrophys.* **10**, 73.
- Beeck, B., Schüssler, M., Cameron, R.H., Reiners, A.: 2015, Three-Dimensional Simulations of Near-Surface Convection in Main-Sequence Stars. III. The Structure of Small-Scale Magnetic Flux Concentrations. *Astron. Astrophys.* **581**, A42. doi:[10.1051/0004-6361/201525788](https://doi.org/10.1051/0004-6361/201525788).
- Bello González, N., Kneer, F.: 2008, Narrow-Band Full Stokes Polarimetry of Small Structures on the Sun with Speckle Methods. *Astron. Astrophys.* **480**, 265. doi:[10.1051/0004-6361:20078567](https://doi.org/10.1051/0004-6361:20078567).
- Bendlin, C., Volkmer, R., Kneer, F.: 1992, A New Instrument for High Resolution, Two-Dimensional Solar Spectroscopy. *Astron. Astrophys.* **257**, 817.
- Bentley, R.D., Freeland, S.L.: 1998, SOLARSOFT – An Analysis Environment for Solar Physics. In: *Crossroads for European Solar and Heliospheric Physics. Recent Achievements and Future Mission Possibilities, ESA Spec. Publ.* **417**, 225.
- Berkefeld, T., Schmidt, D., Soltau, D., von der Lühe, O., Heidecke, F.: 2012, The GREGOR Adaptive Optics System. *Astron. Nachr.* **333**, 863. doi:[10.1002/asna.201211739](https://doi.org/10.1002/asna.201211739).
- Berkefeld, T., Soltau, D., Schmidt, D., von der Lühe, O.: 2010, Adaptive Optics Development at the German Solar Telescopes. *Appl. Opt.* **49**, G155. doi:[10.1364/AO.49.00G155](https://doi.org/10.1364/AO.49.00G155).
- Bommier, V., Rayrole, J., Eff-Darwich, A.: 2005, Vector Magnetic Field Map at the Photospheric Level below and around a Solar Filament (Neutral Line). *Astron. Astrophys.* **435**, 1115. doi:[10.1051/0004-6361:20042509](https://doi.org/10.1051/0004-6361:20042509).
- Bonet, J.A., Sobotka, M., Vazquez, M.: 1995, Photometry of Sunspot Pores from Partial Eclipse Observations. *Astron. Astrophys.* **296**, 241.
- Borrero, J.M., Ichimoto, K.: 2011, Magnetic Structure of Sunspots. *Living Rev. Solar Phys.* **8**. doi:[10.12942/lrsp-2011-4](https://doi.org/10.12942/lrsp-2011-4).
- Bostanci, Z.F.: 2011, Cloud Modeling of a Network Region in H α . *Astron. Nachr.* **332**, 815.
- Bostanci, Z.F., Erdogan, N.A.: 2010, Cloud Modeling of a Quiet Solar Region in H α . *Mem. Soc. Astron. Ital.* **81**, 769.
- Brandt, P.N., Wöhl, H.: 1982, Solar Site-Testing Campaign of JOSO on the Canary Islands in 1979. *Astron. Astrophys.* **109**, 77.
- Brants, J.J., Steenbeek, J.C.M.: 1985, Morphological Evolution of an Emerging Flux Region. *Solar Phys.* **96**, 229. doi:[10.1007/BF00149682](https://doi.org/10.1007/BF00149682).

- Brault, J.W., Neckel, H.: 1987, Spectral Atlas of Solar Absolute Disk-Averaged and Disk-Center Intensity from 3290 to 12510 Å (available at [hs.uni-hamburg.de/pub/outgoing/FTS-Atlas](https://www.hs.uni-hamburg.de/pub/outgoing/FTS-Atlas)).
- Bruzek, A.: 1967, On Arch-Filament Systems in Spotgroups. *Solar Phys.* **2**, 451. doi:[10.1007/BF00146493](https://doi.org/10.1007/BF00146493).
- Bruzek, A.: 1969, Motions in Arch Filament Systems. *Solar Phys.* **8**, 29. doi:[10.1007/BF00150655](https://doi.org/10.1007/BF00150655).
- Cameron, R., Schüssler, M., Vögler, A., Zakharov, V.: 2007, Radiative Magnetohydrodynamic Simulations of Solar Pores. *Astron. Astrophys.* **474**, 261.
- Carlsson, M., Stein, R.F., Nordlund, Å., Scharmer, G.B.: 2004, Observational Manifestations of Solar Magnetoconvection: Center-to-Limb Variation. *Astrophys. J. Lett.* **610**, L137. doi:[10.1086/423305](https://doi.org/10.1086/423305).
- Carrington, R.C.: 1858, On the Distribution of the Solar Spots in Latitudes since the Beginning of the Year 1854, with a Map. *Mon. Not. R. Astron. Soc.* **19**, 1. doi:[10.1093/mnras/19.1.1](https://doi.org/10.1093/mnras/19.1.1).
- Cavallini, F.: 2006, IBIS: A New Post-Focus Instrument for Solar Imaging Spectroscopy. *Solar Phys.* **236**, 415.
- Chae, J.: 2014, Spectral Inversion of the H α Line for a Plasma Feature in the Upper Chromosphere of the Quiet Sun. *Astrophys. J.* **780**, 109. doi:[10.1088/0004-637X/780/1/109](https://doi.org/10.1088/0004-637X/780/1/109).
- Cheung, M.C.M., Isobe, H.: 2014, Flux Emergence (Theory). *Living Rev. Solar Phys.* **11**. doi:[10.12942/lrsp-2014-3](https://doi.org/10.12942/lrsp-2014-3).
- Cheung, M.C.M., Schüssler, M., Moreno-Insertis, F.: 2007, Magnetic Flux Emergence in Granular Convection: Radiative MHD Simulations and Observational Signatures. *Astron. Astrophys.* **467**, 703. doi:[10.1051/0004-6361:20077048](https://doi.org/10.1051/0004-6361:20077048).
- Cheung, M.C.M., Schüssler, M., Tarbell, T.D., Title, A.M.: 2008, Solar Surface Emerging Flux Regions: A Comparative Study of Radiative MHD Modeling and Hinode SOT Observations. *Astrophys. J.* **687**, 1373. doi:[10.1086/591245](https://doi.org/10.1086/591245).
- Cheung, M.C.M., Rempel, M., Title, A.M., Schüssler, M.: 2010, Simulation of the Formation of a Solar Active Region. *Astrophys. J.* **720**, 233. doi:[10.1088/0004-637X/720/1/233](https://doi.org/10.1088/0004-637X/720/1/233).
- Chou, D.Y.: 1993, Structure of Emerging Flux Regions. In: Zirin, H., Ai, G., Wang, H. (eds.) *IAU Colloq. 141: The Magnetic and Velocity Fields of Solar Active Regions, ASP Conf. Ser.* **46**, 471–478.
- Chou, D.Y., Zirin, H.: 1988, The Vertical Structure of Arch Filament Systems in Solar Emerging Flux Regions. *Astrophys. J.* **333**, 420. doi:[10.1086/166757](https://doi.org/10.1086/166757).
- Choudhuri, A.R.: 1986, The Dynamics of Magnetically Trapped Fluids. I. Implications for Umbral Dots and Penumbra Grains. *Astrophys. J.* **302**, 809. doi:[10.1086/164042](https://doi.org/10.1086/164042).
- Collados, M., Lagg, A., Díaz García, J.J., Hernández Suárez, E., López López, R., Páez Mañá, E., Solanki, S.K.: 2007, Tenerife Infrared Polarimeter II. In: Heinzel, P., Dorotovič, I., & Rutten, R.J. (eds.) *The Physics of Chromospheric Plasmas, ASP Conf. Ser.* **368**, 611.
- Collados, M., Calcines, A., Díaz, J.J., Hernández, E., López, R., Páez, E.: 2008, A High-Resolution Spectrograph for the Solar Telescope GREGOR. In: McLean, I.S., Casali, M.M. (eds.) *Ground-Based and Airborne Instrumentation for Astronomy II, Proc. SPIE* **7014**, 70145Z.

- Collados, M., López, R., Páez, E., Hernández, E., Reyes, M., Calcines, A., Ballesteros, E., Díaz, J.J., Denker, C., Lagg, A., Schlichenmaier, R., Schmidt, W., Solanki, S.K., Strassmeier, K.G., von der Lühe, O., Volkmer, R.: 2012, GRIS: The GREGOR Infrared Spectrograph. *Astron. Nachr.* **333**, 872. doi:[10.1002/asna.201211738](https://doi.org/10.1002/asna.201211738).
- Contarino, L., Zuccarello, F., Romano, P., Spadaro, D., Ermolli, I.: 2009, Morphological and Dynamical Properties of Small-Scale Chromospheric Features Deduced from IBIS Observations. *Astron. Astrophys.* **507**, 1625.
- Darvann, T.A., Kusoffsky, U.: 1989, Granule Lifetimes and Dimensions as Function of Distance from a Solar Pore Region. In: Rutten, R.J., Severino, G. (eds.) *Solar and Stellar Granulation, NATO ASI Series C* **263**, 313.
- de Boer, C.R., Kneer, F.: 1992, Speckle Observations of Abnormal Solar Granulation. *Astron. Astrophys.* **264**, L24.
- de la Cruz Rodríguez, J., Rouppe van der Voort, L., Socas-Navarro, H., van Noort, M.: 2013, Physical Properties of a Sunspot Chromosphere with Umbral Flashes. *Astron. Astrophys.* **556**, A115. doi:[10.1051/0004-6361/201321629](https://doi.org/10.1051/0004-6361/201321629).
- de la Cruz Rodríguez, J., Löfdahl, M.G., Sütterlin, P., Hillberg, T., Rouppe van der Voort, L.: 2015, CRISPRED: A Data Pipeline for the CRISP Imaging Spectropolarimeter. *Astron. Astrophys.* **573**, A40. doi:[10.1051/0004-6361/201424319](https://doi.org/10.1051/0004-6361/201424319).
- de Pontieu, B., Title, A.M., Lemen, J.R., Kushner, G.D., Akin, D.J., Allard, B., Berger, T., Boerner, P., Cheung, M., Chou, C., Drake, J.F., Duncan, D.W., Freeland, S., Heyman, G.F., Hoffman, C., Hurlburt, N.E., Lindgren, R.W., Mathur, D., Rehse, R., Sabolish, D., Seguin, R., Schrijver, C.J., Tarbell, T.D., Wülser, J.P., Wolfson, C.J., Yanari, C., Mudge, J., Nguyen-Phuc, N., Timmons, R., van Bezooijen, R., Weingrod, I., Brookner, R., Butcher, G., Dougherty, B., Eder, J., Knagenhjelm, V., Larsen, S., Mansir, D., Phan, L., Boyle, P., Cheimets, P.N., DeLuca, E.E., Golub, L., Gates, R., Hertz, E., McKillop, S., Park, S., Perry, T., Podgorski, W.A., Reeves, K., Saar, S., Testa, P., Tian, H., Weber, M., Dunn, C., Eccles, S., Jaeggli, S.A., Kankelborg, C.C., Mashburn, K., Pust, N., Springer, L., Carvalho, R., Kleint, L., Marmie, J., Mazmanian, E., Pereira, T.M.D., Sawyer, S., Strong, J., Worden, S.P., Carlsson, M., Hansteen, V.H., Leenaarts, J., Wiesmann, M., Aloise, J., Chu, K.C., Bush, R.I., Scherrer, P.H., Brekke, P., Martinez Sykora, J., Lites, B.W., McIntosh, S.W., Uitenbroek, H., Okamoto, T.J., Gummin, M.A., Auken, G., Jerram, P., Pool, P., Waltham, N.: 2014, The Interface Region Imaging Spectrograph (IRIS). *Solar Phys.* **289**, 2733–2779. doi:[10.1007/s11207-014-0485-y](https://doi.org/10.1007/s11207-014-0485-y).
- de Wijn, A.G., Stenflo, J.O., Solanki, S.K., Tsuneta, S.: 2009, Small-Scale Solar Magnetic Fields. *Space Science Rev.* **144**, 275. doi:[10.1007/s11214-008-9473-6](https://doi.org/10.1007/s11214-008-9473-6).
- Deng, H., Zhang, D., Wang, T., Ji, K., Wang, F., Liu, Z., Xiang, Y., Jin, Z., Cao, W.: 2015, Objective Image-Quality Assessment for High-Resolution Photospheric Images by Median Filter-Gradient Similarity. *Solar Phys.* **290**, 1479–1489. doi:[10.1007/s11207-015-0676-1](https://doi.org/10.1007/s11207-015-0676-1).
- Denker, C., Tritschler, A.: 2009, Mini-Filaments – Small-Scale Analogues of Solar Eruptive Events? In: Strassmeier, K.G., Kosovichev, A.G., Beckmann, J.E. (eds.) *Cosmic Magnetic Fields: From Planets, to Stars and Galaxies, IAU Symp.* **259**, 223.
- Denker, C., Didkovsky, L., Ma, J., Shumko, S., Varsik, J., Wang, J., Wang, H., Goode, P.R.: 2003, Imaging Magnetographs for High-Resolution Solar Observations in the Visible and Near-Infrared Wavelength Region. *Astron. Nachr.* **324**, 332.
- Denker, C., Balthasar, H., Hofmann, A., Bello González, N., Volkmer, R.: 2010, The GREGOR Fabry-Pérot Interferometer: A New Instrument for High-Resolution Solar Observations. In:

- McLean, I.S., Ramsay, S.K., Takami, H. (eds.) *Ground-Based and Airborne Instrumentation for Astronomy III, Proc. SPIE* **7735**, 77356M.
- Denker, C., von der Lühe, O., Feller, A., Arlt, K., Balthasar, H., Bauer, S.M., Bello González, N., Berkefeld, T., Caligari, P., Collados, M., Fischer, A., Granzer, T., Hahn, T., Halbgewachs, C., Heidecke, F., Hofmann, A., Kentischer, T., Klvaňa, M., Kneer, F., Lagg, A., Nicklas, H., Popow, E., Puschmann, K.G., Rendtel, J., Schmidt, D., Schmidt, W., Sobotka, M., Solanki, S.K., Soltau, D., Staude, J., Strassmeier, K.G., Volkmer, R., Waldmann, T., Wiehr, E., Wittmann, A.D., Woche, M.: 2012, A Retrospective of the GREGOR Solar Telescope in Scientific Literature. *Astron. Nachr.* **333**, 810. doi:[10.1002/asna.201211728](https://doi.org/10.1002/asna.201211728).
- Esteban Pozuelo, S., Bellot Rubio, L.R., de la Cruz Rodríguez, J.: 2015, Lateral Downflows in Sunspot Penumbra Filaments and their Temporal Evolution. *Astrophys. J.* **803**, 93. doi:[10.1088/0004-637X/803/2/93](https://doi.org/10.1088/0004-637X/803/2/93).
- Everitt, B., Landau, S., Leese, M., Stahl, D.: 2011, *Cluster Analysis, Wiley Series in Probability and Statistics*, Wiley, Chichester, West Sussex, UK.
- Fan, Y.: 2009, Magnetic Fields in the Solar Convection Zone. *Living Rev. Solar Phys.* **6**. doi:[10.12942/lrsp-2009-4](https://doi.org/10.12942/lrsp-2009-4).
- Fang, F., Manchester, W. IV, Abbett, W.P., van der Holst, B.: 2012, Dynamic Coupling of Convective Flows and Magnetic Field during Flux Emergence. *Astrophys. J.* **745**, 37. doi:[10.1088/0004-637X/745/1/37](https://doi.org/10.1088/0004-637X/745/1/37).
- Fanning, D.W.: 2011, *Coyote's Guide to Traditional IDL Graphics*, Coyote Book Publishing, Fort Collins, Colorado, USA.
- Fontenla, J.M., Avrett, E.H., Loeser, R.: 1993, Energy Balance in the Solar Transition Region. III - Helium Emission in Hydrostatic, Constant-Abundance Models with Diffusion. *Astrophys. J.* **406**, 319–345.
- Freeland, S.L., Handy, B.N.: 1998, Data Analysis with the SolarSoft System. *Solar Phys.* **182**, 497.
- Gingerich, O., Noyes, R.W., Kalkofen, W., Cuny, Y.: 1971, The Harvard-Smithsonian Reference Atmosphere. *Solar Phys.* **18**, 347. doi:[10.1007/BF00149057](https://doi.org/10.1007/BF00149057).
- Giordano, S., Berrilli, F., Del Moro, D., Penza, V.: 2008, The Photospheric Structure of a Solar Pore with Light Bridge. *Astron. Astrophys.* **489**, 747–754. doi:[10.1051/0004-6361:20077928](https://doi.org/10.1051/0004-6361:20077928).
- Gömöry, P., Beck, C., Balthasar, H., Rybák, J., Kučera, A., Koza, J., Wöhl, H.: 2010, Magnetic Loop Emergence within a Granule. *Astron. Astrophys.* **511**, A14. doi:[10.1051/0004-6361/200912807](https://doi.org/10.1051/0004-6361/200912807).
- González Manrique, S.J., Kuckein, C., Pastor Yabar, A., Collados, M., Denker, C., Fischer, C.E., Gömöry, P., Diercke, A., Bello González, N., Schlichenmaier, R., Balthasar, H., Berkefeld, T., Feller, A., Hoch, S., Hofmann, A., Kneer, F., Lagg, A., Nicklas, H., Orozco Suárez, D., Schmidt, D., Schmidt, W., Sigwarth, M., Sobotka, M., Solanki, S.K., Soltau, D., Staude, J., Strassmeier, K.G., Verma, M., Volkmer, R., von der Lühe, O., Waldmann, T.: 2016, Fitting Peculiar Spectral Profiles in He I 10830 Å Absorption Features. *Astron. Nachr.* **337**, 1057.
- González Manrique, S.J., Denker, C., Kuckein, C., Pastor Yabar, A., Collados, M., Verma, M., Balthasar, H., Diercke, A., Fischer, C.E., Gömöry, P., Bello González, N., Schlichenmaier, R., Cubas Armas, M., Berkefeld, T., Feller, A., Hoch, S., Hofmann, A., Lagg, A., Nicklas, H., Orozco Suárez, D., Schmidt, D., Schmidt, W., Sigwarth, M., Sobotka, M., Solanki, S.K., Soltau, D., Staude, J., Strassmeier, K.G., Volkmer, R., von der Lühe, O., Waldmann, T.: 2017, Tracking Chromospheric High-Velocity Features in an Arch Filament System. In: Vargas

- Domínguez, S., Kosovichev, A.G., Harra, L., Antolin, P. (eds.) *Fine Structure and Dynamics of the Solar Atmosphere, IAU Symp.* **327**. submitted.
- Granzer, T., Halbgewachs, C., Volkmer, R., Soltau, D.: 2012, Preparing the GREGOR Solar Telescope for Night-Time Use: Deriving a Pointing Model. *Astron. Nachr.* **333**, 823. doi:[10.1002/asna.201211729](https://doi.org/10.1002/asna.201211729).
- Grossmann-Doerth, U., Schüssler, M., Steiner, O.: 1998, Convective Intensification of Solar Surface Magnetic Fields: Results of Numerical Experiments. *Astron. Astrophys.* **337**, 928–939.
- Guglielmino, S.L., Bellot Rubio, L.R., Zuccarello, F., Aulanier, G., Vargas Domínguez, S., Kamio, S.: 2010, Multiwavelength Observations of Small-scale Reconnection Events Triggered by Magnetic Flux Emergence in the Solar Atmosphere. *Astrophys. J.* **724**, 1083. doi:[10.1088/0004-637X/724/2/1083](https://doi.org/10.1088/0004-637X/724/2/1083).
- Guglielmino, S.L., Martínez Pillet, V., Bonet, J.A., del Toro Iniesta, J.C., Bellot Rubio, L.R., Solanki, S.K., Schmidt, W., Gandorfer, A., Barthol, P., Knölker, M.: 2012, The Frontier between Small-Scale Bipoles and Ephemeral Regions in the Solar Photosphere: Emergence and Decay of an Intermediate-Scale Bipole Observed with SUNRISE/IMaX. *Astrophys. J.* **745**, 160. doi:[10.1088/0004-637X/745/2/160](https://doi.org/10.1088/0004-637X/745/2/160).
- Hagenaar, H.J.: 2001, Ephemeral Regions on a Sequence of Full-Disk Michelson Doppler Imager Magnetograms. *Astrophys. J.* **555**, 448.
- Halbgewachs, C., Caligari, P., Glogowski, K., Heidecke, F., Knobloch, M., Mustedanagic, M., Volkmer, R., Waldmann, T.A.: 2012, The GREGOR Telescope Control System. *Astron. Nachr.* **333**, 840. doi:[10.1002/asna.201211732](https://doi.org/10.1002/asna.201211732).
- Hale, G.E.: 1908, On the Probable Existence of a Magnetic Field in Sun-Spots. *Astrophys. J.* **28**, 315. doi:[10.1086/141602](https://doi.org/10.1086/141602).
- Hale, G.E., Nicholson, S.B.: 1925, The Law of Sun-Spot Polarity. *Astrophys. J.* **62**, 270. doi:[10.1086/142933](https://doi.org/10.1086/142933).
- Hale, G.E., Ellerman, F., Nicholson, S.B., Joy, A.H.: 1919, The Magnetic Polarity of Sun-Spots. *Astrophys. J.* **49**, 153. doi:[10.1086/142452](https://doi.org/10.1086/142452).
- Hammerschlag, R.H., Kommers, J.N., Visser, S., Bettonvil, F.C.M., van Schie, A.G.M., van Leverink, S.J., Sliepen, G., Jägers, A.P.L., Schmidt, W., Volkmer, R.: 2012, Open-Foldable Domes with High-Tension Textile Membranes: The GREGOR Dome. *Astron. Nachr.* **333**, 830. doi:[10.1002/asna.201211731](https://doi.org/10.1002/asna.201211731).
- Harvey, J.W., Branston, D., Henney, C.J., Keller, C.U., SOLIS and GONG Teams: 2007, Seething Horizontal Magnetic Fields in the Quiet Solar Photosphere. *Astrophys. J. Lett.* **659**, L177. doi:[10.1086/518036](https://doi.org/10.1086/518036).
- Harvey, K.L., Martin, S.F.: 1973, Ephemeral Active Regions. *Solar Phys.* **32**, 389. doi:[10.1007/BF00154951](https://doi.org/10.1007/BF00154951).
- Heinzel, P., Mein, N., Mein, P.: 1999, Cloud Model with Variable Source Function for Solar H α Structures. II. Dynamical Models. *Astron. Astrophys.* **346**, 322.
- Hirzberger, J.: 2003, Imaging Spectroscopy of Solar Pores. *Astron. Astrophys.* **405**, 331.
- Hofmann, A., Arlt, K., Balthasar, H., Bauer, S.M., Bittner, W., Paschke, J., Popow, E., Rendtel, J., Soltau, D., Waldmann, T.: 2012, The GREGOR Polarimetric Calibration Unit. *Astron. Nachr.* **333**, 854. doi:[10.1002/asna.201211733](https://doi.org/10.1002/asna.201211733).

- Hong, J., Ding, M.D., Li, Y., Fang, C., Cao, W.: 2014, Spectral Observations of Ellerman Bombs and Fitting with a Two-Cloud Model. *Astrophys. J.* **792**, 13. doi:[10.1088/0004-637X/792/1/13](https://doi.org/10.1088/0004-637X/792/1/13).
- Howard, R., Harvey, J.W.: 1964, Photospheric Magnetic Fields and Chromospheric Features. *Astrophys. J.* **139**, 1328. doi:[10.1086/147867](https://doi.org/10.1086/147867).
- Hurlburt, N.E., Rucklidge, A.M.: 2000, Development of Structure in Pores and Sunspots: Flows around Axisymmetric Magnetic Flux Tubes. *Mon. Not. R. Astron. Soc.* **314**, 793. doi:[10.1046/j.1365-8711.2000.03407.x](https://doi.org/10.1046/j.1365-8711.2000.03407.x).
- Keil, S.L., Balasubramaniam, K.S., Smaldone, L.A., Reger, B.: 1999, Velocities in Solar Pores. *Astrophys. J.* **510**, 422.
- Kentischer, T.J., Schmidt, W., Sigwarth, M., Uexkuell, M.V.: 1998, TESOS, a Double Fabry-Perot Instrument for Solar Spectroscopy. *Astron. Astrophys.* **340**, 569.
- Keppens, R., Martinez Pillet, V.: 1996, The Magnetic Structure of Pores and Sunspots Derived from Advanced Stokes Polarimeter Data. *Astron. Astrophys.* **316**, 229.
- Kitiashvili, I.N., Bellot Rubio, L.R., Kosovichev, A.G., Mansour, N.N., Sainz Dalda, A., Wray, A.A.: 2010a, Explanation of the Sea-serpent Magnetic Structure of Sunspot Penumbrae. *Astrophys. J. Lett.* **716**, L181. doi:[10.1088/2041-8205/716/2/L181](https://doi.org/10.1088/2041-8205/716/2/L181).
- Kitiashvili, I.N., Kosovichev, A.G., Wray, A.A., Mansour, N.N.: 2010b, Mechanism of Spontaneous Formation of Stable Magnetic Structures on the Sun. *Astrophys. J.* **719**, 307. doi:[10.1088/0004-637X/719/1/307](https://doi.org/10.1088/0004-637X/719/1/307).
- Kneer, F.: 2012, Hopes and Expectations with GREGOR. *Astron. Nachr.* **333**, 790. doi:[10.1002/asna.201211726](https://doi.org/10.1002/asna.201211726).
- Kosugi, T., Matsuzaki, K., Sakao, T., Shimizu, T., Sone, Y., Tachikawa, S., Hashimoto, T., Minesugi, K., Ohnishi, A., Yamada, T., Tsuneta, S., Hara, H., Ichimoto, K., Suematsu, Y., Shimojo, M., Watanabe, T., Shimada, S., Davis, J.M., Hill, L.D., Owens, J.K., Title, A.M., Culhane, J.L., Harra, L.K., Doschek, G.A., Golub, L.: 2007, The Hinode (Solar-B) Mission: An Overview. *Solar Phys.* **243**, 3. doi:[10.1007/s11207-007-9014-6](https://doi.org/10.1007/s11207-007-9014-6).
- Krödel, M.R., Luchtel, G., Volkmer, R.: 2006, The Cesium Ceramic Optics of the GREGOR Telescope. In: Atad-Ettinger, E., Lemke, D. (eds.) *Optomechanical Technologies for Astronomy, Proc. SPIE* **6273**, 62730Q.
- Kuckein, C., Martínez Pillet, V., Centeno, R.: 2012a, An Active Region Filament Studied Simultaneously in the Chromosphere and Photosphere. I. Magnetic Structure. *Astron. Astrophys.* **539**, A131. doi:[10.1051/0004-6361/201117675](https://doi.org/10.1051/0004-6361/201117675).
- Kuckein, C., Martínez Pillet, V., Centeno, R.: 2012b, An Active Region Filament Studied Simultaneously in the Chromosphere and Photosphere. II. Doppler Velocities. *Astron. Astrophys.* **542**, A112. doi:[10.1051/0004-6361/201218887](https://doi.org/10.1051/0004-6361/201218887).
- Kuckein, C., Verma, M., Denker, C.: 2016, Giant Quiescent Solar Filament Observed with High-Resolution Spectroscopy. *Astron. Astrophys.* **589**, A84. doi:[10.1051/0004-6361/201526636](https://doi.org/10.1051/0004-6361/201526636).
- Kuckein, C., Centeno, R., Martínez Pillet, V., Casini, R., Manso Sainz, R., Shimizu, T.: 2009, Magnetic Field Strength of Active Region Filaments. *Astron. Astrophys.* **501**, 1113. doi:[10.1051/0004-6361/200911800](https://doi.org/10.1051/0004-6361/200911800).
- Kuckein, C., Denker, C., Verma, M., Balthasar, H., González Manrique, S.J., Louis, R.E., Diercke, A.: 2017, sTools – A Data Reduction Pipeline for the GREGOR Fabry-Pérot Interferometer and the High-Resolution Fast Imager at the GREGOR Solar Telescope. In: Vargas Domínguez, S., Kosovichev, A.G., Harra, L., Antolin, P. (eds.) *Fine Structure and Dynamics of the Solar Atmosphere, IAU Symp.* **327**. submitted.

- Lagg, A., Woch, J., Krupp, N., Solanki, S.K.: 2004, Retrieval of the Full Magnetic Vector with the He I Multiplet at 1083 nm. Maps of an Emerging Flux Region. *Astron. Astrophys.* **414**, 1109. doi:[10.1051/0004-6361:20031643](https://doi.org/10.1051/0004-6361:20031643).
- Lagg, A., Woch, J., Solanki, S.K., Krupp, N.: 2007, Supersonic Downflows in the Vicinity of a Growing Pore. Evidence of Unresolved Magnetic Fine Structure at Chromospheric Heights. *Astron. Astrophys.* **462**, 1147. doi:[10.1051/0004-6361:20054700](https://doi.org/10.1051/0004-6361:20054700).
- Lagg, A., Ishikawa, R., Merenda, L., Wiegelmann, T., Tsuneta, S., Solanki, S.K.: 2009, Inter-network Horizontal Magnetic Fields in the Quiet Sun Chromosphere: Results from a Joint Hinode/VTT Study. In: Lites, B., Cheung, M., Magara, T., Mariska, J., Reeves, K. (eds.) *The Second Hinode Science Meeting: Beyond Discovery-Toward Understanding*, *ASP Conf. Ser.* **415**, 327.
- Lee, C.Y., Chae, J., Wang, H.: 2000, Dynamical Characteristics of Small-Scale H α Upflow Events on the Quiet Sun. *Astrophys. J.* **545**, 1124.
- Leenaarts, J., de la Cruz Rodríguez, J., Kochukhov, O., Carlsson, M.: 2014, The Effect of Isotopic Splitting on the Bisector and Inversions of the Solar Ca II 854.2 nm Line. *Astrophys. J. Lett.* **784**, L17.
- Leka, K.D., Skumanich, A.: 1998, The Evolution of Pores and the Development of Penumbrae. *Astrophys. J.* **507**, 454.
- Lemen, J.R., Title, A.M., Akin, D.J., Boerner, P.F., Chou, C., Drake, J.F., Duncan, D.W., Edwards, C.G., Friedlaender, F.M., Heyman, G.F., Hurlburt, N.E., Katz, N.L., Kushner, G.D., Levay, M., Lindgren, R.W., Mathur, D.P., McFeaters, E.L., Mitchell, S., Rehse, R.A., Schrijver, C.J., Springer, L.A., Stern, R.A., Tarbell, T.D., Wuelser, J.P., Wolfson, C.J., Yanari, C., Bookbinder, J.A., Cheimets, P.N., Caldwell, D., Deluca, E.E., Gates, R., Golub, L., Park, S., Podgorski, W.A., Bush, R.I., Scherrer, P.H., Gummin, M.A., Smith, P., Auker, G., Jerram, P., Pool, P., Souffi, R., Windt, D.L., Beardsley, S., Clapp, M., Lang, J., Waltham, N.: 2012, The Atmospheric Imaging Assembly (AIA) on the Solar Dynamics Observatory (SDO). *Solar Phys.* **275**, 17. doi:[10.1007/s11207-011-9776-8](https://doi.org/10.1007/s11207-011-9776-8).
- Li, X., Yang, Z., Zhang, H.: 2015, Formation of Pores Associated with the Inflow of Moving Magnetic Features. *Astrophys. J.* **807**, 160. doi:[10.1088/0004-637X/807/2/160](https://doi.org/10.1088/0004-637X/807/2/160).
- Lites, B.W., Martinez Pillet, V., Skumanich, A.: 1994, A Quantitative Comparison of Vector Magnetic Field Measurement and Analysis Techniques. *Solar Phys.* **155**, 1. doi:[10.1007/BF00670727](https://doi.org/10.1007/BF00670727).
- Lites, B.W., Skumanich, A., Martinez Pillet, V.: 1998, Vector Magnetic Fields of Emerging Solar Flux. I. Properties at the Site of Emergence. *Astron. Astrophys.* **333**, 1053.
- Löfdahl, M.G.: 2002, Multi-Frame Blind Deconvolution with Linear Equality Constraints. In: Bones, P.J., Fiddy, M.A., Millane, R.P. (eds.) *Image Reconstruction from Incomplete Data*, *Proc. SPIE* **4792**, 146. doi:[10.1117/12.451791](https://doi.org/10.1117/12.451791).
- Ma, L., Zhou, W., Zhou, G., Zhang, J.: 2015, The Evolution of Arch Filament Systems and Moving Magnetic Features around a Sunspot. *Astron. Astrophys.* **583**, A110. doi:[10.1051/0004-6361/201424872](https://doi.org/10.1051/0004-6361/201424872).
- Mackay, D., Yeates, A.: 2012, The Sun's Global Photospheric and Coronal Magnetic Fields: Observations and Models. *Living Rev. Solar Phys.* **9**. doi:[10.12942/lrsp-2012-6](https://doi.org/10.12942/lrsp-2012-6).
- Mackay, D.H., Karpen, J.T., Ballester, J.L., Schmieder, B., Aulanier, G.: 2010, Physics of Solar Prominences. II. Magnetic Structure and Dynamics. *Space Science Rev.* **151**, 333. doi:[10.1007/s11214-010-9628-0](https://doi.org/10.1007/s11214-010-9628-0).

- Markwardt, C.B.: 2009, Non-Linear Least-Squares Fitting in IDL with MPFIT. In: Bohlender, D.A., Durand, D., Dowler, P. (eds.) *Astronomical Data Analysis Software and Systems XVIII, ASP Conf. Ser.* **411**, 251.
- Martin, S.F.: 1988, The Identification and Interaction of Network, Intranetwork, and Ephemeral-Region Magnetic Fields. *Solar Phys.* **117**, 243. doi:[10.1007/BF00147246](https://doi.org/10.1007/BF00147246).
- Martínez González, M.J., Manso Sainz, R., Asensio Ramos, A., Bellot Rubio, L.R.: 2010, Small Magnetic Loops Connecting the Quiet Surface and the Hot Outer Atmosphere of the Sun. *Astrophys. J. Lett.* **714**, L94. doi:[10.1088/2041-8205/714/1/L94](https://doi.org/10.1088/2041-8205/714/1/L94).
- Martínez Pillet, V., Del Toro Iniesta, J.C., Álvarez-Herrero, A., Domingo, V., Bonet, J.A., González Fernández, L., López Jiménez, A., Pastor, C., Gasent Blesa, J.L., Mellado, P., Piqueras, J., Aparicio, B., Balaguer, M., Ballesteros, E., Belenguer, T., Bellot Rubio, L.R., Berkefeld, T., Collados, M., Deutsch, W., Feller, A., Girela, F., Grauf, B., Heredero, R.L., Herranz, M., Jerónimo, J.M., Laguna, H., Meller, R., Menéndez, M., Morales, R., Orozco Suárez, D., Ramos, G., Reina, M., Ramos, J.L., Rodríguez, P., Sánchez, A., Uribe-Patarroyo, N., Barthol, P., Gandorfer, A., Knoelker, M., Schmidt, W., Solanki, S.K., Vargas Domínguez, S.: 2011, The Imaging Magnetograph eXperiment (IMaX) for the Sunrise Balloon-Borne Solar Observatory. *Solar Phys.* **268**, 57. doi:[10.1007/s11207-010-9644-y](https://doi.org/10.1007/s11207-010-9644-y).
- Martínez-Sykora, J., Hansteen, V., Carlsson, M.: 2008, Twisted Flux Tube Emergence from the Convection Zone to the Corona. *Astrophys. J.* **679**, 871. doi:[10.1086/587028](https://doi.org/10.1086/587028).
- Martínez-Sykora, J., Hansteen, V., Carlsson, M.: 2009, Twisted Flux Tube Emergence from the Convection Zone to the Corona. II. Later States. *Astrophys. J.* **702**, 129. doi:[10.1088/0004-637X/702/1/129](https://doi.org/10.1088/0004-637X/702/1/129).
- Martres, M.J., Michard, R., Soru-Iscovi: 1966, Étude Morphologique de la Structure Magnétique des Régions Actives en Relation avec les Phénomènes Chromosphériques et les Éruptions Solaires. II. Localisation des Plages Brillantes, Filaments et Éruptions. *Annales d'Astrophysique* **29**, 249.
- Mathew, S.K., Martínez Pillet, V., Solanki, S.K., Krivova, N.A.: 2007, Properties of Sunspots in Cycle 23. I. Dependence of Brightness on Sunspot Size and Cycle Phase. *Astron. Astrophys.* **465**, 291. doi:[10.1051/0004-6361:20066356](https://doi.org/10.1051/0004-6361:20066356).
- Mein, N., Mein, P., Heinzel, P., Vial, J., Malherbe, J.M., Staiger, J.: 1996, Cloud Model with Variable Source Function for Solar H α Structures. *Astron. Astrophys.* **309**, 275.
- Mein, P., Mein, N.: 1988, Differential Cloud Models for Solar Velocity Field Measurements. *Astron. Astrophys.* **203**, 162.
- Molowny-Horas, R., Heinzel, P., Mein, P., Mein, N.: 1999, A Non-LTE Inversion Procedure for Chromospheric Cloud-Like Features. *Astron. Astrophys.* **345**, 618.
- Moré, J.J.: 1977, The Levenberg-Marquardt Algorithm: Implementation and Theory. In: Watson, G.A. (ed.) *Numerical Analysis, Lecture Notes in Mathematics* **630**, Springer, Berlin, 105.
- Moré, J.J., Wright, S.J.: 1993, *Optimization Software Guide, Frontiers in Applied Mathematics* **14**, Society for Industrial and Applied Mathematics (SIAM), Philadelphia, USA.
- Moreno-Insertis, F.: 1997, Emergence of Magnetic Flux from the Solar Interior. *Mem. Soc. Astron. Ital.* **68**, 429.
- Morinaga, S., Sakurai, T., Ichimoto, K., Yokoyama, T., Shimojo, M., Katsukawa, Y.: 2008, Suppression of Convection around Small Magnetic Concentrations. *Astron. Astrophys.* **481**, L29. doi:[10.1051/0004-6361:20079029](https://doi.org/10.1051/0004-6361:20079029).

- Muglach, K., Sütterlin, P.: 1998, Simultaneous Observations with the GCT and SoHO: High Velocity Events in the Upper Chromosphere. In: Alissandrakis, C.E., Schmieder, B. (eds.) *Three-Dimensional Structure of Solar Active Regions, ASP Conf. Ser.* **155**, 341.
- Muglach, K., Schmidt, W., Knoelker, M.: 1997, Multiple Velocities Observed in He I 1083 nm. *Solar Phys.* **172**, 103. doi:[10.1023/A:1004988205716](https://doi.org/10.1023/A:1004988205716).
- Neckel, H., Labs, D.: 1984, The Solar Radiation between 3300 and 12500 Å. *Solar Phys.* **90**, 205. doi:[10.1007/BF00173953](https://doi.org/10.1007/BF00173953).
- November, L.J., Simon, G.W.: 1988, Precise Proper-Motion Measurement of Solar Granulation. *Astrophys. J.* **333**, 427. doi:[10.1086/166758](https://doi.org/10.1086/166758).
- Orozco Suárez, D., Katsukawa, Y., Bellot Rubio, L.R.: 2012, The Connection between Internetwork Magnetic Elements and Supergranular Flows. *Astrophys. J. Lett.* **758**, L38. doi:[10.1088/2041-8205/758/2/L38](https://doi.org/10.1088/2041-8205/758/2/L38).
- Pariat, E., Aulanier, G., Schmieder, B., Georgoulis, M.K., Rust, D.M., Bernasconi, P.N.: 2004, Resistive Emergence of Undulatory Flux Tubes. *Astrophys. J.* **614**, 1099. doi:[10.1086/423891](https://doi.org/10.1086/423891).
- Parker, E.N.: 1978, Hydraulic Concentration of Magnetic Fields in the Solar Photosphere. VI - Adiabatic Cooling and Concentration in Downdrafts. *Astrophys. J.* **221**, 368–377. doi:[10.1086/156035](https://doi.org/10.1086/156035).
- Parker, E.N.: 1979, Sunspots and the Physics of Magnetic Flux Tubes. IX. Umbral Dots and Longitudinal Overstability. *Astrophys. J.* **234**, 333. doi:[10.1086/157501](https://doi.org/10.1086/157501).
- Penn, M.J., Kuhn, J.R.: 1995, Imaging Spectropolarimetry of the He I 1083 Nanometer Line in a Flaring Solar Active Region. *Astrophys. J. Lett.* **441**, L51–L54. doi:[10.1086/187787](https://doi.org/10.1086/187787).
- Perona, P., Malik, J.: 1990, Scale-Space and Edge Detection Using Anisotropic Diffusion. *IEEE Trans. Pattern Anal. Mach. Intell.* **12**, 629. doi:[10.1109/34.56205](https://doi.org/10.1109/34.56205).
- Pesnell, W.D., Thompson, B.J., Chamberlin, P.C.: 2012, The Solar Dynamics Observatory (SDO). *Solar Phys.* **275**, 3.
- Pevtsov, A.A., Bertello, L., Tlatov, A.G., Kilcik, A., Nagovitsyn, Y.A., Cliver, E.W.: 2014, Cyclic and Long-Term Variation of Sunspot Magnetic Fields. *Solar Phys.* **289**, 593. doi:[10.1007/s11207-012-0220-5](https://doi.org/10.1007/s11207-012-0220-5).
- Priest, E.: 2014, *Magnetohydrodynamics of the Sun*, Cambridge University Press, New York.
- Puschmann, K.G., Kneer, F., Seelemann, T., Wittmann, A.D.: 2006, The New Göttingen Fabry-Pérot Spectrometer for Two-Dimensional Observations of the Sun. *Astron. Astrophys.* **451**, 1151. doi:[10.1051/0004-6361:20054487](https://doi.org/10.1051/0004-6361:20054487).
- Puschmann, K.G., Kneer, F., Nicklas, H., Wittmann, A.D.: 2007, From the Göttingen Fabry-Pérot Interferometer to the GREGOR FPI. In: Kneer, F., Puschmann, K.G., Wittmann, A.D. (eds.) *Modern Solar Facilities – Advanced Solar Science*, Universitätsverlag Göttingen, Göttingen, Germany, 45.
- Puschmann, K.G., Denker, C., Kneer, F., Al Erdogan, N., Balthasar, H., Bauer, S.M., Beck, C., Bello González, N., Collados, M., Hahn, T., Hirzberger, J., Hofmann, A., Louis, R.E., Nicklas, H., Okunev, O., Martínez Pillet, V., Popow, E., Seelemann, T., Volkmer, R., Wittmann, A.D., Woche, M.: 2012, The GREGOR Fabry-Pérot Interferometer. *Astron. Nachr.* **333**, 880. doi:[10.1002/asna.201211734](https://doi.org/10.1002/asna.201211734).
- Puschmann, K.G., Denker, C., Balthasar, H., Louis, R.E., Popow, E., Woche, M., Beck, C., Seelemann, T., Volkmer, R.: 2013, GREGOR Fabry-Pérot Interferometer and its Companion the Blue Imaging Solar Spectrometer. *Opt. Eng.* **52**, 081606. doi:[10.1117/1.OE.52.8.081606](https://doi.org/10.1117/1.OE.52.8.081606).

- Quintero Noda, C., Shimizu, T., Ruiz Cobo, B., Suematsu, Y., Katsukawa, Y., Ichimoto, K.: 2016, Analysis of a Spatially Deconvolved Solar Pore. *Mon. Not. R. Astron. Soc.* **460**, 1476. doi:[10.1093/mnras/stw1068](https://doi.org/10.1093/mnras/stw1068).
- Rempel, M.: 2011, Subsurface Magnetic Field and Flow Structure of Simulated Sunspots. *Astrophys. J.* **740**, 15.
- Rempel, M.: 2012, Numerical Sunspot Models: Robustness of Photospheric Velocity and Magnetic Field Structure. *Astrophys. J.* **750**, 62. doi:[10.1088/0004-637X/750/1/62](https://doi.org/10.1088/0004-637X/750/1/62).
- Rempel, M., Cheung, M.C.M.: 2014, Numerical Simulations of Active Region Scale Flux Emergence: From Spot Formation to Decay. *Astrophys. J.* **785**, 90. doi:[10.1088/0004-637X/785/2/90](https://doi.org/10.1088/0004-637X/785/2/90).
- Rempel, M., Schüssler, M., Cameron, R.H., Knölker, M.: 2009, Penumbra Structure and Outflows in Simulated Sunspots. *Science* **325**, 171.
- Rezaei, R., Bello González, N., Schlichenmaier, R.: 2012, The Formation of Sunspot Penumbra. Magnetic Field Properties. *Astron. Astrophys.* **537**, A19. doi:[10.1051/0004-6361/201117485](https://doi.org/10.1051/0004-6361/201117485).
- Roupe van der Voort, L.H.M., Hansteen, V.H., Carlsson, M., Fossum, A., Marthinussen, E., van Noort, M.J., Berger, T.E.: 2005, Solar Magnetic Elements at 0.1 arcsec Resolution. II. Dynamical Evolution. *Astron. Astrophys.* **435**, 327. doi:[10.1051/0004-6361:20042561](https://doi.org/10.1051/0004-6361:20042561).
- Roupe van der Voort, L., van Noort, M., Carlsson, M., Hansteen, V.: 2006, High Spatial Resolution Observations of Solar Magnetic Structures. In: Leibacher, J., Stein, R.F., Uitenbroek, H. (eds.) *Solar MHD Theory and Observations: A High Spatial Resolution Perspective*, ASP Conf. Ser. **354**, 37.
- Rucklidge, A.M., Schmidt, H.U., Weiss, N.O.: 1995, The Abrupt Development of Penumbrae in Sunspots. *Mon. Not. R. Astron. Soc.* **273**, 491.
- Ruiz Cobo, B., del Toro Iniesta, J.C.: 1992, Inversion of Stokes Profiles. *Astrophys. J.* **398**, 375.
- Sasso, C., Lagg, A., Solanki, S.K.: 2011, Multicomponent He I 10830 Å Profiles in an Active Filament. *Astron. Astrophys.* **526**, A42. doi:[10.1051/0004-6361/200912956](https://doi.org/10.1051/0004-6361/200912956).
- Sasso, C., Lagg, A., Solanki, S.K.: 2014, Magnetic Structure of an Activated Filament in a Flaring Active Region. *Astron. Astrophys.* **561**, A98. doi:[10.1051/0004-6361/201322481](https://doi.org/10.1051/0004-6361/201322481).
- Sasso, C., Lagg, A., Solanki, S.K., Aznar Cuadrado, R., Collados, M.: 2007, Full-Stokes Observations and Analysis of He I 10830 Å in a Flaring Region. In: Heinzel, P., Dorotovič, I., Rutten, R.J. (eds.) *The Physics of Chromospheric Plasmas*, ASP Conf. Ser. **368**, 467.
- Schad, T.A., Penn, M.J., Lin, H.: 2013, He I Vector Magnetometry of Field-Aligned Superpenumbral Fibrils. *Astrophys. J.* **768**, 111. doi:[10.1088/0004-637X/768/2/111](https://doi.org/10.1088/0004-637X/768/2/111).
- Scharmer, G.B.: 2006, Comments on the Optimization of High Resolution Fabry-Pérot Filtergraphs. *Astron. Astrophys.* **447**, 1111.
- Scharmer, G.B., Gudiksen, B.V., Kiselman, D., Löfdahl, M.G., Roupe van der Voort, L.H.M.: 2002, Dark Cores in Sunspot Penumbra Filaments. *Nature* **420**, 151.
- Scharmer, G.B., Bjelksjo, K., Korhonen, T.K., Lindberg, B., Petterson, B.: 2003, The 1-Meter Swedish Solar Telescope. In: Keil, S.L., Avakyan, S.V. (eds.) *Innovative Telescopes and Instrumentation for Solar Astrophysics*, Proc. SPIE **4853**, 341.
- Scharmer, G.B., Narayan, G., Hillberg, T., de la Cruz Rodriguez, J., Löfdahl, M.G., Kiselman, D., Sütterlin, P., van Noort, M., Lagg, A.: 2008, CRISP Spectropolarimetric Imaging of Penumbra Fine Structure. *Astrophys. J. Lett.* **689**, L69.

- Scherrer, P.H., Bogart, R.S., Bush, R.I., Hoeksema, J.T., Kosovichev, A.G., Schou, J., Rosenberg, W., Springer, L., Tarbell, T.D., Title, A., Wolfson, C.J., Zayer, I., MDI Engineering Team: 1995, The Solar Oscillations Investigation – Michelson Doppler Imager. *Solar Phys.* **162**, 129. doi:[10.1007/BF00733429](https://doi.org/10.1007/BF00733429).
- Scherrer, P.H., Schou, J., Bush, R.I., Kosovichev, A.G., Bogart, R.S., Hoeksema, J.T., Liu, Y., Duvall, T.L., Zhao, J., Title, A.M., Schrijver, C.J., Tarbell, T.D., Tomczyk, S.: 2012, The Helioseismic and Magnetic Imager (HMI) Investigation for the Solar Dynamics Observatory (SDO). *Solar Phys.* **275**, 207.
- Schlichenmaier, R., Collados, M.: 2002, Spectropolarimetry in a Sunspot Penumbra. Spatial Dependence of Stokes Asymmetries in Fe I 1564.8 nm. *Astron. Astrophys.* **381**, 668–682. doi:[10.1051/0004-6361:20011459](https://doi.org/10.1051/0004-6361:20011459).
- Schlichenmaier, R., Bello González, N., Rezaei, R., Waldmann, T.A.: 2010, The Role of Emerging Bipoles in the Formation of a Sunspot Penumbra. *Astron. Nachr.* **331**, 563. doi:[10.1002/asna.201011372](https://doi.org/10.1002/asna.201011372).
- Schmidt, W., Soltau, D.: 1987, Construction of the German Solar Telescopes in the Observatorio del Teide, Tenerife: The Vacuum Tower Telescope. *Mitt. Astron. Ges. Hamburg* **68**, 184.
- Schmidt, W., Muglach, K., Knölker, M.: 2000, Free-fall Downflow Observed in He I 1083.0 Nanometers and H β . *Astrophys. J.* **544**, 567. doi:[10.1086/317169](https://doi.org/10.1086/317169).
- Schmidt, W., Stix, M., Wöhl, H.: 1999, Center-to-Limb Variation of the Solar Oscillation. New Results from MDI Data. *Astron. Astrophys.* **346**, 633.
- Schmidt, W., Beck, C., Kentischer, T., Elmore, D., Lites, B.: 2003, POLIS: A Spectropolarimeter for the VTT and for GREGOR. *Astron. Nachr.* **324**, 300. doi:[10.1002/asna.200310101](https://doi.org/10.1002/asna.200310101).
- Schmidt, W., von der Lühe, O., Volkmer, R., Denker, C., Solanki, S.K., Balthasar, H., Bello González, N., Berkefeld, T., Collados, M., Fischer, A., Halbgewachs, C., Heidecke, F., Hofmann, A., Kneer, F., Lagg, A., Nicklas, H., Popow, E., Puschmann, K.G., Schmidt, D., Sigwarth, M., Sobotka, M., Soltau, D., Staude, J., Strassmeier, K.G., Waldmann, T.A.: 2012, The 1.5 Meter Solar Telescope GREGOR. *Astron. Nachr.* **333**, 796. doi:[10.1002/asna.201211725](https://doi.org/10.1002/asna.201211725).
- Schmieder, B., Archontis, V., Pariat, E.: 2014, Magnetic Flux Emergence along the Solar Cycle. *Space Science Rev.* **186**, 227. doi:[10.1007/s11214-014-0088-9](https://doi.org/10.1007/s11214-014-0088-9).
- Schmieder, B., Raadu, M.A., Wiik, J.E.: 1991, Fine Structure of Solar Filaments. II. Dynamics of Threads and Footpoints. *Astron. Astrophys.* **252**, 353.
- Schmieder, B., Rust, D.M., Georgoulis, M.K., Démoulin, P., Bernasconi, P.N.: 2004, Emerging Flux and the Heating of Coronal Loops. *Astrophys. J.* **601**, 530. doi:[10.1086/380199](https://doi.org/10.1086/380199).
- Schou, J., Scherrer, P.H., Bush, R.I., Wachter, R., Couvidat, S., Rabello-Soares, M.C., Bogart, R.S., Hoeksema, J.T., Liu, Y., Duvall, T.L., Akin, D.J., Allard, B.A., Miles, J.W., Rairden, R., Shine, R.A., Tarbell, T.D., Title, A.M., Wolfson, C.J., Elmore, D.F., Norton, A.A., Tomczyk, S.: 2012, Design and Ground Calibration of the Helioseismic and Magnetic Imager (HMI) Instrument on the Solar Dynamics Observatory (SDO). *Solar Phys.* **275**, 229. doi:[10.1007/s11207-011-9842-2](https://doi.org/10.1007/s11207-011-9842-2).
- Schrijver, C.J., Title, A.M., van Ballegoijen, A.A., Hagenaar, H.J., Shine, R.A.: 1997, Sustaining the Quiet Photospheric Network: The Balance of Flux Emergence, Fragmentation, Merging, and Cancellation. *Astrophys. J.* **487**, 424.
- Schröter, E.H., Soltau, D., Wiehr, E.: 1985, The German Solar Telescopes at the Observatorio del Teide. *Vistas Astron.* **28**, 519. doi:[10.1016/0083-6656\(85\)90073-X](https://doi.org/10.1016/0083-6656(85)90073-X).

- Severnyi, A.B.: 1965, The Nature of Solar Magnetic Fields (The Fine Structure of the Field). *Sov. Astron.* **9**, 171.
- Simon, G.W., Weiss, N.O.: 1970, On the Magnetic Field in Pores. *Solar Phys.* **13**, 85. doi:[10.1007/BF00963944](https://doi.org/10.1007/BF00963944).
- Sobotka, M.: 2003, Solar Activity. II. Sunspots and Pores. *Astron. Nachr.* **324**, 369. doi:[10.1002/asna.200310132](https://doi.org/10.1002/asna.200310132).
- Sobotka, M., Vázquez, M., Bonet, J.A., Hanslmeier, A.: 1999, Interaction of Convective Structures with the Magnetic Field of Solar Pores. In: Schmieder, B., Hofmann, A., Staude, J. (eds.) *Third Advances in Solar Physics Euroconference: Magnetic Fields and Oscillations*, *ASP Conf. Ser.* **184**, 60.
- Sobotka, M., Del Moro, D., Jurčák, J., Berrilli, F.: 2012, Magnetic and Velocity Fields of a Solar Pore. *Astron. Astrophys.* **537**, A85. doi:[10.1051/0004-6361/201117851](https://doi.org/10.1051/0004-6361/201117851).
- Socas-Navarro, H.: 2001, Stokes Inversion Techniques: Recent Achievements and Future Horizons. In: Sigwarth, M. (ed.) *Advanced Solar Polarimetry – Theory, Observation, and Instrumentation*, *ASP Conf. Ser.* **236**, 487.
- Socas-Navarro, H., Uitenbroek, H.: 2004, On the Diagnostic Potential of H α for Chromospheric Magnetism. *Astrophys. J. Lett.* **603**, L129. doi:[10.1086/383147](https://doi.org/10.1086/383147).
- Socas-Navarro, H., de la Cruz Rodríguez, J., Asensio Ramos, A., Trujillo Bueno, J., Ruiz Cobo, B.: 2015, An Open-Source, Massively Parallel Code for Non-LTE Synthesis and Inversion of Spectral Lines and Zeeman-Induced Stokes Profiles. *Astron. Astrophys.* **577**, A7.
- Solanki, S.K.: 2003, Sunspots: An Overview. *Astron. Astrophys. Rev.* **11**, 153.
- Solanki, S.K., Lagg, A., Woch, J., Krupp, N., Collados, M.: 2003, Three-Dimensional Magnetic Field Topology in a Region of Solar Coronal Heating. *Nature* **425**, 692. doi:[10.1038/nature02035](https://doi.org/10.1038/nature02035).
- Soltau, D., Volkmer, R., von der Lühe, O., Berkefeld, T.: 2012, Optical Design of the New Solar Telescope GREGOR. *Astron. Nachr.* **333**, 847. doi:[10.1002/asna.201211730](https://doi.org/10.1002/asna.201211730).
- Spadaro, D., Billotta, S., Contarino, L., Romano, P., Zuccarello, F.: 2004, AFS Dynamic Evolution During the Emergence of an Active Region. *Astron. Astrophys.* **425**, 309. doi:[10.1051/0004-6361:20041004](https://doi.org/10.1051/0004-6361:20041004).
- Spruit, H.C.: 1979, Convective Collapse of Flux Tubes. *Solar Phys.* **61**, 363.
- Spruit, H.C.: 1981, Motion of Magnetic Flux Tubes in the Solar Convection Zone and Chromosphere. *Astron. Astrophys.* **98**, 155–160.
- Staiger, J.: 2012a, HELLRIDE: A New Interferometric Multiline Instrument for the Analysis of the Solar Atmosphere. In: *Ground-Based and Airborne Instrumentation for Astronomy IV*, *Proc. SPIE* **8446**, 844675. doi:[10.1117/12.926295](https://doi.org/10.1117/12.926295).
- Staiger, J.: 2012b, HELLRIDE: A New Multiline Spectrometer for the Vacuum Tower Telescope, Tenerife. In: Rimmele, T.R., Tritschler, A., Wöger, F., Collados Vera, M., Socas-Navarro, H., Schlichenmaier, R., Carlsson, M., Berger, T., Cadavid, A., Gilbert, P.R., Goode, P.R., Knölker, M. (eds.) *Second ATST-EAST Meeting: Magnetic Fields from the Photosphere to the Corona.*, *ASP Conf. Ser.* **463**, 445.
- Stein, R.F.: 2012, Solar Surface Magneto-Convection. *Living Rev. Solar Phys.* **9**. doi:[10.12942/lrsp-2012-4](https://doi.org/10.12942/lrsp-2012-4).

- Stein, R.F., Nordlund, Å.: 2012a, Flux Emergence and Pore Formation: What ATST can See. In: Rimmele, T.R., Tritschler, A., Wöger, F., Collados Vera, M., Socas-Navarro, H., Schlichenmaier, R., Carlsson, M., Berger, T., Cadavid, A., Gilbert, P.R., Goode, P.R., Knölker, M. (eds.) *Second ATST-EAST Meeting: Magnetic Fields from the Photosphere to the Corona*, *ASP Conf. Ser.* **463**, 83.
- Stein, R.F., Nordlund, Å.: 2012b, On the Formation of Active Regions. *Astrophys. J. Lett.* **753**, L13. doi:[10.1088/2041-8205/753/1/L13](https://doi.org/10.1088/2041-8205/753/1/L13).
- Stein, R.F., Lagerfjärd, A., Nordlund, Å., Georgobiani, D.: 2011, Solar Flux Emergence Simulations. *Solar Phys.* **268**, 271. doi:[10.1007/s11207-010-9510-y](https://doi.org/10.1007/s11207-010-9510-y).
- Stein, R.F., Lagerfjärd, A., Nordlund, Å., Georgobiani, D.: 2012, Emerging Flux Simulations and Proto-Active Regions. In: Bellot Rubio, L., Reale, F., Carlsson, M. (eds.) *4th Hinode Science Meeting: Unsolved Problems and Recent Insights*, *ASP Conf. Ser.* **455**, 133.
- Stenflo, J.O.: 1989, Small-Scale Magnetic Structures on the Sun. *Astron. Astrophys. Rev.* **1**, 3. doi:[10.1007/BF00872483](https://doi.org/10.1007/BF00872483).
- Stenflo, J.O.: 2014, Nature of Quiet-Sun Magnetic Fields. In: Nagendra, K.N., Stenflo, J.O., Qu, Q., Samooprna, M. (eds.) *Solar Polarization 7*, *ASP Conf. Ser.* **489**, 3.
- Stix, M.: 2004, *The Sun: An Introduction*, Springer, Berlin, Germany.
- Strassmeier, K.G., Ilyin, I.V., Woche, M., Granzer, T., Weber, M., Weingrill, J., Bauer, S.M., Popow, E., Denker, C., Schmidt, W., von der Lühe, O., Berdyugina, S., Collados, M., Koubsky, P., Hackman, T., Mantere, M.J.: 2012, Gregor@Night: The Future High-Resolution Stellar Spectrograph for the GREGOR Solar Telescope. *Astron. Nachr.* **333**, 901. doi:[10.1002/asna.201211727](https://doi.org/10.1002/asna.201211727).
- Strous, L.H., Zwaan, C.: 1999, Phenomena in an Emerging Active Region. II. Properties of the Dynamic Small-Scale Structure. *Astrophys. J.* **527**, 435. doi:[10.1086/308071](https://doi.org/10.1086/308071).
- Strous, L.H., Scharmer, G., Tarbell, T.D., Title, A.M., Zwaan, C.: 1996, Phenomena in an Emerging Active Region. I. Horizontal Dynamics. *Astron. Astrophys.* **306**, 947.
- Sütterlin, P.: 1998, Properties of Solar Pores. *Astron. Astrophys.* **333**, 305.
- Sütterlin, P., Schröter, E.H., Muglach, K.: 1996, Polarimetry of Solar Pores. *Solar Phys.* **164**, 311.
- Tandberg-Hanssen, E. (ed.): 1995, *The Nature of Solar Prominences, Astrophysics and Space Science Library* **199**. doi:[10.1007/978-94-017-3396-0](https://doi.org/10.1007/978-94-017-3396-0).
- Teriaca, L., Falchi, A., Cauzzi, G., Falciani, R., Smaldone, L.A., Andretta, V.: 2003, Solar and Heliospheric Observatory/Coronal Diagnostic Spectrograph and Ground-Based Observations of a Two-Ribbon Flare: Spatially Resolved Signatures of Chromospheric Evaporation. *Astrophys. J.* **588**, 596. doi:[10.1086/373946](https://doi.org/10.1086/373946).
- Thomas, J.H., Weiss, N.O.: 2004, Fine Structure in Sunspots. *Ann. Rev. Astron. Astrophys.* **42**, 517. doi:[10.1146/annurev.astro.42.010803.115226](https://doi.org/10.1146/annurev.astro.42.010803.115226).
- Tlatov, A.G., Vasil'eva, V.V., Pevtsov, A.A.: 2010, Distribution of Magnetic Bipoles on the Sun over Three Solar Cycles. *Astrophys. J.* **717**, 357. doi:[10.1088/0004-637X/717/1/357](https://doi.org/10.1088/0004-637X/717/1/357).
- Tortosa-Andreu, A., Moreno-Insertis, F.: 2009, Magnetic Flux Emergence into the Solar Photosphere and Chromosphere. *Astron. Astrophys.* **507**, 949. doi:[10.1051/0004-6361/200912394](https://doi.org/10.1051/0004-6361/200912394).
- Trujillo Bueno, J., Shchukina, N., Asensio Ramos, A.: 2004, A Substantial Amount of Hidden Magnetic Energy in the Quiet Sun. *Nature* **430**, 326. doi:[10.1038/nature02669](https://doi.org/10.1038/nature02669).

- Tsiropoula, G., Georgakilas, A.A., Alissandrakis, C.E., Mein, P.: 1992, Time Evolution of Arch Filaments. *Astron. Astrophys.* **262**, 587.
- Tsuneta, S., Ichimoto, K., Katsukawa, Y., Nagata, S., Otsubo, M., Shimizu, T., Suematsu, Y., Nakagiri, M., Noguchi, M., Tarbell, T., Title, A., Shine, R., Rosenberg, W., Hoffmann, C., Jurcevich, B., Kushner, G., Levay, M., Lites, B., Elmore, D., Matsushita, T., Kawaguchi, N., Saito, H., Mikami, I., Hill, L.D., Owens, J.K.: 2008, The Solar Optical Telescope for the Hinode Mission: An Overview. *Solar Phys.* **249**, 167. doi:[10.1007/s11207-008-9174-z](https://doi.org/10.1007/s11207-008-9174-z).
- Tziotziou, K., Tsiropoula, G., Mein, P.: 2003, On the Nature of the Chromospheric Fine Structure. I. Dynamics of Dark Mottles and Grains. *Astron. Astrophys.* **402**, 361.
- Tziotziou, K., Heinzel, P., Mein, P., Mein, N.: 2001, Non-LTE Inversion of Chromospheric Ca II Cloud-Like Features. *Astron. Astrophys.* **366**, 686.
- Uitenbroek, H., Balasubramaniam, K.S., Tritschler, A.: 2006, Evidence for a Siphon Flow Ending near the Edge of a Pore. *Astrophys. J.* **645**, 776.
- van Driel-Gesztelyi, L., Green, L.M.: 2015, Evolution of Active Regions. *Living Rev. Solar Phys.* **12**, 1. doi:[10.1007/lrsp-2015-1](https://doi.org/10.1007/lrsp-2015-1).
- van Driel-Gesztelyi, L., Petrovay, K.: 1990, Asymmetric Flux Loops in Active Regions. *Solar Phys.* **126**, 285. doi:[10.1007/BF00153051](https://doi.org/10.1007/BF00153051).
- van Noort, M., Rouppe van der Voort, L., Löfdahl, M.G.: 2005, Solar Image Restoration by Use of Multi-Frame Blind Deconvolution with Multiple Objects and Phase Diversity. *Solar Phys.* **228**, 191. doi:[10.1007/s11207-005-5782-z](https://doi.org/10.1007/s11207-005-5782-z).
- Vargas Domínguez, S., van Driel-Gesztelyi, L., Bellot Rubio, L.R.: 2012, Granular-Scale Elementary Flux Emergence Episodes in a Solar Active Region. *Solar Phys.* **278**, 99. doi:[10.1007/s11207-012-9968-x](https://doi.org/10.1007/s11207-012-9968-x).
- Verma, M., Denker, C.: 2011, Horizontal Flow Fields Observed in Hinode G-Band Images. I. Methods. *Astron. Astrophys.* **529**, A153. doi:[10.1051/0004-6361/201016358](https://doi.org/10.1051/0004-6361/201016358).
- Verma, M., Denker, C.: 2012, Horizontal Flow Fields Observed in Hinode G-band Images. III. The Decay of a Satellite Sunspot and the Role of Magnetic Flux Removal in Flaring. *Astron. Astrophys.* **545**, A192.
- Verma, M., Denker, C.: 2014, Horizontal Flow Fields Observed in Hinode G-band Images. IV. Statistical Properties of the Dynamical Environment around Pores. *Astron. Astrophys.* **563**, A112. doi:[10.1051/0004-6361/201322476](https://doi.org/10.1051/0004-6361/201322476).
- Verma, M., Steffen, M., Denker, C.: 2013, Evaluating Local Correlation Tracking Using CO5BOLD Simulations of Solar Granulation. *Astron. Astrophys.* **555**, A136. doi:[10.1051/0004-6361/201321628](https://doi.org/10.1051/0004-6361/201321628).
- Verma, M., Denker, C., Balthasar, H., Kuckein, C., González Manrique, S.J., Sobotka, M., Bello González, N., Hoch, S., Diercke, A., Kummerow, P., Berkefeld, T., Collados, M., Feller, A., Hofmann, A., Kneer, F., Lagg, A., Löhner-Böttcher, J., Nicklas, H., Pastor Yabar, A., Schlichenmaier, R., Schmidt, D., Schmidt, W., Schubert, M., Sigwarth, M., Solanki, S.K., Soltau, D., Staude, J., Strassmeier, K.G., Volkmer, R., von der Lühe, O., Waldmann, T.: 2016, Horizontal Flow Fields in and around a Small Active Region – The Transition Period between Flux Emergence and Decay. *Astron. Astrophys.* **596**, A3. doi:[10.1051/0004-6361/201628380](https://doi.org/10.1051/0004-6361/201628380).
- Vögler, A.: 2005, On the Effect of Photospheric Magnetic Fields on Solar Surface Brightness. Results of Radiative MHD Simulations. *Mem. Soc. Astron. Ital.* **76**, 842.

- Vögler, A., Schüssler, M.: 2003, Studying Magneto-Convection by Numerical Simulation. *Astron. Nachr.* **324**, 399. doi:[10.1002/asna.200310146](https://doi.org/10.1002/asna.200310146).
- Vögler, A., Schüssler, M.: 2007, A Solar Surface Dynamo. *Astron. Astrophys.* **465**, L43. doi:[10.1051/0004-6361:20077253](https://doi.org/10.1051/0004-6361:20077253).
- Vögler, A., Shelyag, S., Schüssler, M., Cattaneo, F., Emonet, T., Linde, T.: 2005, Simulations of Magneto-Convection in the Solar Photosphere. Equations, Methods, and Results of the MURaM Code. *Astron. Astrophys.* **429**, 335. doi:[10.1051/0004-6361:20041507](https://doi.org/10.1051/0004-6361:20041507).
- Volkmer, R., von der Lühe, O., Kneer, F., Staude, J., Hofmann, A., Schmidt, W., Sobotka, M., Soltau, D., Wiehr, E., Wittmann, A., Berkefeld, T.: 2003a, GREGOR: The New 1.5m Solar Telescope on Tenerife. In: Keil, S.L., Avakyan, S.V. (eds.) *Innovative Telescopes and Instrumentation for Solar Astrophysics, Proc. SPIE* **4853**, 360.
- Volkmer, R., von der Lühe, O., Soltau, D., Emde, P., Krodel, M., Pailer, N., Wiehr, E.: 2003b, Optical and Thermal Design of the Main Optic of the Solar Telescope GREGOR. In: Goodman, W.A. (ed.) *Optical Materials and Structures Technologies, Proc. SPIE* **5179**, 270. doi:[10.1117/12.506710](https://doi.org/10.1117/12.506710).
- Volkmer, R., von der Lühe, O., Kneer, F., Staude, J., Berkefeld, T., Caligari, P., Halbgewachs, C., Heidecke, F., Schmidt, W., Soltau, D., Nicklas, H., Wittmann, A., Balthasar, H., Hofmann, A., Strassmeier, K., Sobotka, M., Klvaňa, M., Collados, M.: 2006, The New 1.5-Meter Solar Telescope GREGOR: First-Light and Start of Commissioning. In: Stepp, L.M. (ed.) *Ground-Based and Airborne Telescopes, Proc. SPIE* **6267**, 62670W.
- Volkmer, R., von der Lühe, O., Denker, C., Solanki, S., Balthasar, H., Berkefeld, T., Caligari, P., Collados, M., Fischer, A., Halbgewachs, C., Heidecke, F., Hofmann, A., Klvaňa, M., Kneer, F., Lagg, A., Popow, E., Schmidt, D., Schmidt, W., Sobotka, M., Soltau, D., Strassmeier, K.G.: 2010a, GREGOR Solar Telescope. *Astron. Nachr.* **331**, 624.
- Volkmer, R., von der Lühe, O., Denker, C., Solanki, S., Balthasar, H., Berkefeld, T., Caligari, P., Collados Vera, M., Halbgewachs, C., Heidecke, F., Hofmann, A., Klvaňa, M., Kneer, F., Lagg, A., Schmidt, W., Sobotka, M., Soltau, D., Strassmeier, K.G.: 2010b, GREGOR Telescope: Start of Commissioning. In: Stepp, L.M., Gilmozzi, R., Hall, H.J. (eds.) *Ground-Based and Airborne Telescopes III, Proc. SPIE* **7733**, 77330K.
- Volkmer, R., Eisenträger, P., Emde, P., Fischer, A., von der Lühe, O., Nicklas, H., Soltau, D., Schmidt, W., Weis, U.: 2012, Mechanical Design of the Solar Telescope GREGOR. *Astron. Nachr.* **333**, 816. doi:[10.1002/asna.201211740](https://doi.org/10.1002/asna.201211740).
- von der Lühe, O.: 1998, High-Resolution Observations with the German Vacuum Tower Telescope on Tenerife **42**, 493. doi:[10.1016/S1387-6473\(98\)00060-8](https://doi.org/10.1016/S1387-6473(98)00060-8).
- von der Lühe, O., Schmidt, W., Soltau, D., Berkefeld, T., Kneer, F., Staude, J.: 2001, GREGOR: A 1.5-Meter Telescope for Solar Research. *Astron. Nachr.* **322**, 353.
- von der Lühe, O., Soltau, D., Berkefeld, T., Schelenz, T.: 2003, KAOS: Adaptive Optics System for the Vacuum Tower Telescope at Teide Observatory. In: Keil, S.L., Avakyan, S.V. (eds.) *Innovative Telescopes and Instrumentation for Solar Astrophysics, Proc. SPIE* **4853**, 187.
- von der Lühe, O., Volkmer, R., Kentischer, T.J., Geißler, R.: 2012, The GREGOR Broad-Band Imager. *Astron. Nachr.* **333**, 894. doi:[10.1002/asna.201211735](https://doi.org/10.1002/asna.201211735).
- Wang, H., Zirin, H.: 1992, Flows around Sunspots and Pores. *Solar Phys.* **140**, 41.
- Wang, J., Li, W., Denker, C., Lee, C., Wang, H., Goode, P.R., McAllister, A., Martin, S.F.: 2000, Minifilament Eruption on the Quiet Sun. I. Observations at H α Central Line. *Astrophys. J.* **530**, 1071.

- Wedemeyer-Böhm, S., Lagg, A., Nordlund, Å.: 2009, Coupling from the Photosphere to the Chromosphere and the Corona. *Space Science Rev.* **144**, 317. doi:[10.1007/s11214-008-9447-8](https://doi.org/10.1007/s11214-008-9447-8).
- Wöger, F., von der Lühe, O.: 2008, KISIP: A Software Package for Speckle Interferometry of Adaptive Optics Corrected Solar Data. In: *Advanced Software and Control for Astronomy II, Proc. SPIE* **7019**, 70191E. doi:[10.1117/12.788062](https://doi.org/10.1117/12.788062).
- Wöger, F., von der Lühe, O., Reardon, K.: 2008, Speckle Interferometry with Adaptive Optics Corrected Solar Data. *Astron. Astrophys.* **488**, 375. doi:[10.1051/0004-6361:200809894](https://doi.org/10.1051/0004-6361:200809894).
- Xu, Z., Lagg, A., Solanki, S.K.: 2010, Magnetic Structures of an Emerging Flux Region in the Solar Photosphere and Chromosphere. *Astron. Astrophys.* **520**, A77. doi:[10.1051/0004-6361/200913227](https://doi.org/10.1051/0004-6361/200913227).
- Xu, Z., Lagg, A., Solanki, S., Liu, Y.: 2012, Magnetic Fields of an Active Region Filament from Full Stokes Analysis of Si textsci 1082.7 nm and He I 1083.0 nm. *Astrophys. J.* **749**, 138. doi:[10.1088/0004-637X/749/2/138](https://doi.org/10.1088/0004-637X/749/2/138).
- Zeeman, P.: 1897, The Effect of Magnetisation on the Nature of Light Emitted by a Substance. *Nature* **55**, 347. doi:[10.1038/055347a0](https://doi.org/10.1038/055347a0).
- Zuccarello, F., Guglielmino, S.L., Battiato, V., Contarino, L., Spadaro, D., Romano, P.: 2009, Emergence and Evolution of Active and Ephemeral Regions: Comparison between Observations and Models. *Acta Geophys.* **57**, 15. doi:[10.2478/s11600-008-0057-3](https://doi.org/10.2478/s11600-008-0057-3).
- Zwaan, C.: 1978, On the Appearance of Magnetic Flux in the Solar Photosphere. *Solar Phys.* **60**, 213.
- Zwaan, C.: 1985, The Emergence of Magnetic Flux. *Solar Phys.* **100**, 397. doi:[10.1007/BF00158438](https://doi.org/10.1007/BF00158438).
- Zwaan, C.: 1987, Elements and Patterns in the Solar Magnetic Field. *Ann. Rev. Astron. Astrophys.* **25**, 83. doi:[10.1146/annurev.aa.25.090187.000503](https://doi.org/10.1146/annurev.aa.25.090187.000503).

Acknowledgments

I owe my sincere gratitude to my supervisor Prof. Dr. Carsten Denker. He gave me the opportunity to realize one of my biggest dreams. Thanks to him, this thesis has the best scientific and English level that I could ever imagine. Without all his support, suggestions, and advice, I would never have finished it. I would like to mention that I not only appreciate his advice in science but also in real life. I hope to honor him by continuing my scientific career and always striving to do my best as he taught me. Furthermore, I would like to thank the co-supervisor of this thesis Prof. Dr. Gottfried Mann. Many thanks to my mentor Prof. Dr. Lutz Wisotzki. I would like to sincerely thank Dr. Manuel Collados who gave me many ideas enhancing this thesis project and for his hospitably during my research visit in Tenerife.

Special thanks to my student mentor Dr. Yori Fournier. He listened to me many times when I was very stressed and sometimes sad. He gave me advice and cheered me up in the most difficult moments but he was also there congratulating me to my achievements. I am very grateful to all members of the Solar Optical Physics group at AIP, with their help everything was easier and enjoyable. Particularly, I would like to thank Dr. Christoph Kuckein, he was also a co-supervisor, a colleague, a friend, a brother. He has been my most important support in every way during this trip. I will never forget everything he has done for me. There are no words that can describe everything I feel – for that many thanks. I also want to thank Dr. Meetu Verma for helping me with many things during the thesis, but most importantly for helping me to understand and how to communicate with Carsten when I was lost. I am indebted to Dr. Horst Balthasar for his support during this journey but even more for taking me to work to Slovakia, he knows why. It is a pleasure for me to thank Andrea who helped me with many things, including proof-reading the bibliography. She is a very good colleague and an even a better friend.

My heartfelt appreciation to all the scientists involved in the manuscripts and the observations: especially to Dr. Peter Gömöry for his help and advice, Dr. Sami Solanki, Dr. Andreas Lagg, Dr. Wolfgang Schmidt, Adur Pastor Yabar, Dr. Rolf Schlichenmaier, and Dr. Nazaret Bello González for all their comments and suggestions.

I would like to thank to my former supervisor Dr. Jose Carlos del Toro Iniesta. He prepared me in the best way for the future that awaited me. I am also indebted to many teachers and professors at the Universidad de Granada and Universidad de La Laguna, but specially to Dr. Basilio Ruiz Cobo who made me love solar physics and encouraged me to pursue my dreams and supported me all these years.

I would like to thank all my colleagues at AIP Benito, Alessandro, Gohar, Olga, and Friedrich. I am sure that I am forgetting to many of them but thanks to all of them. Also to my friends Aythami, Jorge, and Fran. They were supporting me all together from ‘Nucleo Duro’. A special word of gratitude I would like to dedicate to Carlos, thank you for everything my brother. To Ana González, thank you for all the long talks.

I would like to acknowledge all the support, love, patient, and trust of my beloved fiancée Bibiána, without all her support I could never succeed in this adventure. I would like to thank also to Laura for accepting me and making everything easier during all these years – grazie mille.

Finally, I would like to thank my family. Gracias de todo corazón a mis padres, por todo su incondicional apoyo, por su paciencia, por creer en mí incluso cuando yo no lo hacía. Por todo su amor, ayuda, consejos, ánimos. No tengo palabras para expresar toda mi gratitud hacia ellos. Les quiero mucho. A mi hermana, Anita. Gracias por aguantarme todo este tiempo, por apoyarme, animarme, ser mi confidente, a ti también te quiero mucho. Muchísimas gracias al resto de mi familia por apoyarme desde el familiote y los primos Manrique. Gracias por todos los ánimos, Ina, Rosa, Heri, Loly, Eves, Cesar, Pedrito, Domingo, Esther, Vane, Vero, María, Eli, Juan Antonio, Andrés, Manu, Octavio, Edu, Jocsan, Carla, Mamá Lola y el resto de mi familia querida. Por último, me gustaría dar las gracias y dedicar esta tesis a mi abuelo que ya no está. Espero que lo estés viendo allá donde estés papá Pedro, esto también es una parte tuya.

The 1.5-meter GREGOR solar telescope was built by a German consortium under the leadership of the Kiepenheuer-Institut für Sonnenphysik in Freiburg with the Leibniz-Institut für Astrophysik Potsdam, the Institut für Astrophysik Göttingen, and the Max-Planck-Institut für Sonnensystemforschung in Göttingen as partners, and with contributions by the Instituto de Astrofísica de Canarias and the Astronomical Institute of the Academy of Sciences of the Czech Republic. The Vacuum Tower Telescope (VTT) at the Spanish Observatorio del Teide of the Instituto de Astrofísica de Canarias is operated by the Kiepenheuer-Institut für Sonnenphysik in Freiburg. The Solar Dynamics Observatory is developed and launched by NASA. The SDO data are provided by the Joint Science Operations Center – Science Data Processing at Stanford University. The Solar and Heliospheric Observatory (SoHO) is a project of international cooperation between the European Space Agency (ESA) and the National Aeronautics and Space Administration (NASA). This research has made use of NASA’s Astrophysics Data System. SolarSoftWare is a public-domain software package for analysis of solar data written in the Interactive Data Language by Harris Geospatial Solutions. Only thanks to the easy access of data and software libraries, a fast analysis was possible in the time period allotted to a doctoral thesis. This work was carried out as a part of the SOLARNET project supported by the European Commission’s 7th Framework Programme under grant agreement No. 312495. I am grateful for financial support from the Leibniz Graduate School for Quantitative Spectroscopy in Astrophysics, a joint project of the Leibniz Institute for Astrophysics Potsdam (AIP) and the Institute of Physics and Astronomy of the University of Potsdam (UP).

Appendix A – Abstracts

Refereed articles

Horizontal flow fields in and around a small active region – The transition period between flux emergence and decay

M. Verma, C. Denker, H. Balthasar, C. Kuckein, S.J. González Manrique, M. Sobotka, N. Bello González, S. Hoch, A. Diercke, P. Kummerow, T. Berkefeld, M. Collados, A. Feller, A. Hofmann, F. Kneer, A. Lagg, J. Löhner-Böttcher, H. Nicklas, A. Pastor Yabar, R. Schlichenmaier, D. Schmidt, W. Schmidt, M. Schubert, M. Sigwarth, S.K. Solanki, D. Soltau, J. Staude, K.G. Strassmeier, R. Volkmer, O. von der Lühe, and T. Waldmann: 2016, *Astron. Astrophys.* 596, A3. doi: [10.1051/0004-6361/201628380](https://doi.org/10.1051/0004-6361/201628380)

Context. The solar magnetic field is responsible for all aspects of solar activity. Thus, emergence of magnetic flux at the surface is the first manifestation of the ensuing solar activity.

Aims. Combining high-resolution and synoptic observations has the ambition to provide a comprehensive description of flux emergence at photospheric level and of the growth process eventually leading to a mature active region.

Methods. Small active region NOAA 12118 emerged on 2014 July 17 and was observed one day later with the 1.5-meter GREGOR solar telescope on 2014 July 18. High-resolution time-series of blue continuum and G-band images acquired in the Blue Imaging Channel of the GREGOR Fabry-Pérot Interferometer were complemented by synoptic line-of-sight magnetograms and continuum images obtained with the Helioseismic and Magnetic Imager onboard the Solar Dynamics Observatory. Horizontal proper motions and horizontal plasma velocities were computed with local correlation tracking and the differential affine velocity estimator, respectively. Morphological image processing was employed to measure the photometric/magnetic area, magnetic flux, and the separation profile of the emerging flux region during its evolution.

Results. The computed growth rates for photometric area, magnetic area, and magnetic flux are about two times larger than the respective decay rates. The space-time diagram using HMI magnetograms of five days provides a comprehensive view of growth and decay. It traces a leaf-like structure, which is determined by the initial separation of the two polarities, a rapid expansion phase, a time when the spread stalls, and a period when the region slowly shrinks again. The separation rate of 0.26 km s^{-1} is highest in the initial stage, and it decreases when the separation comes to a halt. Horizontal plasma velocities computed at four evolutionary stages indicate a changing pattern of inflows. In LCT maps we find persistent flow patterns such as outward motions in the outer part of the two major pores, a diverging feature near the trailing pore marking the site of upwelling plasma and flux emergence, and low velocities in the interior of dark pores. We detected many elongated, rapidly expanding granules between the two major polarities, with two times larger dimensions than the normal granules.

Inference of magnetic fields in the very quiet Sun

M.J. Martínez González, A. Pastor Yabar, A. Lagg, A. Asensio Ramos, M. Collados, S.K. Solanki, H. Balthasar, T. Berkefeld, C. Denker, H. P. Doerr, A. Feller, M. Franz, S.J. González Manrique, A. Hofmann, F. Kneer, C. Kuckein, R.E. Louis, O. von der Lühe, H. Nicklas, D. Orozco, R. Rezaei, R. Schlichenmaier, D. Schmidt, W. Schmidt, M. Sigwarth, M. Sobotka, D. Soltau, J. Staude, K.G. Strassmeier, M. Verma, T. Waldmann, and R. Volkmer: 2016, *Astron. Astrophys.* 596, A5. doi: [10.1051/0004-6361/201628449](https://doi.org/10.1051/0004-6361/201628449)

Context. Over the last 20 years the quietest areas of the solar surface have revealed a weak but extremely dynamic magnetism occurring at small scales ($< 500 \text{ km}$), which may provide an important contribution to the dynamics and energetics of the outer layers of the atmosphere.

Understanding this magnetism requires the inference of physical quantities from high spatio-temporal resolution, high sensitivity spectro-polarimetric data.

Aims. We present high spatial resolution ($0.4''$), high precision spectro-polarimetric data of the very quiet Sun at $1.56 \mu\text{m}$ to shed some light on this complex magnetism.

Methods. We use inversion techniques using two main approaches. First, we assume that the observed profiles can be reproduced with a constant magnetic field atmosphere embedded in a field-free medium. Second, we assume substructure within the resolution element either with two constant magnetic atmospheres or a single magnetic atmosphere with gradients of the physical quantities along the optical depth, both coexisting with a global stray light component.

Results. Half of our observed quiet Sun region is better explained by magnetic substructure within the resolution element. However, we can not discriminate if this substructure comes from gradients of the physical parameters along the LOS or from horizontal gradients (across the surface). In these pixels, a two magnetic component model is preferred and we find two distinct populations of magnetic fields. The one with larger filling factor has very weak (~ 150 G) horizontal fields similar to those obtained in previous works. We demonstrate that the field vector of this population is not constrained by the observations, given the spatial resolution and polarimetric accuracy of our data. The topology of the other component with smaller filling factor is constrained by the observations for field strengths above 250 G: we infer hG fields with inclinations and azimuth values compatible with an isotropic distribution. The filling factors are typically below 30%. We also find that the flux of the two polarities is not balanced. From the other half of the observed quiet Sun area $\sim 50\%$ are two-lobbed Stokes V profiles, meaning that 23% of the FOV can be adequately explained with a single constant magnetic field embedded in a non-magnetic atmosphere. From the regular profiles, only in 50% the magnetic field vector and filling factor are reliably inferred. Therefore, 12% of the FOV harbour hG fields with filling factors typically below 30%. Still at our present spatial resolution, 70% of the pixel is apparently non-magnetized.

Spectropolarimetric Observations of an Arch Filament System with the GREGOR solar telescope

H. Balthasar, P. Gömöry, S.J. González Manrique, C. Kuckein, J. Kavka, A. Kučera, P. Schwartz, R. Vasková, T. Berkefeld, M. Collados Vera, C. Denker, A. Feller, A. Hofmann, A. Lagg, H. Nicklas, R. Schlichenmaier, D. Schmidt, W. Schmidt, M. Sigwarth, M. Sobotka, S.K. Solanki, D. Soltau, J. Staude, K.G. Strassmeier, R. Volkmer, O. von der Lühe, and T. Waldmann: 2016, *Astron. Nachr.* 337, 1050. doi: [10.1002/asna.201612432](https://doi.org/10.1002/asna.201612432)

Arch filament systems occur in active sunspot groups, where a fibril structure connects areas of opposite magnetic polarity, in contrast to active region filaments that follow the polarity inversion line. We used the GREGOR Infrared Spectrograph (GRIS) to obtain the full Stokes vector in the spectral lines Si I 1082.7 nm, He I 1083.0 nm, and Ca I 1083.9 nm. We focus on the near-infrared calcium line to investigate the photospheric magnetic field and velocities, and use the line core intensities and velocities of the helium line. The individual fibrils of the arch filament system connect the sunspot with patches of magnetic polarity opposite to that of the spot. These patches do not necessarily coincide with pores, where the magnetic field is strongest. Instead areas are preferred not far from the polarity inversion line. These areas exhibit photospheric downflows of moderate velocity, but significantly higher downflows of up to 30 km s^{-1} in the chromospheric helium line. Our findings can be explained with new emerging flux where the matter flows downward along the field lines of rising flux tubes.

Solar Physics at the Einstein Tower

C. Denker, C. Heibel, J. Rendtel, K. Arlt, H. Balthasar, A. Diercke, S.J. González Manrique, A. Hofmann, C. Kuckein, H. Önel, V. Senthamizh Pavaai, J. Staude, and M. Verma: 2016, *Astron. Nachr.* 337, 1105. doi: [10.1002/asna.201612442](https://doi.org/10.1002/asna.201612442)

The solar observatory Einstein Tower (*Einsteinturm*) at the Telegrafenberg in Potsdam is both a landmark of modern architecture and an important place for solar physics. Originally built for high-resolution spectroscopy and measuring the gravitational redshift, research shifted over the years to understanding the active Sun and its magnetic field. Nowadays, telescope and spectrographs are used for research and development, i.e., testing instruments and in particular polarization optics for advanced instrumentation deployed at major European and international astronomical and solar telescopes. In addition, the Einstein Tower is used for educating and training of the next generation astrophysicists as well as for education and public outreach activities directed at the general public. This article comments on the observatory's unique architecture and the challenges of maintaining and conserving the building. It describes in detail the characteristics of telescope, spectrographs, and imagers; it portrays some of the research and development activities.

Flow and magnetic field properties in the trailing sunspots of active region NOAA 12396

M. Verma, C. Denker, F. Böhm, H. Balthasar, E. Fischer, C. Kuckein, N. Bello González, T. Berkefeld, M. Collados, A. Diercke, A. Feller, S.J. González Manrique, A. Hofmann, A. Lagg, H. Nicklas, D. Orozco Suárez, A. Pastor Yabar, R. Rezaei, R. Schlichenmaier, D. Schmidt, W. Schmidt, M. Sigwarth, M. Sobotka, S.K. Solanki, D. Soltau, J. Staude, K.G. Strassmeier, R. Volkmer, O. von der Lühe, T. Waldmann: 2016, *Astron. Nachr.* 337, 1090.

doi: [10.1002/asna.201612447](https://doi.org/10.1002/asna.201612447)

Improved measurements of the photospheric and chromospheric three-dimensional magnetic and flow fields are crucial for a precise determination of the origin and evolution of active regions. We present an illustrative sample of multi-instrument data acquired during a two-week coordinated observing campaign in August 2015 involving, among others, the GREGOR solar telescope (imaging and near-infrared spectroscopy) and the space missions Solar Dynamics Observatory (SDO) and Interface Region Imaging Spectrograph (IRIS). The observations focused on the trailing part of active region NOAA 12396 with complex polarity inversion lines and strong intrusions of opposite polarity flux. The GREGOR Infrared Spectrograph (GRIS) provided Stokes IQUV spectral profiles in the photospheric Si I $\lambda 1082.7$ nm line, the chromospheric He I $\lambda 1083.0$ nm triplet, and the photospheric Ca I $\lambda 1083.9$ nm line. Carefully calibrated GRIS scans of the active region provided maps of Doppler velocity and magnetic field at different atmospheric heights. We compare quick-look maps with those obtained with the ‘Stokes Inversions based on Response functions’ (SIR) code, which furnishes deeper insight into the magnetic properties of the region. We find supporting evidence that newly emerging flux and intruding opposite polarity flux are hampering the formation of penumbrae, i.e., a penumbra fully surrounding a sunspot is only expected after cessation of flux emergence in proximity to the sunspots.

Conference proceedings

Flows along arch filaments observed in the GRIS ‘very fast spectroscopic mode’

S.J. González Manrique, C. Denker, C. Kuckein, A. Pastor Yabar, M. Collados, M. Verma, H. Balthasar, A. Diercke, C.E. Fischer, P. Gömöry, N. Bello González, R. Schlichenmaier, M. Cubas Armas, T. Berkefeld, A. Feller, S. Hoch, A. Hofmann, A. Lagg, H. Nicklas, D. Orozco Suárez, D. Schmidt, W. Schmidt, M. Sigwarth, M. Sobotka, S.K. Solanki, D. Soltau, J. Staude, K.G. Strassmeier, R. Volkmer, O. von der Lühe, T. Waldmann: 2017, in *IAU Symp.*, Vol. 327, *Fine Structure and Dynamics of the Solar Atmosphere*, ed. S. Vargas Domínguez, A. G. Kosovichev, L. Harra, P. Antolin, submitted.

A new generation of solar instruments provides improved spectral, spatial, and temporal resolution, thus facilitating a better understanding of dynamic processes on the Sun. High-resolution observations often reveal multiple-component spectral line profiles, e.g., in the near-infrared He I

10830 Å triplet, which provides information about the chromospheric velocity and magnetic fine structure. We observed an emerging flux region, including two small pores and an arch filament system, on 2015 April 17 with the ‘very fast spectroscopic mode’ of the GREGOR Infrared Spectrograph (GRIS) situated at the 1.5-meter GREGOR solar telescope at Observatorio del Teide, Tenerife, Spain. We discuss this method of obtaining fast (one per minute) spectral scans of the solar surface and its potential to follow dynamic processes on the Sun. We demonstrate the performance of the ‘very fast spectroscopic mode’ by tracking chromospheric high-velocity features in the arch filament system.

sTools – a data reduction pipeline for the GREGOR Fabry-Pérot Interferometer and the High-resolution Fast Imager at the GREGOR solar telescope

C. Kuckein, C. Denker, M. Verma, H. Balthasar, S.J. González Manrique, R.E. Louis, A. Diercke: 2017, in IAU Symp., Vol. 327, Fine Structure and Dynamics of the Solar Atmosphere, ed. S. Vargas Domínguez, A. G. Kosovichev, L. Harra, P. Antolin, submitted.

A huge amount of data has been acquired with the GREGOR Fabry-Pérot Interferometer (GFPI), large-format facility cameras, and since 2016 with the High-resolution Fast Imager (HiFI). These data are processed in standardized procedures with the aim of providing science-ready data for the solar physics community. For this purpose, we have developed a user-friendly data reduction pipeline called “sTools” based on the Interactive Data Language (IDL) and licensed under creative commons license. The pipeline delivers reduced and image-reconstructed data with a minimum of user interaction. Furthermore, quick-look data are generated as well as a webpage with an overview of the observations and their statistics. All the processed data are stored online at the GREGOR GFPI and HiFI data archive of the Leibniz Institute for Astrophysics Potsdam (AIP). The principles of the pipeline are presented together with selected high-resolution spectral scans and images processed with sTools.

Flows in and around active region NOAA12118 observed with the GREGOR solar telescope and SDO/HMI

M. Verma, C. Denker, H. Balthasar, C. Kuckein, S.J. González Manrique, M. Sobotka, N. Bello González, S. Hoch, A. Diercke, P. Kummerow, T. Berkefeld, M. Collados, A. Feller, A. Hofmann, F. Kneer, A. Lagg, J. Löhner-Böttcher, H. Nicklas, A. Pastor Yabar, R. Schlichenmaier, D. Schmidt, W. Schmidt, M. Schubert, M. Sigwarth, S.K. Solanki, D. Soltau, J. Staude, K.G. Strassmeier, R. Volkmer, O. von der Lühe, and T. Waldmann: 2016, Ground-Based Solar Observations in the Space Instrumentation Era, ASP Conference Series, [2016arXiv160301109V](https://arxiv.org/abs/2016arXiv160301109V)

Accurate measurements of magnetic and velocity fields in and around solar active regions are key to unlocking the mysteries of the formation and the decay of sunspots. High spatial resolution image and spectral sequences with a high cadence obtained with the GREGOR solar telescope give us an opportunity to scrutinize 3-D flow fields with local correlation tracking and imaging spectroscopy. We present GREGOR early science data acquired in 2014 July-August with the GREGOR Fabry-Pérot Interferometer and the Blue Imaging Channel. Time-series of blue continuum (λ 450.6 nm) images of the small active region NOAA 12118 were restored with the speckle masking technique to derive horizontal proper motions and to track the evolution of morphological changes. In addition, high-resolution observations are discussed in the context of synoptic data from the Solar Dynamics Observatory.

Spectropolarimetric observations of an arch filament system with GREGOR

H. Balthasar, P. Gömöry, S.J. González Manrique, C. Kuckein, A. Kučera, P. Schwartz, T. Berkefeld, M. Collados, C. Denker, A. Feller, A. Hofmann, D. Schmidt, W. Schmidt, M. Sobotka,

S.K. Solanki, D. Soltau, J. Staude, K.G. Strassmeier, O. von der Lühe: 2017, in Solar Polarization 8, ASP Conference Series, ed. Belluzi, L., Casini, R., Trujillo Bueno, J. and Romoli, M., submitted.

We observed an arch filament system (AFS) in a sunspot group with the GREGOR Infrared Spectrograph attached to the GREGOR solar telescope. The AFS was located between the leading sunspot of negative polarity and several pores of positive polarity forming the following part of the sunspot group. We recorded five spectro-polarimetric scans of this region. The spectral range included the spectral lines Si I 1082.7 nm, He I 1083.0 nm, and Ca I 1083.9 nm. In this work we concentrate on the silicon line which is formed in the upper photosphere. The line profiles are inverted with the code ‘Stokes Inversion based on Response functions’ to obtain the magnetic field vector. The line-of-sight velocities are determined independently with a Fourier phase method. Maximum velocities are found close to the ends of AFS fibrils. These maximum values amount to 2.4 km s^{-1} next to the pores and to 4 km s^{-1} at the sunspot side. Between the following pores, we encounter an area of negative polarity that is decreasing during the five scans. We interpret this by new emerging positive flux in this area canceling out the negative flux. In summary, our findings confirm the scenario that rising magnetic flux tubes cause the AFS.

Photospheric magnetic fields of the trailing sunspots in active region NOAA 12396

M. Verma, H. Balthasar, C. Denker, F. Böhm, C.E. Fischer, C. Kuckein, S.J. González Manrique, M. Sobotka, N. Bello González, A. Diercke, T. Berkefeld, M. Collados, A. Feller, A. Hofmann, A. Lagg, H. Nicklas, D. Orozco Suárez, A. Pastor Yabar, R. Rezaei, R. Schlichenmaier, D. Schmidt, W. Schmidt, M. Sigwarth, S.K. Solanki, D. Soltau, J. Staude, K.G. Strassmeier, R. Volkmer, O. von der Lühe, T. Waldmann: 2017, in Solar Polarization 8, Astronomical Society of the Pacific Conference Series, ed. Belluzi, L., Casini, R., Trujillo Bueno, J. and Romoli, M., submitted.

Active region NOAA 12396 emerged on 2015 August 3 and was observed three days later with the 1.5-meter GREGOR solar telescope on 2015 August 6. High-resolution spectropolarimetric data from the GREGOR Infrared Spectrograph were obtained in the photospheric Si I $\lambda 1082.7$ nm and Ca I $\lambda 1083.9$ nm lines, together with the chromospheric He I $\lambda 1083.0$ nm triplet. We present two-component inversions of the photospheric Ca I line using the ‘Stokes Inversions based on Response functions’ code. Besides improving the fits of multi-lobed Stokes V profiles, sorting the two magnetic components according to their filling factor revealed the presence of kilo-Gauss fields in regions with ongoing flux emergence, which prevented the formation of penumbrae.

Appendix B – List of Acronyms

3D	Three-Dimensional
AFS	Arch Filament System
AIP	Leibniz-Institut für Astrophysik Potsdam
AO	Adaptive Optics
BBI	Broad-Band Imager
BBSO	Big Bear Solar Observatory
BIC	Blue Imaging Channel
BFI	Broad-Band Filter Imager
CCD	Charge-Coupled Device
CM	Cloud Model
CRISP	CRisp Imaging SpectroPolarimeter
DST	Dunn Solar Telescope
EFR	Emerging Flux Region
ESA	European Space Agency
EUV	Extreme Ultra-Violet
FLCR	Ferroelectric Liquid Crystal Retarder
FOV	Field-of-View
FPI	Fabry-Pérot Interferometer
FTS	Fourier Transform Spectrometer
FWHM	Full-Width-at-Half-Maximum
GAOS	GREGOR Adaptive Optics System
GFPI	GREGOR Fabry-Pérot Interferometer
GCT	Gregory-Coudé Telescope
GPU	GREGOR Polarimetric Unit
GRIS	GREGOR Infrared Spectrograph
HAZEL	HAAnle and ZEEeman Light code
HELIX⁺	He-Line Information Extractor
HELLRIDE	HELioseismological Large Regions Interferometric DEvice
HMI	Helioseismic and Magnetic Imager
HSRA	Harvard-Smithsonian Reference Atmosphere
IAC	Instituto de Astrofísica de Canarias
IBIS	Interferometric Bidimensional Spectrometer
IDL	Interactive Data Language
IMaX	Imaging Magnetograph eXperiment
IRIS	Interface Region Imaging Spectrograph
KAOS	Kiepenheuer Adaptive Optics System
KIS	Kiepenheuer-Institute für Sonnenphysik
LEST	Large Earth-based Solar Telescope
LCT	Local Correlation Tracking
LOS	Line-of-Sight
LTE	Local Thermodynamic Equilibrium

MDI	Michelson Doppler Imager
MELANIE	Milne-Eddington Line Analysis using Numerical Inversion Engine
MFBD	Multi-Frame Blind Deconvolution
MFGS	Median Filter Gradient Similarity
MHD	Magnetohydrodynamics
MOMFBD	Multi-Object MultiFrame Blind Deconvolution
MPS	Max-Planck-Institut für Sonnensystemforschung
MURaM	MPS/University of Chicago RAdiative MHD
NASA	National Aeronautics and Space Administration
NIR	Near Infrared
NIST	National Institute of Standards and Technology
NLTE	Non-Local Thermodynamic Equilibrium
NOAA	National Oceanic and Atmospheric Administration
OT	Observatorio del Teide
PIL	Polariry Inversion Line
POLIS	Polarimetric Littrow Spectrograph
ROI	Region-of-Interest
RTE	Radiative Transfer Equation
SDO	Solar Dynamics Observatory
SIR	Stokes Inversion based on Response function
SoHO	Solar and Heliospheric Observatory
SST	Swedish Solar Telescope
TIP	Tenerife Infrared Polarimeter
TESOS	Telecentric Etalon Solar Spectrometer
UP	University of Potsdam
VIM	Visible-light and NIR Imaging Magnetograph
VSO	Virtual Solar Observatory
VTT	Vacuum Tower Telescope